McKinnon, Bryan (2006) *Search for the [Theta] + Pentaquark in the Reaction [gamma]d->pK +K -n with CLAS*. PhD thesis.

http://theses.gla.ac.uk/3586/

Search for the Θ^+ Pentaquark in the Reaction $\gamma d \rightarrow pK^+K^-n$ with CLAS

Bryan McKinnon

Presented as a Thesis for the Degree of Doctor of Philosophy

Nuclear Physics Group
Department of Physics and Astronomy
University of Glasgow

Abstract

Recently reported theoretical predictions and experimental observations have revitalised the interest in the pentaquark (an exotic baryon with quark configuration $qqqq\bar{q}$). Confirmation of the existence of such a state would be an important addition to our understanding of Quantum ChromoDynamics (QCD). The non-definitive nature and low statistics of all reported observations motivated the CLAS Collaboration at the Thomas Jefferson National Accelerator Facility (JLab) to perform the first ever experiment dedicated to the Θ^+ pentaquark (with configuration $uudd\bar{s}$). This high statistics measurement of Θ^+ photoproduction on deuterium was completed using the CLAS detector at JLab. The experiment E03-113, entitled G10, took data between March 13th - May 17th 2004, with tagged photons, produced from an electron beam of energy $3.767\,GeV$, incident on a $24\,cm$ liquid-deuterium target. The final state $\gamma d \rightarrow pK^+K^-n$ was analysed for evidence of the previously reported Θ^+ member of the predicted pentaquark anti-decuplet. This analysis studied the exclusive reaction mechanism, with the proton and both kaons detected in CLAS. No evidence of any narrow Θ^+ pentaquark state in the invariant mass of the nK^+ system around $1.54\,GeV/c^2$ was observed. Furthermore, details of a modified 4-body phase space Monte Carlo simulation are shown which lead to a determination of CLAS detector acceptance as a function of invariant mass. Consequently, the cross-section of the process $\gamma d \rightarrow pK^+K^-n$ is calculated along with the determination of an upper limit on the cross-section $\gamma d \rightarrow p\Theta^+K^-$. This upper limit in the mass range $1.52\,GeV/c^2 - 1.56\,GeV/c^2$ is less than $0.3\,nb$ (95% confidence level), and less than $0.6\,nb$ in the mass range $1.48\,GeV/c^2 - 1.7\,GeV/c^2$.

This current result [1] shows that the Θ^+ (invariant mass nK^+) peak of the previous CLAS report [2] could not be reproduced, and places significant limits on the production cross-section.

Declaration

The data presented in this thesis were obtained as part of the G10 Experiment of the CLAS Collaboration at the U.S. Department of Energy's Jefferson Lab in Virginia and the University of Glasgow's Nuclear Physics Group. I participated fully in the preparation and execution of the experiment. The analysis of the experimental data is my own work. This thesis was composed by myself.

Bryan McKinnon

May 2006

Contents

List of Figures

List of Tables

Chapter 1

Introduction

For more than 30 years, physicists have searched for the pentaquark, a baryon composed of four quarks (q) plus an anti-quark ($\bar{q}$). Definitive evidence for the existence of such a state would be an important addition to our understanding of Quantum ChromoDynamics (QCD), which itself does not prohibit its existence [3,4]. Furthermore, the determination of which colour singlet configurations exist in nature is a fundamental aim of non-perturbative QCD. A narrow baryon resonance with the exotic strangeness quantum number $S = +1$ is a natural candidate for such a pentaquark state, with the quark configuration ($uudd\bar{s}$).

It is well established from high energy neutrino antineutrino scattering experiments [5, 6], that sea-quarks ($q\bar{q}$ pairs) are part of the ground state wave function of the nucleon. In addition, pion electroproduction experiments in the $\Delta - resonance$ region have shown the presence of a pion *cloud* surrounding the valence quarks [7]. Consequently, we know that five quark configurations ($qqqq\bar{q}$) exist as an admixture with the three valence quarks. However, the question of whether a five quark configuration where the anti-quark ($\bar{q}$) has a different flavour than (and hence cannot annihilate with) the other valence quarks is the motivation for the search for pentaquark states.

The lack of experimental evidence for strongly interacting particles with more than three valence quarks was a principle of the original quark model introduced by Gell-Mann and Ne'eman [8]. However, given the non-prohibitive nature of QCD to their existence, the non-definitive experimental observation of five valence quark configurations ($qqqq\bar{q}$) remains an unresolved mystery of the strong interaction. Indeed, the physical bias against any quark configuration other than mesons ($q\bar{q}$) and baryons (qqq) has led to a debate as to whether the rules governing QCD should be modified to prohibit pentaquark states [9].

Exotic multi-quark structures beyond the basic quark model were suggested

by Jaffe [10] and others in the 1970's. These resonances were thought to be too wide to be detected by experiment. However, recently the prediction of a narrow pentaquark by Diakonov *et al* [11] has renewed interest in searches for an exotic baryon with valence quark configuration ($qqqq\bar{q}$), known as the Θ^+. If this Θ^+ exists, then theorists face the task of describing such states by using effective degrees of freedom [12] or lattice gauge calculations [13] of the QCD Lagrangian.

1.1 Previous Measurements

1.1.1 Θ^+ Measurements

The first evidence of a possible $S = +1$ exotic baryon was reported by the LEPS collaboration [14] in the reaction $\gamma n \to K^+ K^- n$, with the neutron bound in a ^{12}C target. The narrow state was seen in the missing mass spectrum (see figure 1.1) of the K^-, after the removal of events associated with the production of the $\phi(1020)$ and $\Lambda(1520)$. The reported mass was $1.54 \pm 0.01\,GeV/c^2$, with a width less than $0.025\,GeV/c^2$ and a statistical significance of $(4.6 \pm 0.1)\,\sigma$. The photon energy range for this measurement was $1.5 - 2.35\,GeV$.
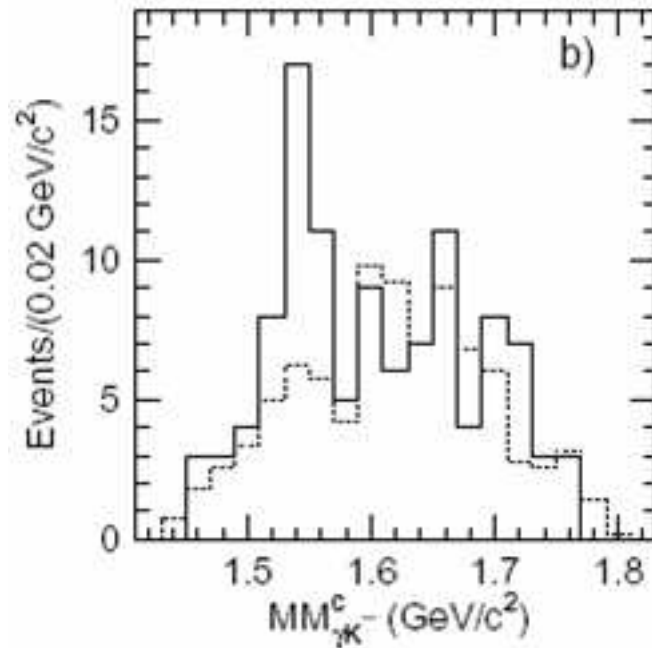
Figure 1.1: The missing mass $MM(K^-)$ spectrum (solid line) in the reaction $\gamma n \to K^+ K^- n$ on a ^{12}C target, from the LEPS collaboration. The dotted line indicates events from a LH_2 target.

This result from LEPS renewed the interest in pentaquark searches within the hadronic physics community, and since its release several other experiments have reported supportive evidence for exotic pentaquarks. In May 2003, the CLAS collaboration reported the observation of a $S = +1$ Θ^+ baryon state in photoproduction on the deuteron (detailed in section 1.1.3). Subsequently, CLAS also reported [15] the observation of a possible Θ^+ decaying to nK^+ in photoproduction on the proton $\gamma p \to \pi^+ K^+ K^- n$. Figure 1.2 shows the invariant mass $M(nK^+)$, with a peak at a mass of $1.555 \pm 0.010\,GeV/c^2$ and a width of less than $0.026\,GeV/c^2$. The statistical significance was calculated to be $(7.8 \pm 1.0)\,\sigma$. The photon energy range for this experiment was $3.00 - 5.47\,GeV$.
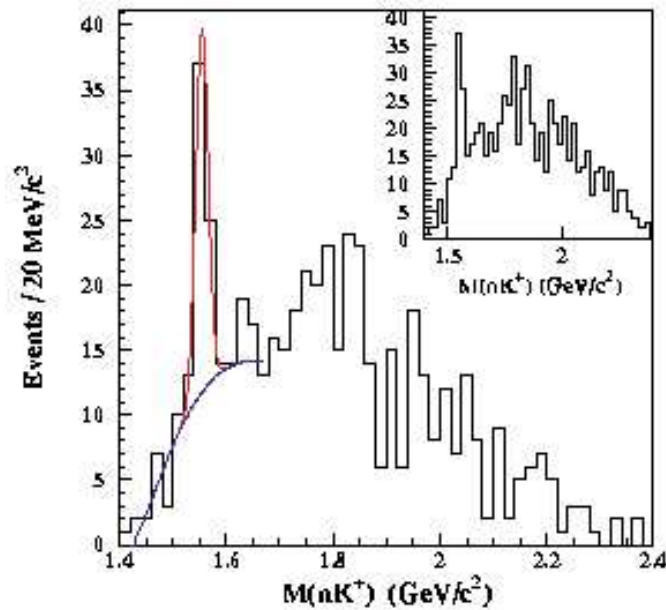
Figure 1.2: The invariant mass $M(nK^+)$ in the reaction $\gamma p \to \pi^+ K^+ K^- n$. The insert histogram is the invariant mass with less restrictive analysis cuts.

Further to this CLAS measurement in photoproduction on the proton, the SAPHIR collaboration reported a possible Θ^+ signal in the reaction $\gamma p \to K^+ K_s^0 n$ [16]. Up until this point, these reported results shared the commonality of a Θ^+ decaying to nK^+ ($\Theta^+ \to nK^+$). However, isospin symmetry predicts that the Θ^+ should have an equal branching ratio into both nK^+ and pK^0. The DIANA collaboration at ITEP, re-analysed existing $K - Xenon$ bubble chamber data, and reported the first evidence of a possible Θ^+ decaying to pK^0 [17]. Figure 1.3 shows the invariant mass $M(pK^0)$ spectrum, with a narrow peak at $1.54\,GeV/c^2$ and a width less than $0.01\,GeV/c^2$. The reported statistical significance was $4\,\sigma$ (no error quoted). In addition to the DIANA result, several other experiments

reported [18–21] possible evidence in this decay mode, with masses ranging from 1.525 to 1.555 GeV/c^2.
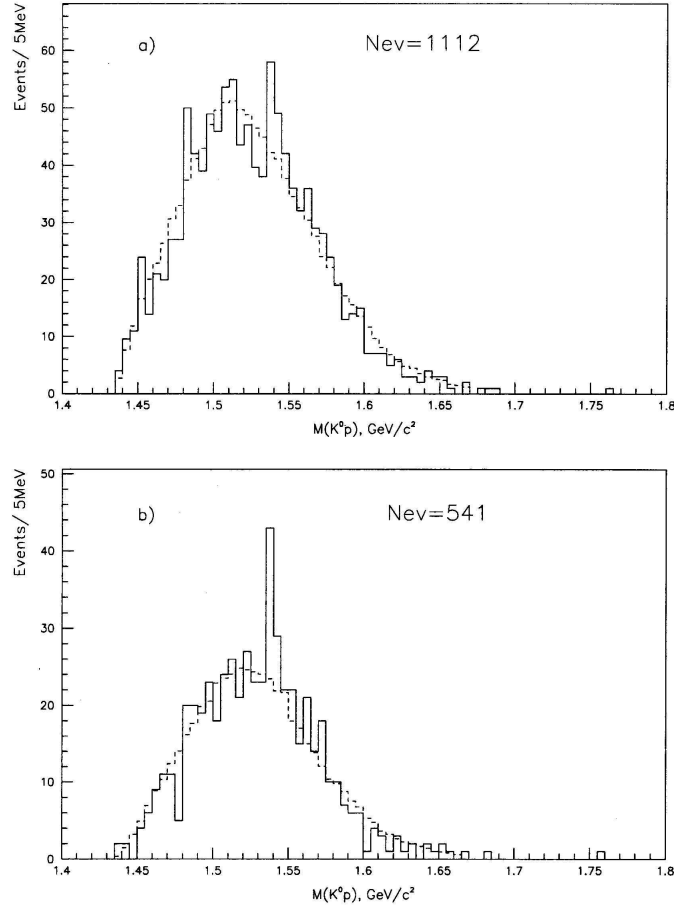
Figure 1.3: The invariant mass $M(pK^0)$ spectrum in the reaction $K^+ Xe \to \Theta^+ Xe' \to pK^0 Xe'$. a) for all events, b) events after suppressing proton and K^0 re-interactions.

Further to these recently reported observations, a review of a 1973 paper [22] has posed the question as to whether a narrow resonance in the invariant mass $M(pK^0)$ spectrum was overlooked (see figure 1.4). These results are from the analysis of $K^+ p \to pK^0 X$ bubble chamber data. At this time, around thirty years ago, it was predicted that a $S = +1$ pentaquark would have a width of the order $0.1 \, GeV/c^2$, and therefore such a narrow signal could have been missed.
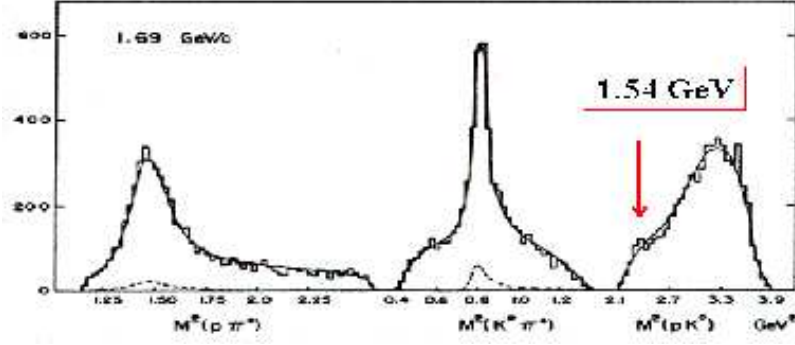
Figure 1.4: Results from and old (1973) CERN analysis showing a shoulder corresponding to a mass of $1.54\,GeV/c^2$ in the invariant mass $M(pK^0)$.

The large number of experiments reporting possible evidence for the Θ^+ pentaquark is indeed compelling. However, no single experiment adequately meets the criteria for irrefutable evidence of the existence of this exotic $S = +1$ state ($uudd\bar{s}$). Furthermore, there are a number of experiments in which it should have been possible to observe the Θ^+, yet null results were reported. A summary of published results with evidence for the existence of the Θ^+ can be found in table 1.1. A more detailed summary can be found in Ref. [23], in addition to reports of non-observations.

Group	Ref.	Reaction	Mass [GeV/c^2]	Width [GeV/c^2]	σ's
LEPS	[14]	$\gamma n \to K^+ K^- n$	1.540 ± 0.010	< 0.025	4.6
DIANA	[17]	$K^+ Xe \to K^0 p Xe'$	1.539 ± 0.002	< 0.009	4.4
CLAS	[2]	$\gamma d \to p K^+ K^- n$	1.542 ± 0.005	< 0.021	5.2 ± 0.6
SAPHIR	[16]	$\gamma d \to K^+ K^0 n$	1.540 ± 0.006	< 0.025	4.8
ITEP	[18]	$\nu A \to p K^0 X$	1.533 ± 0.005	< 0.020	6.7
CLAS	[15]	$\gamma p \to \pi^+ K^+ K^- n$	1.555 ± 0.010	< 0.026	7.8
HERMES	[19]	$e^+ d \to K^0 p X$	1.526 ± 0.003	0.013 ± 0.009	~ 5
ZUES	[24]	$e^+ p \to e^+ K^0 p X$	1.522 ± 0.003	0.008 ± 0.004	~ 5
COSY-TOF	[21]	$pp \to K^0 p \Sigma^+$	1.530 ± 0.005	< 0.018	$4 - 6$
SVD	[20]	$pA \to K^0 p X$	1.526 ± 0.005	< 0.024	5.6

Table 1.1: Experiments with reported evidence for the Θ^+.

1.1.2   Other Pentaquark Measurements

The predicted (using the chiral soliton model) baryon anti-decuplet of Diakonov *et al* has three exotic states, Θ, Ξ^{--} and Ξ^+, of which the Θ^+ is the least massive. The other two predicted exotic Ξ states have strangeness $S = -2$.

The first evidence of a possible Ξ^{--} state was reported by the NA49 collaboration [25]. A doubly negative charged baryon state, with $S = -2$, was seen at a mass of $1.860\,GeV/c^2$ decaying to $\Xi^-\pi^-$. The combined invariant mass spectra, $M(\Xi^-\pi^-,\ \Xi^-\pi^+,\ \bar{\Xi}^+\pi^-,\ \bar{\Xi}^+\pi^+)$, can be seen in figure 1.5, with the $\Xi^{--} \to \Xi^-\pi^-$ and a possible isospin partner $\Xi^0 \to \Xi^-\pi^+$ observed at the same mass. However, to date this evidence of another pentaquark state has as yet not been corroborated, and the performed analysis has been questioned [26].
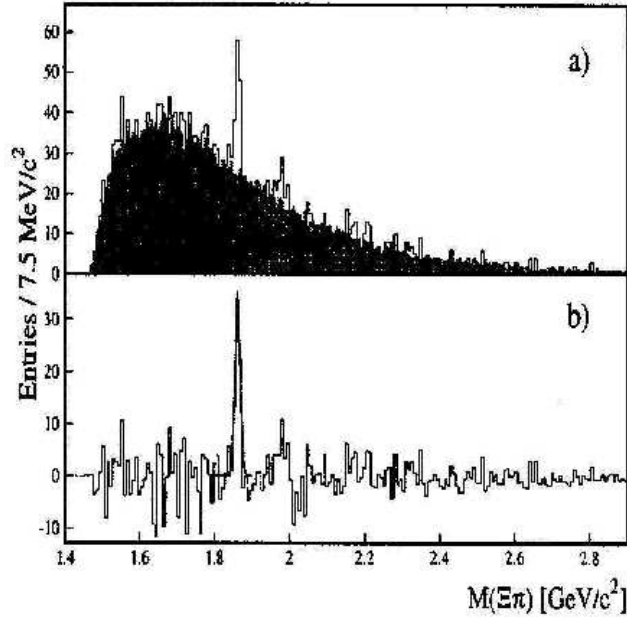
Figure 1.5: a) The sum of the $M(\Xi^-\pi^-,\ \Xi^-\pi^+,\ \bar{\Xi}^+\pi^-,\ \bar{\Xi}^+\pi^+)$ invariant mass spectra (the shaded histogram represents a mixed event background). b) Background subtracted spectrum with a fit to the peak.

1.1.3 CLAS Θ^+ Measurement in the reaction $\gamma d \to pK^+K^-n$

The previous published [2] measurement of the exclusive reaction $\gamma d \to pK^+K^-n$ by the CLAS collaboration shows evidence for the Θ^+ decaying to nK^+ at an invariant mass $M(nK^+)$ of $1.542 \pm 0.005\,GeV/c^2$ with a width of $0.021\,GeV/c^2$. The statistical significance of the peak is $(5.2 \pm 0.6)\ \sigma$ (although further analysis of this data suggests that the significance of the observed peak may not be as large as indicated [27]). Figure 1.6 shows this previous result.
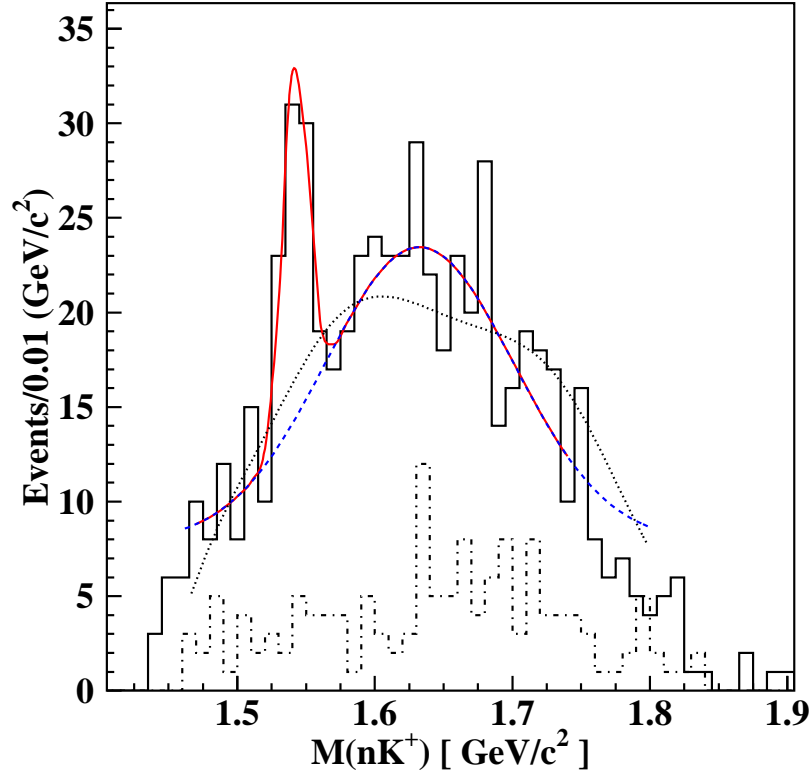
Figure 1.6: Invariant mass $M(nK^+)$ in the reaction $\gamma d \to pK^+K^-n$, which has strangeness $S = +1$, showing a sharp peak at a mass of $1.542\,GeV/c^2$. The fit to the peak (solid line) on top of the smooth background (dashed line), gives a statistical significance of $5.8\,\sigma$. The dotted line is a simulated background and the dash-dot histogram are events associated with the production of $\Lambda(1520)$.

The assumed Θ^+ production mechanism for this reaction is shown in figure 1.7. In this reaction $\gamma d \to pK^+K^-n$, the Θ^+ decays to the nK^+ final state, and it is likely that Θ^+ production proceeds via *t-channel* K^+ exchange on the neutron. This being the case, the proton will act as a spectator and will not therefore have sufficient momentum to be detected in the CLAS spectrometer. However, the final state interaction (FSI) involving the proton and the K^- (see figure 1.7) will rescatter the proton into the CLAS acceptance.
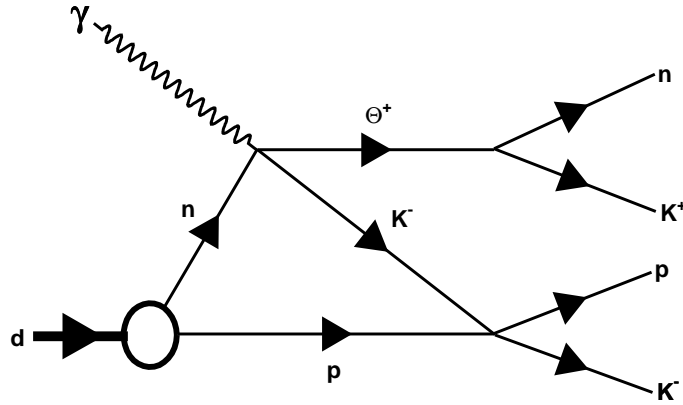
Figure 1.7: A rescattering diagram that could contribute to the production of the Θ^+ and an energetic proton via FSI with the K^-.

Given the implications, both experimentally and towards a deeper understanding of Quantum ChromoDynamics (QCD), of this previous measurement, reproducibility became a necessity. Consequently, this motivated the G10 experiment at CLAS and the analysis presented in this thesis. The G10 experiment was the first ever dedicated search for the Θ^+, and aimed to significantly increase the statistics of the previous measurement.

1.2   CLAS G10

The CLAS experiment E03-113, Θ^+ Pentaquark Searches in Photoproduction from Deuterium [28], ran from March 13th until May 17th 2004. The main aim of this experiment was to gather high statistics data for the production of the Θ^+ in the reaction $\gamma d \to pK^+K^-n$; $\Theta^+ \to nK^+$.

Other physics issues that were to be investigated with this data set included:

1. determination of the Θ^+ mass with $\pm 2\,MeV/c^2$ accuracy (if observed).

2. search for the Θ^+ in the reactions:
   $\gamma d \to \Lambda^0 nK^+$; $\Theta^+ \to nK^+$
   $\gamma d \to p\pi^+\pi^- K^-$; $\Theta^+ \to pK^0$, $K^0 \to \pi^+\pi^-$
   $\gamma n \to K^- nK^+$; $\Theta^+ \to nK^+$ (with Fermi momentum correction)

3. search for other non-exotic members of the predicted anti-decuplet of pentaquark baryons.

4. determination of the Θ^+ spin using analysis of the angular distribution of the decay kaon (if observed).

A total of 61 accelerator days were available assuming 50% average efficiency, to result in the proposed 30 days of beam time. In reality, the average efficiency was 62% ABU (actual beam used) which therefore allowed additional calibration measurements on a hydrogen target and a tagger energy calibration to be conducted without adversely affecting the production statistics.

The analysis presented in this thesis was carried out on the same reaction channel as the previous CLAS measurement: $\gamma d \rightarrow pK^+K^-n$, with the Θ^+ decaying to the nK^+ ($\Theta^+ \rightarrow nK^+$). Details of the experimental apparatus, data calibration and processing, and the analysis steps follow in the proceeding chapters. The final chapter provides a summary of the results and conclusions.

Chapter 2

Theoretical Background

2.1 Quantum ChromoDynamics *(QCD)*

The quark model proposed by Gell-Mann [29] and Zweig [30,31], was introduced to explain the spectrum of strongly interacting particles in terms of constituents called *quarks*. In this model, mesons (Baryon number $B = 0$) are bound states of a quark / anti-quark pair ($q\bar{q}$), and baryons ($B = 1$) are bound states of three quarks (qqq). Together mesons and baryons form the group known as hadrons (particles which interact through the strong force). The quantum numbers of all known hadrons can be obtained simply from their quark content (see table 2.1).

Flavour	Mass [GeV/c^2]	Spin	B	Q	I_3	S	C	$\widetilde{B}$	T
u	$0.0015 - 0.004$	$\frac{1}{2}$	$\frac{1}{3}$	$\frac{2}{3}$	$\frac{1}{2}$	0	0	0	0
d	$0.004 - 0.008$	$\frac{1}{2}$	$\frac{1}{3}$	$-\frac{1}{3}$	$-\frac{1}{2}$	0	0	0	0
s	$0.08 - 0.13$	$\frac{1}{2}$	$\frac{1}{3}$	$-\frac{1}{3}$	0	-1	0	0	0
c	$1.15 - 1.35$	$\frac{1}{2}$	$\frac{1}{3}$	$\frac{2}{3}$	0	0	1	0	0
b	$4.1 - 4.4$	$\frac{1}{2}$	$\frac{1}{3}$	$-\frac{1}{3}$	0	0	0	-1	0
t	172.7 ± 2.9 [32]	$\frac{1}{2}$	$\frac{1}{3}$	$\frac{2}{3}$	0	0	0	0	1

Table 2.1: Quantum numbers of the 6 flavours of quarks.

The two most stable (and common) baryons, the proton (uud) and the neutron (udd), are isospin partners. Indeed, $SU(2)$ isospin symmetry itself is believed to be a result of the closeness in mass of the u and d quarks. The introduction of strangeness extends $SU(2)$ isospin symmetry into $SU(3)$ flavour symmetry. $SU(3)$ flavour symmetry is not exact, since the mass of the strange quark is significantly larger than that of the up and down quarks. Additionally, quarks retain their identity under the strong or electromagnetic interactions, however weak interactions do not prohibit reactions such as $s \rightarrow u + \bar{u}d$.

Light meson states ($q\bar{q}$) are classified according to the $SU(3) \otimes SU(3)$ group, which translates into a nonet. The nonet ($8 \oplus 1$) is decomposed into an octet and a singlet (see figure 2.1). For the baryon states (qqq), $SU(3)$ flavour decomposition gives rise to 27 possible combinations ($10 \oplus 8 \oplus 8 \oplus 1$). Baryon ground states are obtained by combining the $SU(3)$ flavour decomposition with the $SU(2)$ isospin decomposition. These ground state baryons are shown in figure 2.2.
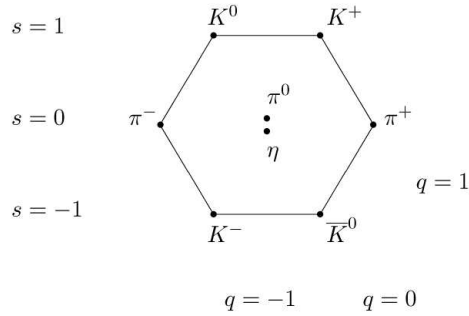
Figure 2.1: Meson nonet: octect plus a singlet. (s is strangeness and q is charge).
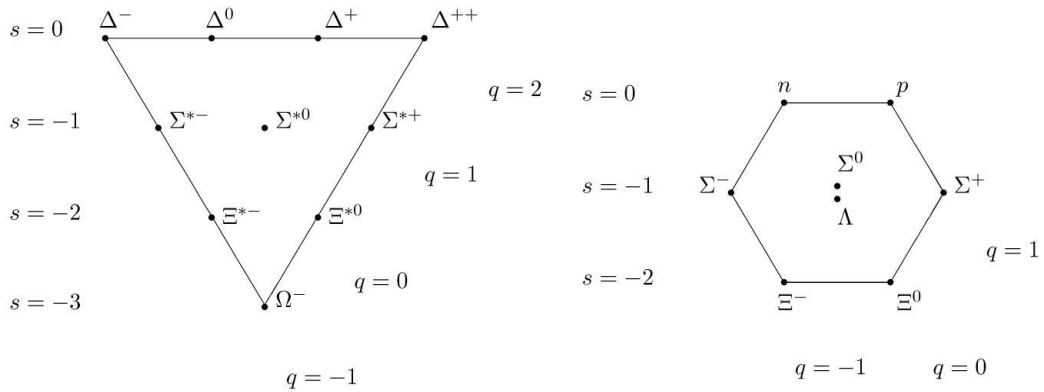
Figure 2.2: Baryons: spin 3/2 decuplet (left) and spin 1/2 octet (right). (s is strangeness and q is charge).

The original quark model was a phenomenological success, however two problems remained unresolved: the lack of free particles with fractional charge, and the apparent violation of Fermi-Dirac statistics in terms of the quantum numbers of the Δ^{++} (which has spin 3/2, charge +2, and is interpreted as a *uuu* bound state with zero orbital angular momentum and all three quark spins parallel, which violates the Pauli exclusion principle).

Therefore, to resolve these problems of the constituent quark model, Han and Nambu, Greenberg and Gell-Mann, proposed that quarks carry an additional

(unobserved) quantum number called *colour*, and introduced an internal $SU(3)$ gauge symmetry. The assumption (indeed colour confinement is a requirement of QCD) that hadrons form colour singlets implies that the only possible light hadrons are the mesons, baryons and anti-baryons. Colour symmetry is identified with a gauge group, and the strong interaction acts upon the quark colour fields of this group. Consequently, this results in a model of the strong interaction as a system of quarks (of six flavours), each assigned to the fundamental representation of the local gauge group $SU(3)$. The quanta of the $SU(3)$ gauge field are called *gluons*, and the theory is known as Quantum ChromoDynamics (QCD), detailed by Wilczek and Gross [33].

Quantum ChromoDynamics is a non-Abelian gauge field theory based upon $SU(3)_c$ (colour) symmetry. The fundamental particles are the quarks, which follow Fermi-Dirac statistics, their colour fields being the fundamental degrees of freedom, mediated through gluon (the gauge boson of the strong interaction) exchange. The underlying symmetries are described in terms of group theory and Lie algebra.

2.2 Exotic Hadrons

Quantum ChromoDynamics does not prohibit the existence of hadrons which lie outside the simple quark model. Predictions of hadron decay rates and cross-sections based on isospin symmetry, within the quark model, are close to experimental measurements, however the quark model does not address quark confinement within hadrons. Confinement arises as a result of the non-Abelian nature of the $SU(3)_c$ gauge group, which leads to the concept of asymptotic freedom, whereby the interaction between quarks (mediated by the gluons) becomes stronger as the distance between them becomes larger. Indeed the gluons are expected to contribute to the properties of hadronic states (mass and spin) by the provision of extra degrees of freedom. There are various models proposed which predict possible meson and baryon states which have a more complex internal configuration and quantum numbers that cannot exist within the simple quark model. These states are called exotic states and are classified as the following:

- Glueballs with configuration (gg)

- Hybrids with configuration $(q\bar{q}g)$

- Four quark states with configuration $(q\bar{q}q\bar{q})$

- Exotic baryon states with configuration $(qqqq\bar{q})$

2.2.1 Exotic Mesons

The simple quark model states that mesons are composed of a quark and an anti-quark pair $(q\bar{q})$. Furthermore, only this pair contributes to the valence properties of the meson. However, the gluons which bind these two quarks can interact with each other to form a bound state, or interact along with the quarks as a fundamental constituent of the meson. Among the defining quantum numbers of a meson are J^{PC}, where, J is the total angular momentum, P is the parity and C is the charge conjugation. For a conventional meson (bound state of a $q\bar{q}$ pair), the following rules apply:

$$P(q\bar{q}) = (-1)^{L+1} \tag{2.1}$$

$$C(q\bar{q}) = (-1)^{L+S} \tag{2.2}$$

$$J = L + S \tag{2.3}$$

where, L is the orbital angular momentum, and S is the spin. Note that for a $q\bar{q}$ pair, S can only be 0 (antisymmetric singlet) or 1 (triplet). Consequently, the allowed J^{PC} combinations are:

$$0^{-+}, 0^{++}, 1^{--}, 1^{+-}, 1^{++}, 2^{--}, 2^{-+}, 2^{++}, 3^{--}, 3^{+-}, 3^{++}..... \tag{2.4}$$

Gluonic contributions (gluons interacting with the quarks) as described by the flux-tube model [34], allow for states with exotic quantum numbers other than those listed in Eqn. 2.4, as follows:

$$0^{--}, 0^{+-}, 1^{-+}, 2^{+-}, 3^{-+}..... \tag{2.5}$$

Mesons with these quantum numbers are called exotic. One should note that the gluonic flux-tube model [34] is the most commonly adopted of several proposed QCD motivated phenomenological models. Each of these models [35–39] explicitly incorporates the gluonic degree of freedom into the meson $q\bar{q}g$ interaction. Research on exotic mesons is the primary motivation behind the future GLUEX and PANDA experiments.

2.2.2   Exotic Baryons

The identification of exotic mesons can be achieved by their exotic J^{PC} quantum numbers, but there is no equivalent for the case of exotic baryons. Baryons have no C-parity, and all half-integer J values with both positive and negative parity can arise from a three quark configuration. However, baryons could exist with exotic quantum numbers such as positive strangeness, which cannot be obtained from a three quark configuration. Such baryons would be unambiguously exotic, and an $S = +1$ baryon state has been proposed in the context of the bag model [4]. Historically, the search for exotic baryons focused on pentaquark states with minimal quark configuration ($qqqq\bar{q}$), where the $\bar{q}$ has a different flavour than the other quarks. These experiments were primarily kaon-nucleon scattering, and involved a phase shift analysis. The mass range for these searches was $1.55 - 2.65 \, GeV/c^2$, and the expected width of such a state was of the order $\sim 100 \, MeV/c^2$. No evidence was ever found for these exotic pentaquark states.

Further to the pentaquark, there are other proposed exotic baryons being sought. One exotic baryon candidate is the di-baryon. The H di-baryon [40] is a particle (possibly stable and long-lived) with the quark configuration *uuddss*.

2.3   Chiral Soliton Model

The chiral soliton model, proposed by Skyrme [41], suggests that the low energy behaviour of nucleons can be interpreted as a spherically symmetric soliton solution of the pion (or chiral) field. The minimal generalisation of spherical symmetry which incorporates three isospin components of the pion field is based on a Hamiltonian of the so-called hedgehog form. In this form, a space rotation of the field is equivalent to a rotation in isospin. The energy eigenvalues of such a rotation are quantized as follows:

$$E_{rot} = \frac{J(J+1)}{2I} \tag{2.6}$$

where, I is the moment of inertia of the soliton. The rotational states are therefore $(2J + 1)^2$-fold degenerate. This results in four nucleon states having $J = 1/2$, and sixteen Δ-isobar states having $J = 3/2$. Consequently, the baryonic nature of the nucleon is interpreted as not due to quarks carrying baryon quantum number $B = 1/3$, but as the baryon number being a topological quantum number of the pion (chiral) field [42, 43].

By introducing a rotation of flavour $SU(3)$ space, the quantizations show that

the lowest rotational state corresponds to an octet with spin 1/2. The next highest rotational state is a decuplet with spin 3/2. These two states are identified with the lowest mass baryon octet and decuplet (the same as the quark model). In the three flavour case, the next highest rotational state is an anti-decuplet with spin 1/2, which does not correspond to any known baryons. This is the prediction of Diakonov *et al* [11], the pentaquark baryon multiplet. As a direct consequence, pentaquark states appear naturally in the framework of the chiral soliton model, as rotational excitations of the rigid soliton core (qqq) surrounded by a meson field ($q\bar{q}$).

Definitive predictions [11] for the masses and widths of the members of this 5-quark baryon anti-decuplet are also given. The structure of the anti-decuplet is shown on figure 2.3.
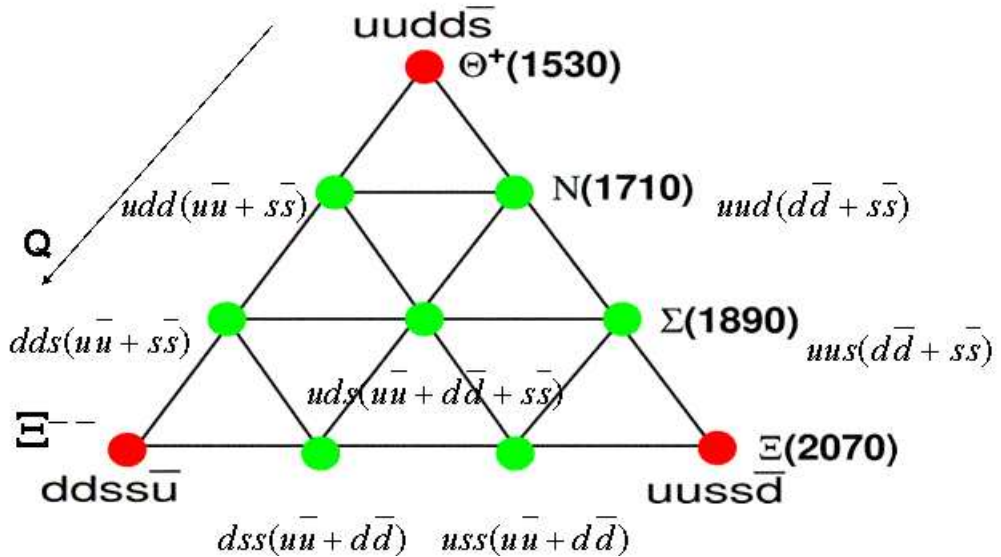
Figure 2.3: The anti-decuplet as predicted by Diakonov *et al.* The three states at the vertices are exotic, whilst the middle octet overlaps with the conventional baryons.

As with other multiplets, the strangeness quantum number S increase by one for each step down. The identification of the nucleon resonance $N(1710)$ as a member of this anti-decuplet, serves as an anchor for predicting the masses of the other members. Symmetries of the chiral soliton model are used to relate the mass splittings of the octet, decuplet and the anti-decuplet, with just three parameters. Two of these parameters are determined using data for the masses of the octet and decuplet, and the third is related to the nucleon Σ-term (corresponding to the effective masses of the light quarks (u d and s) when they are bound inside

the nucleon). This value of the nucleon Σ-term is not precisely determined by experiment, however values of $45 - 65\,MeV$ were taken. The advantage of the chiral soliton model is that the mass splittings are predicted from symmetry, so that if one member of the anti-decuplet is identified, then the masses of the others are predicted. Table 2.2 shows the mass and width predictions of the exotic members of the anti-decuplet.

State	S	Mass $[GeV/c^2]$	Width $[GeV/^2]$	Possible Candidate
Θ^+	$+1$	1.53	0.015	-
N	0	1.71	~ 0.04	$N(1710)P_{11}$
Σ	-1	1.89	~ 0.07	$\Sigma(1880)P_{11}$
Ξ	-2	2.07	> 0.14	$\Xi(2030)?$

Table 2.2: Predictions for masses and widths of the members of the anti-decuplet, with possible candidates.

The most interesting feature of this anti-decuplet is the exotic quantum numbers of the isosinglet member at the top vertex, called the Θ^+. The minimal quark configuration of this state is $uudd\bar{s}$. Using the process described previously, the mass of this state is predicted to be $1.53\,GeV/c^2$, with a width of $0.015\,GeV/c^2$.

2.4   Di-quark Model

Further to the chiral soliton model, the di-quark model [12] has a similar prediction for the masses and widths of the pentaquark baryon states. Jaffe and Wilczek argue that the chiral soliton model, in the three flavour case, primarily relies on chiral $SU(3) \times SU(3)$ symmetry, which is not exact and spontaneously broken in nature. Instead, the framework of the di-quark model interprets the $qqqq\bar{q}$ ($q^4\bar{q}$) system based on the four quarks bound into two spin zero diquarks, combined with the anti-quark. The combination of the four quarks into di-quarks gives rise to:

$$[ud]^2,\ [ud][us],\ [us]^2,\ [us][ds],\ [ds]^2\ and\ [ds][ud] \tag{2.7}$$

When combined with the anti-quark, the result is a degenerate $SU(3)\,8 \oplus 10$ (octet and anti-decuplet). The state $[ud]^2\bar{s}$ is identified with the $\Theta^+(1540)$, whilst the narrowness of the state is proposed to be a result of the relatively weak coupling of the nK^+ continuum to the $[ud]^2\bar{s}$ state. One should note that the two $[ud]$ di-quarks must have wave-functions antisymmetric under spatial exchange

(negative space parity), and when combined with the s quark to form $[ud]^2\bar{s}$, the parity is positive.

2.5 Θ^+ Photoproduction on the Neutron

Since the first evidence of the Θ^+ was reported, many theoretical papers, for example that of Close and Zhao [44], have been devoted to the calculation of the production cross-section, as well as the possible production mechanism. In this section, one such theoretical calculation will be briefly detailed, along with a review of some of the predictions. The model of Guidal *et al* [45] estimates the cross-section for the elementary reaction $\gamma n \rightarrow \Theta^+ K^-$, based on Kaon exchange mechanisms. Furthermore, the sensitivity to spin-parity $J^P = \frac{1}{2}^{\pm}, \frac{3}{2}^{\pm}$ assignments for the Θ^+ is investigated. These estimates use an upper limit on the width of the Θ^+ ($\Gamma_{\Theta^+} = 1\,MeV/c^2$).

At energies above the nucleon resonance, strangeness photoproduction reactions (e.g. $\gamma p \rightarrow K^+\Lambda$) at forward angles are dominated by $K\,and\,K^*$ exchanges. The model presented here extends this to a description of the process:

$$\gamma(q) + n(p_N) \rightarrow \Theta^+(p_\Theta)K^-(p_K) \tag{2.8}$$

where, q is the momentum of the photon, p_N is the momentum of the nucleon (in this case the neutron), p_{Θ^+} is the momentum of the Θ^+, and p_K is the momentum of the kaon (in this case the K^-). The Mandlestam variables for this process are given by the following:

$$s = (p_N + q)^2 \quad t = (q - p_K)^2 \quad u = (q - p_\Theta)^2 \tag{2.9}$$

which satisfies,

$$s + t + u = M_N^2 + M_K^2 + M_\Theta^2 \tag{2.10}$$

where, M_N, $M_K\,and\,M_\Theta$ are the masses of the nucleon (neutron), kaon (K^-) and Θ^+, respectively. The value of M_Θ is taken to be $1.54\,GeV/c^2$, and the reaction is described in the region of large s ($\sqrt{s} > 2\,GeV$) and small t ($-t << s$). The $t-channel$ K^+ exchange process is shown in figure 2.4.
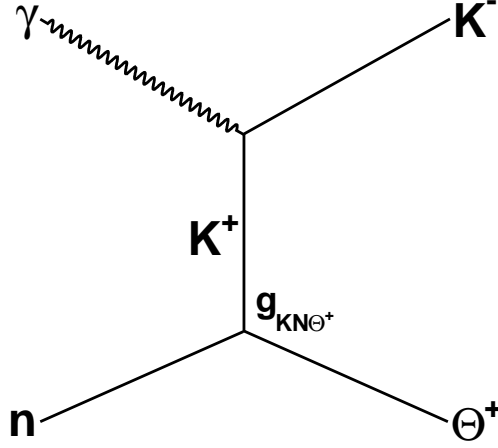
Figure 2.4: *t-channel K^+ exchange.*

As derived in Ref. [45], using a $KN\Theta^+$ vertex function the decay width ($\Gamma_{\Theta \to NK}$) for the spin-parity assignment $J^P = \frac{1}{2}^+$ is given by:

$$\Gamma_{\Theta \to NK} = \frac{g_{KN\Theta}^2}{2\pi} \frac{|p_K|}{M_\Theta} (\sqrt{p_K^2 + M_N^2} - M_N) \tag{2.11}$$

and for the spin-parity assignment $J^P = \frac{1}{2}^-$ is given by:

$$\Gamma_{\Theta \to NK} = \frac{g_{KN\Theta}^2}{2\pi} \frac{|p_K|}{M_\Theta} (\sqrt{p_K^2 + M_N^2} + M_N) \tag{2.12}$$

where, $g_{KN\Theta}$ is the coupling constant and all other terms are as before.

Using $\Gamma_{\Theta \to NK} = 1\,MeV$ for the decay width results in a coupling constant $g_{KN\Theta} \simeq 1.056$ for the $J^P = \frac{1}{2}^+$ case, and $g_{KN\Theta} \simeq 0.1406$ for the $J^P = \frac{1}{2}^-$ case.

The resulting calculated total cross-sections using a width of $1\,MeV$, can be seen in figure 2.5, along with the differential cross-section in figure 2.6, for four spin-parity assignments.
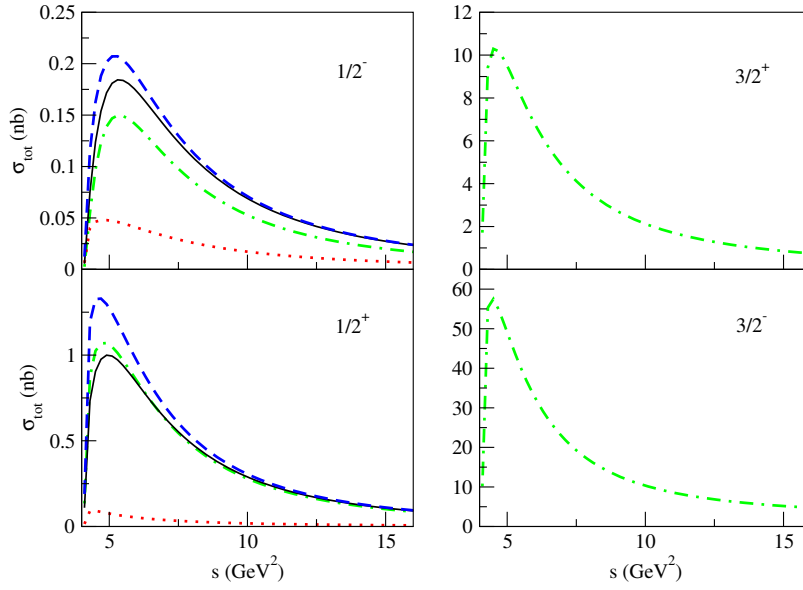
Figure 2.5: Total cross-section predictions [45] for the reaction $\gamma n \rightarrow \Theta^+ K^-$, for different J^P assignments. Green curves: K exchange, Red curves($\pm 1/2$ only): K^* exchange, Blue and black curves: $K + K^*$ exchange.
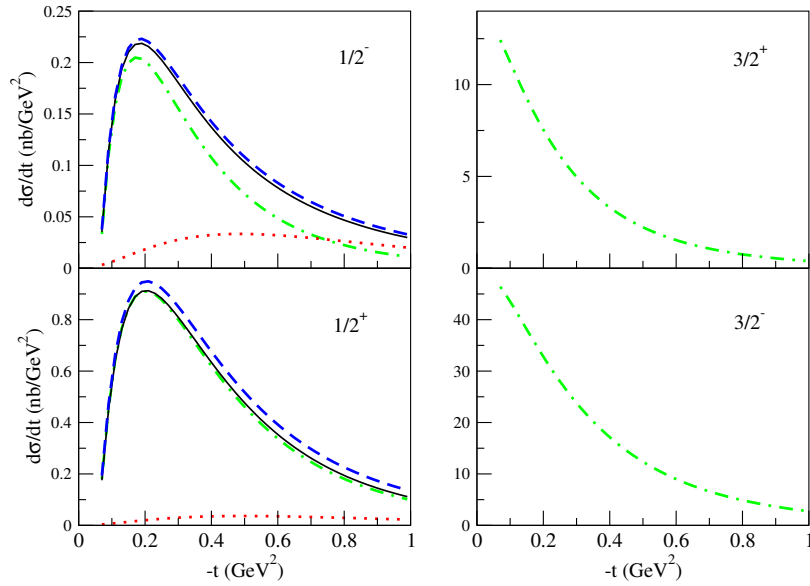
Figure 2.6: Differential cross-section predictions [45] for the reaction $\gamma n \rightarrow \Theta^+ K^-$, for different J^P assignments. Green curves: K exchange, Red curves($\pm 1/2$ only): K^* exchange, Blue and black curves: $K + K^*$ exchange.

As can be seen, the maximum total cross-section is around $1\,nb$ for the $J^P = \frac{1}{2}^+$ case, and around $0.2\,nb$ for the $J^P = \frac{1}{2}^-$. For the the other two cases ($\frac{3}{2}^\pm$), the cross-section is much larger when the same $1\,MeV$ value for the width is used. As previously mentioned, there are many such theoretical cross-section estimates, of which the above is but one. Table 2.3 reviews some other estimates for the total cross-section (in both the $\gamma n \to \Theta^+ K^-$ and $\gamma p \to \Theta^+ \bar{K}^0$ reactions).

Ref.	Reaction	J^P			
		$\frac{1}{2}^-$	$\frac{1}{2}^+$	$\frac{3}{2}^-$	$\frac{3}{2}^+$
[45]	$\gamma p \to \Theta^+ K^0$	0.01	0.22	-	-
	$\gamma n \to \Theta^+ K^-$	0.2	1	55	10
[46]	$\gamma p \to \Theta^+ K^0$	-	(2.7)	8	(1)
	$\gamma n \to \Theta^+ K^-$	-	2.7	200	25
[47]	$\gamma p \to \Theta^+ K^0$	~ 0.4	$\sim 1.6(100)$	-	-
	$\gamma n \to \Theta^+ K^-$	~ 1.7	$\sim 8.7(75)$	-	-
[48]	$\gamma p \to \Theta^+ K^0$	-	15(30)	-	-
	$\gamma n \to \Theta^+ K^-$	-	15(30)	-	-
[49]	$\gamma p \to \Theta^+ K^0$	2	$5.2(\sim 10)$	15.4	1.8
	$\gamma n \to \Theta^+ K^-$	3.5	$11.2(\sim 20)$	48	4

Table 2.3: Theoretical model cross-section predictions (all values are nb). ()-represents models with K^* exchange.

2.6   Exclusive Reaction

The reaction $\gamma d \to p K^+ K^- n$ selects the Θ^+ decaying to the nK^+ final state. The mechanism for this channel could proceed through a two step process. One possible diagram for this process has already been shown in figure 1.7. Here the Θ^+ is created, and the K^- re-interacts with the proton. In this scenario for Θ^+ production, the spectator proton (with a small momentum) requires a final state interaction, FSI (see figure 1.7), with the K^- in order to be detected in CLAS, since the minimum detection momentum in CLAS is $300 - 350\,MeV/c$. Furthermore, the exclusivity of this process allows for the complete reconstruction (by missing mass) of the undetected neutron.

It is likely that Θ^+ production proceeds through *t-channel* K^+ exchange on the neutron. This is an assumed symmetry with $\Lambda(1520)$ production on the proton, which is dominated by *t-channel* K^- exchange [50, 51]. Figure 2.4 shows this *t-channel* K^+ exchange.

The subsequent chapters of this thesis detail the experimental setup and the

analysis of this exclusive reaction $\gamma d \to p K^+ K^- n$. Using the assumptions about the reaction mechanism (FSI) and the $t - channel$ process discussed in this chapter, a production cross-section $\gamma d \to p \Theta^+ K^-$ is measured and a model dependent prediction of the production cross-section of Θ^+ photoproduction on the neutron (the elementary process) will be given.

Chapter 3

Experimental Apparatus

The experiment, designated G10, was carried out in Hall B at Jefferson Lab. The electron beam from the CEBAF accelerator was incident on a radiator producing bremsstrahlung photons which were *tagged* by the Hall B photon tagging spectrometer. This photon beam was subsequently incident on a liquid deuterium (LD_2) target and the outgoing hadrons, from the resulting photoproduction reaction, were detected in CLAS. Figure 3.1 shows a schematic representation of the experimental setup. Overviews of both Jefferson Lab/CEBAF and the Hall B experimental apparatus (CLAS and the photon tagger) are given in the remainder of this chapter.
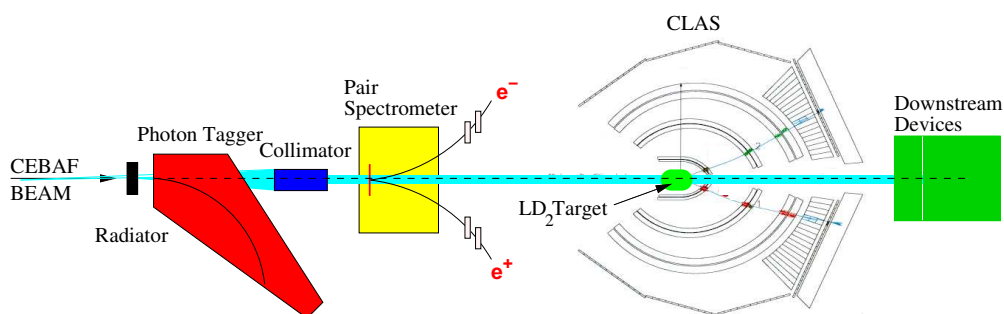
Figure 3.1: Schematic representation of the experimental setup.

3.1 The Thomas Jefferson National Accelerator Facility

The Thomas Jefferson National Accelerator Facility (known as Jefferson Lab or JLab) in Newport News, Virginia, USA is a joint undertaking by the U.S. Depart-

ment of Energy and the Southeastern Universities Research Association (SURA). The purpose of this facility is to study the electromagnetic structure of nucleons and nuclei down to the fundamental quark-gluon picture. Since the first scientific data was taken in 1995, JLab has become the world's premier intermediate energy physics facility, and with the proposed upgrade of the accelerator to $12\,GeV$ and consequent upgrades of each of the three experimental halls, it should continue to remain at the forefront of our understanding of this rich and varied physical domain.

The Continuous Electron Beam Accelerator Facility (CEBAF) at JLab [52] delivers a continuous-wave electron beam of energy upto $\sim 6\,GeV$ to three experimental halls simultaneously. A schematic diagram of CEBAF is shown in figure 3.2. Electrons are injected at energies of a few MeV into the first of two anti-parallel linear accelerators (known as linacs), which are connected by nine recirculation beam arcs in a race-track configuration. The maximum beam energy of $\sim 6\,GeV$ is obtained when the beam is recirculated a maximum of five times. However it can be extracted after any of the complete passes ($\sim 1.2\,GeV$ per pass) and delivered to the experimental Halls A, B and C.
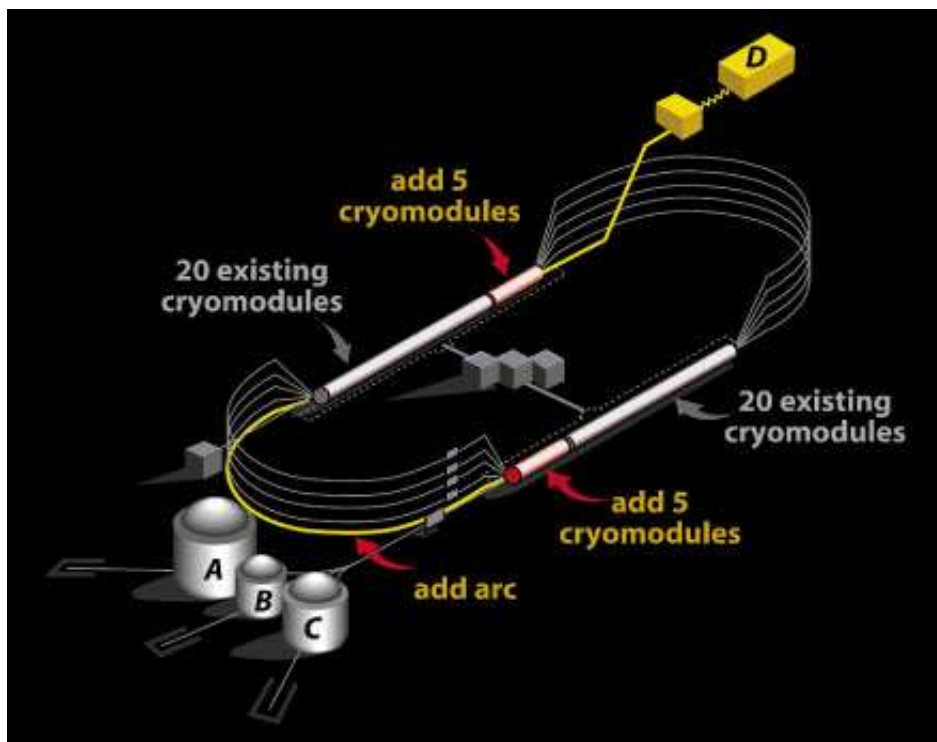
Figure 3.2: Race-track configuration of CEBAF at JLab: 20 cryomodules per linac and nine recirculation arcs. Represented in yellow are the components of the proposed upgrade.

The injected electrons are produced by light from three $499\,MHz$ r.f. gain-switch diode lasers incident on a strained gallium arsenide (GaAs) photocathode wafer which is maintained under high vacuum. The incidence of this circularly polarised laser light upon the GaAs causes the photo-emission of longitudinally polarised electrons. The three interlaced beams are separated by 120° of r.f. phase and are accelerated in a $1497\,MHz$ field. The use of r.f. separators at each of the hall entrances allows the delivery of *beam buckets* with different current and polarisation states to each of the halls simultaneously.

Each of the linacs consists of 20 cryomodules, each containing eight Niobium superconducting radio frequency (s.r.f.) cavities cooled by liquid helium at $2\,K$. As the electrons pass through each cavity they are accelerated by cycling the electromagnetic field within the cavity (in effect creating an area of negative charge behind the electrons and an area of positive charge in front of them). This is achieved by the direction of microwaves cycling at $1497\,MHz$ into each of these cavities. Through this process, each one of the anti-parallel linacs provides an acceleration of $\sim 0.6\,GeV$. The nine recirculation arcs which link the two linacs are formed by the magnetic optics which steer the electrons of different energies through their orbits before extraction and transport to the experimental halls.

CEBAF is capable of delivering beam at currents of up to $120\,\mu A$ in Halls A and C, whilst simultaneously delivering a current as low as $\sim 1\,nA$ to Hall B where the CLAS detector systems and photon tagger limit the operational luminosity. The use of s.r.f. technology means a substantial reduction in the amount of r.f. power needed and thus results in the ability to operate the machine continuously, as opposed to traditional pulsed operation.

3.2   Experimental Hall B

Hall B at Jefferson Lab houses the CEBAF Large Acceptance Spectrometer, known as CLAS, and the photon tagging spectrometer (referred to simply as the photon tagger). This configuration of CLAS detector and photon tagger, allows for both photon and electron beam experiments to be undertaken in Hall B. Furthermore, it is possible to conduct experiments utilising linearly polarised photons by implementing the Hall B Coherent Bremsstrahlung Facility. The G10 experiment operated in the standard photon configuration. Figure 3.3 shows a schematic layout of Hall B with the beam entering from the bottom righthand corner and proceeding through the photon tagger to the target which is situated at the centre of the CLAS detector. Downstream of CLAS are various detec-

tors which are used for photon normalisation and monitoring before the beam terminates in the beam dump.
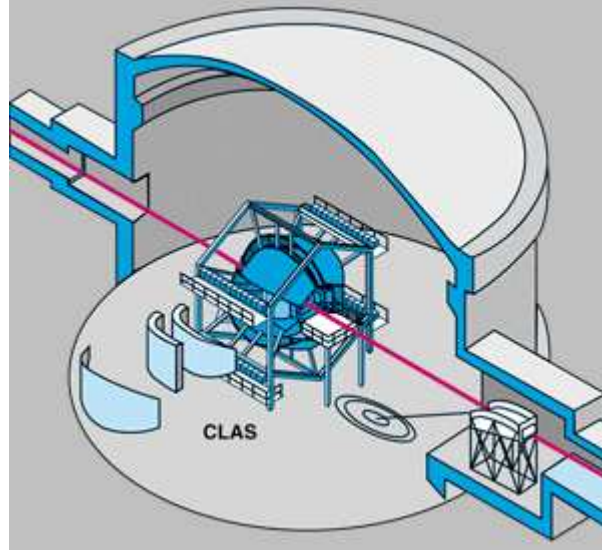
Figure 3.3: Schematic layout of Hall B at Jefferson Lab.

3.3   Photon Tagging Spectrometer

The photon tagger [53] within Hall B is used for the tagging of bremsstrahlung photons. The process of bremsstrahlung radiation occurs when an electron incident upon a radiator emits an energetic photon as it decelerates under the influence of the electromagnetic field nuclei within the radiator: $e \rightarrow e' + \gamma$, where, e and e' are the incident and degraded electron respectively. Tagging is the process of associating the detected, energy degraded electron with the produced photon. Consequently, the energy of the photon can be calculated simply by $E_\gamma = E_0 - E_{e'}$, where, E_0 is the energy of the incident electron (beam energy) and $E_{e'}$ is the energy of the degraded electron measured in the tagger.

The radiator used in the production of bremsstrahlung photons is situated $\sim 0.5\,m$ upstream from the tagger entry window. Upon entering the tagger, an uncharged photon will pass unaltered in path through the magnetic yoke, as shown in figure 3.4. However, the uniform dipole field focuses the energy degraded electrons onto the scintillator hodoscope and full energy electrons to the tagger beam dump. The hodoscope comprises two planes of scintillator detectors known as the energy plane (E-plane) and the timing plane (T-plane).

The E-plane consists of 384 scintillators, each $4\,mm$ in thickness spaced at dis-
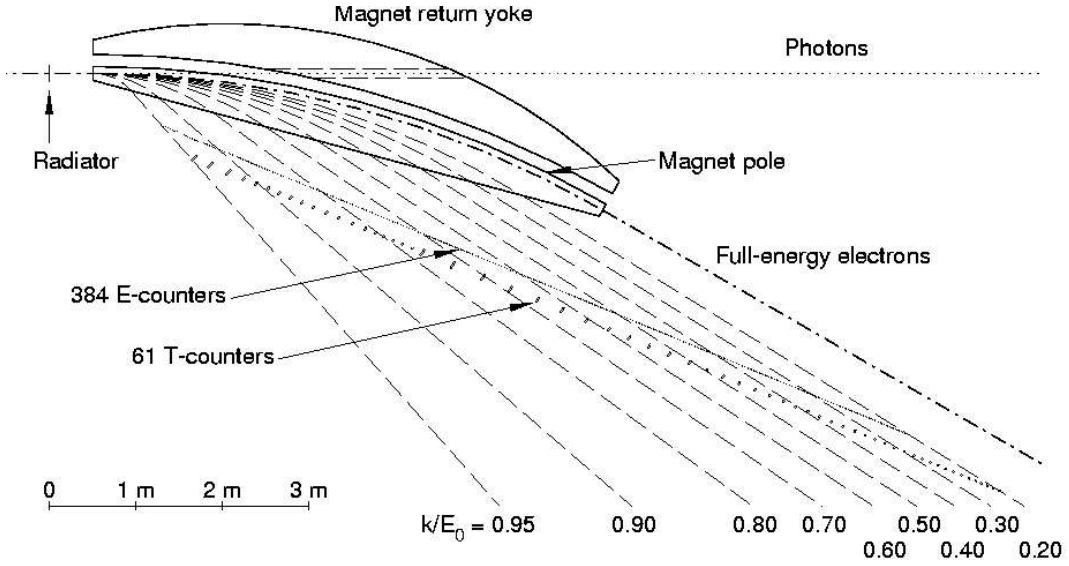
Figure 3.4: Schematic of the photon tagger detailing relative positions. (Note $k_0 \equiv E_{e'}$).

crete intervals along the plane. However, the widths of each of these scintillators varies from $6 - 18\,mm$ dependent upon position, to allow constant momentum bins of $\sim 0.003\,E_0$. The T-plane which lies below the E-plane consists of 61 scintillators each $2\,cm$ in thickness which give a timing resolution of around $50\,ps$, ten times better than the $500\,ps$ timing resolution of the E-counters above. The scintillators in each plane of the hodoscope are geometrically arranged to partially overlap resulting in extra energy and time bins and also serving to reduce background. The overlap on the E-plane provides 767 energy bins/channels, whilst the T-plane provides 121 timing bins/channels. A valid tagger event requires coincidence between a T-counter and its associated E-counters. Signals from either end of the E-counters are read out via a light guide which connects to an optical fibre. These optical fibres are connected to a single PMT. One should note that constant fraction discriminators are used for the photon tagger PMTs, and hence require no time-walk correction. E-counter timing is obtained from a TDC module which can record multiple hits. The T-counter signals are read out from both sides via fixed light guides and PMTs. Again timing is obtained from a TDC module. The outputs of each of the tagger TDCs are grouped together in blocks of four and logically ORed in a module known as the tagger master-OR. This master-OR signal goes on to form part of the CLAS trigger (see section 3.8).

The photon tagger has an energy resolution of $\sim 0.1\%$ of the incident electron beam energy (E_0) and a tagging range of $20 - 95\%\ E_0$.

3.4   G10 Target

The G10 experiment target cell [54], shown in figure 3.5 along with its connecting structure, was a $240\,mm$ in length, $40\,mm$ in diameter cylinder made of Mylar. During the experimental run it was filled with liquid deuterium at $\sim 10\,K$ for production running, and liquid hydrogen for normalisation/calibration runs. In order to increase the forward angle acceptance of negatively charged particles, the G10 target was positioned $25\,cm$ upstream of the CLAS centre ($Z = -25\,cm$).

Figure 3.5: The G10 target cell.

3.5   Hall B Pair Spectrometer

The Hall B pair spectrometer (often referred to as the Primex [55] pair spectrometer), consists of a pair production converter, dipole magnet and two planes of scintillator counters. The pair production converter is an Al foil positioned $55.77\,cm$ upstream of the dipole centre, and is 10^{-3} radiation lengths thick. The scintillators are positioned symmetrically either side of the beamline and the whole ensemble is located $10\,m$ downstream of the photon tagger radiator. During the G10 experiment, the pair spectrometer was additionally instrumented with two pairs of microstrip (MS) detectors, which provided better e^+e^- position determination, each covering a detection area of $400\,mm^2$ and located $930.7\,cm$ downstream of the dipole magnet centre.

The pair spectrometer can be used to provide a measurement of photon beam energy and indeed, if these measurements are taken in coincidence with a tagger E-counter hit, can provide a photon tagger energy calibration (see section 4.5) as was implemented in the G10 experiment. When a photon interacts with the thin converter in front of the pair spectrometer, e^+e^- pairs are produced which travel

under the influence of the field generated by the dipole magnet. These lepton pairs are detected in the pair spectrometer scintillators and microstrip detectors. Upon analysis of the resulting data, the hit positions are used to calculate the energy of the pair, and therefore of the interaction photon.

3.6 The CLAS Detector

The CLAS [56] detector is comprised of six superconducting magnets and multi-layered detector subsystems, geometrically split into six sectors. These different subsystems give information on the charge, momentum, mass and velocity of the particles from the reaction taking place. The toroidal field generated by the magnets focus all particles within the detector giving rise to a near 4π accep-tance. The presence of the magnetic coils themselves result in certain regions having no acceptance. The multilayered six sector structure of CLAS can be seen schematically in figure 3.6. Figure 3.7 is a photograph of CLAS with its *clamshell* open.
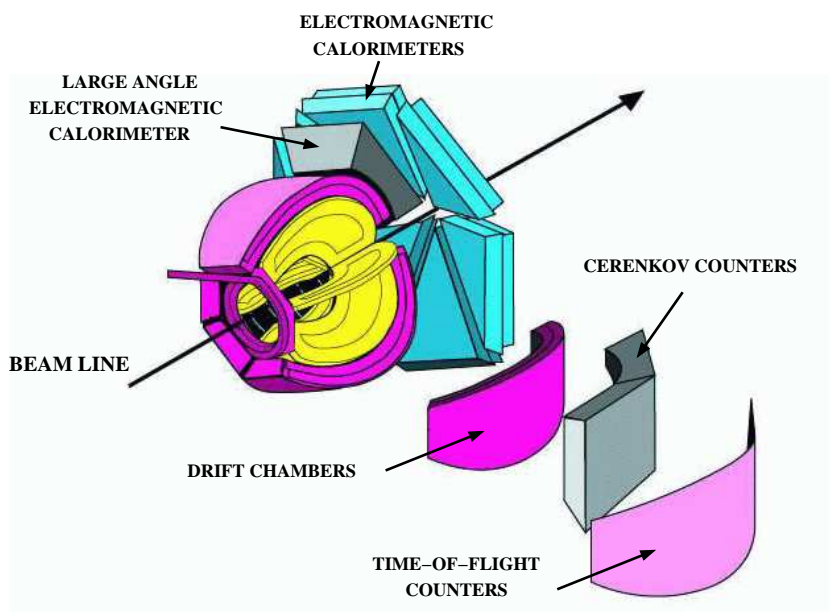
Figure 3.6: An exploded view of the multilayered detector subsystems of CLAS.

The detection sequence in CLAS (for example of a charged particle) is as follows. After production within the target, the charged particle passes through the start counter, where the signal generated allows for an event start time to be defined. Beyond the start counter, the charged particle passes through the three drift chamber regions. Its initial and final directions upon entering and leaving

Figure 3.7: The CLAS detector with open *clamshell*. The six sector configuration of the drift chambers (region 3 visible) can be seen, along with time of flight scintillator paddles (left of centre).

the drift chambers are determined in region 1 and 3 respectively. Region 2 of the drift chambers is situated in the region of maximal toroidal field strength, hence the curvature of the charged particle as it passes through this region determines its momentum. (The trajectory of the curvature of the particle depends on its charge and the polarity of the toroidal magnetic field. In the case of the G10 experiment, the polarity was positive, hence positively charged particles curved outward away from the beamline and negatively charged particles curved inward toward the beamline). After passing through the drift chambers (this portion of the detection sequence is referred to as *tracking*), the charged particle now enters the time of flight (TOF) subsystem. The flight time of the particle from the target to this time of flight subsystem is used to calculate it's velocity. This velocity along with the momentum determined previously in the drift chambers, allows for the charged particle's mass to be determined (particle identification). If the particle was neutral, its detection and identification would occur in the electromagnetic calorimeters. For subsequent physics analysis, all particles originating from a single event are identified on the basis of timing information and vertex positions. The associated photon for the event is found from timing information in the photon tagger.

3.6.1 The Superconducting Torus Magnet

The toroidal magnetic field within CLAS is generated by six superconducting coils mounted around the beamline to create six $\sim 60^o$ sectors. The configuration of the coils relative to the beamline is shown in figure 3.8. The magnetic field generated by these coils is always transverse to the momentum of the particle. The maximum intensity of this field is $\sim 2\,T$. During the G10 experiment, data were taken with both high and low field settings ($3375\,A$ & $2250\,A$). The positive polarity of the main torus magnet explains why the low field setting gives rise to an increased acceptance of negatively charged particles. At this field setting, less particles are lost at forward angles down the beamline hole in the CLAS detector.
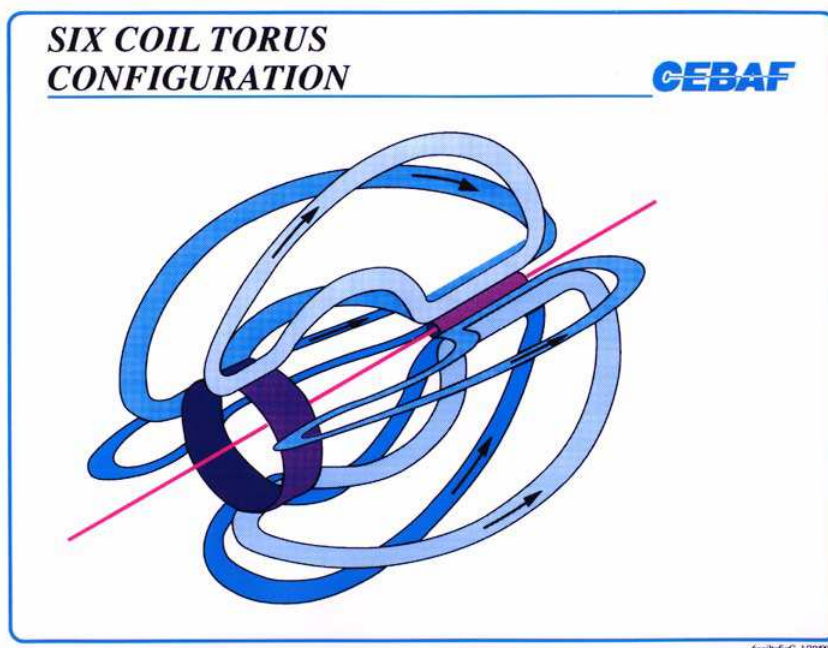
Figure 3.8: The six magnetic coils of CLAS.

A mini torus surrounding the target can be used for electron running to prevent low momentum Mϕller electrons entering region 1 of the drift chambers.

3.6.2 Start Counter

In order to provide a reference start time of a particle interaction, a start counter [57] surrounds the target within CLAS. This start counter is constructed of six pieces of scintillator conjoined in a coupled paddle configuration which effectively provides three sectors of scintillator in the forward direction. Figure 3.9 shows one of these six scintillators (one half of a coupled paddle) surrounding the tar-

get. Each of these coupled paddles is arranged so as to geometrically map onto two sectors of CLAS. The signal from any detected charged particle within the scintillator is read out via a light guide and a photomultiplier tube (PMT) attached in the backward direction, resulting in six channels, each corresponding to the six sectors of CLAS. These six channels also have charge-to-digital converters (QDC) and time-to-digital converters (TDC) which provide energy and timing information of the interaction in the scintillator.
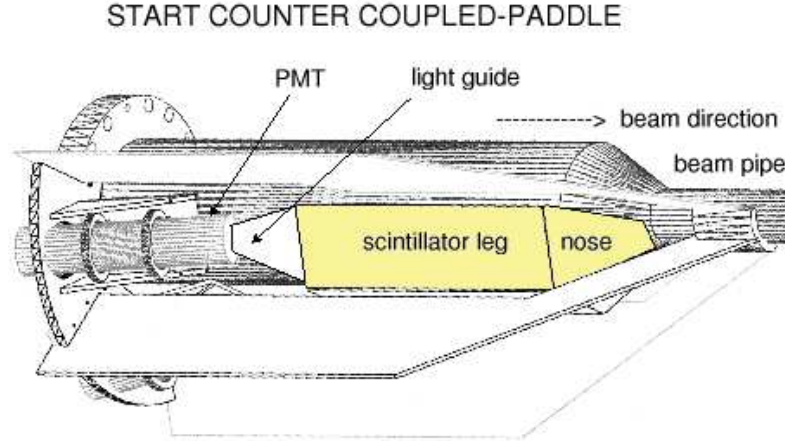
Figure 3.9: The CLAS Start Counter: showing one half of a coupled paddle.

Timing resolution of around $260\,ps$ can be obtained after calibration and the angular coverage is, apart from the forward direction, exactly the same as that of the time of flight subsystem. Using the timing information from the start counter a well defined start time can be assigned to an interaction, which simplifies the identification of the RF beam bucket from which the associated photon was produced. The start counter information is also used in conjunction with the drift chamber tracking and time of flight measurements to provide a means of particle identification.

3.6.3 Drift Chambers

The drift chambers [58] in CLAS, which detect and measure the momentum and trajectory of charged particles, are split into three regions and arranged between the coils of the superconducting torus, as shown in figure 3.10 (left). Each one of these drift chamber regions is divided into six by the torus coils, which leads to eighteen drift chamber segments in total. Figure 3.10 (right) shows a representation of one of these segments. Each region has $\sim 60^{o}$ azimuthal (ϕ)

coverage and is constructed with a curvature designed to maintain the wire plane parallel to the magnetic field.
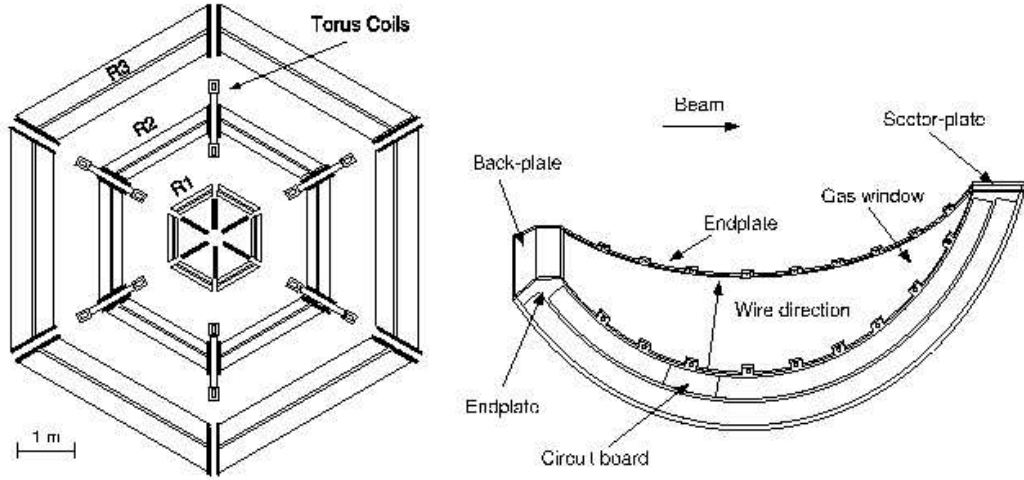
Figure 3.10: Cross section of the CLAS drift chambers (left), and a CLAS drift chamber segment (right).

Each region consists of two superlayers which in turn contains six layers of wire each. These wire layers are arranged in such a way as to produce a repeating hexagonal cell pattern of one sense wire maintained at a positive voltage surrounded by six field wires maintained at a negative voltage. The diameter of these cells is different for each region (region 1 cell diameter is $0.7\,cm$, region 2 cell diameter $1.5\,cm$ and region 3 cell diameter $2.0\,cm$), and their resolution varies from $\sim 310 - 380\,\mu m$. The first superlayer, known as the axial superlayer, is arranged axially to the magnetic field. The second layer, known as the stereo superlayer, is arranged with a 6° orientation offset to the axial superlayer and provides the azimuthal measurement of the track trajectory. The chambers are filled with a gas mixture containing 90% argon - 10% carbon dioxide (CO_2).

When operational, a potential is applied to the layers within the drift chambers. Consequently, any charged particle entering the drift chamber will ionise the gas molecules and the electrons will avalanche onto the positive sense wire. The drift distance and therefore the particle's position can be determined by measuring the drift time of the electrons onto this sense wire. Multiple drift distance measurements of the particle as it passes through all three drift chamber regions results in the tracking of the particle's trajectory, as can be seen in figure 3.11.

Region 1 of the drift chambers lies closest to the target within the nearly field-free region of the torus. Consequently, this region is used to provide the initial trajectory information (direction) of the charged particle as it enters the drift
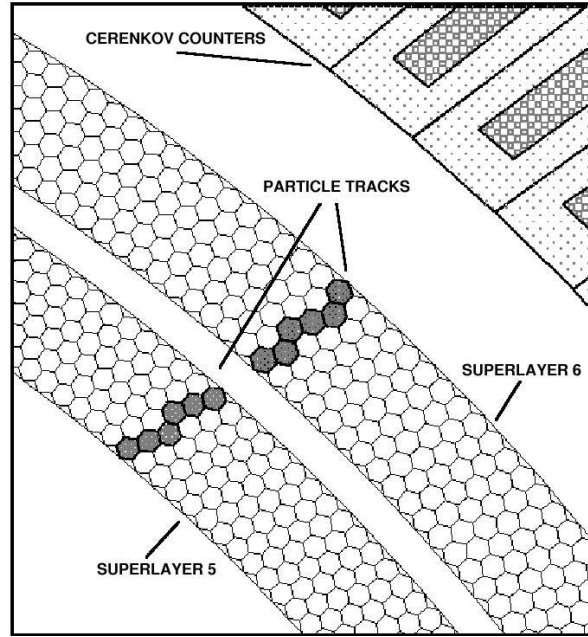
Figure 3.11: Particle track passing through the two superlayers of a drift chamber region.

chambers. Similarly region 3 lies outwith the torus coils, again in a region of low magnetic field, and provides the final direction information of the charged particle as it leaves the drift chambers before passing onto the outer lying subsystems, TOF etc. Region 2 is located in the region of strongest magnetic field between the torus coils. Within this region of strong magnetic field, the curvature of the particle's trajectory will be maximal, hence best momentum resolution is attained in region 2. The measurements of the initial and final track directions, combined with the measurement at maximal track curvature, allow for the determination of the charged particle's trajectory and momentum.

3.6.4 $\check{C}erenkov$ **Counters**

The $\check{C}erenkov$ counters [59] are a forward angle ($\Theta < 45^o$, where Θ is the polar angle relative to the CLAS beamline) detector subsystem only used in electron running. When operating in electron running, they separate pions from electrons and also trigger on electrons. The device consists of mirrored chambers filled with perflurobutane gas which has a refractive index of ~ 1.002 and ended by a Winston cone and PMT. When a charged particle traveling faster than the speed of light in the gas enters the chamber, $\check{C}erenkov$ light is emitted and collected by the Winston cone. The opening angle of the emitted cone of $\check{C}erenkov$ light

depends upon the velocity of the particle and can be used for identification of, and differentiation between, pions and electrons.

3.6.5 Time of Flight Scintillation Counters

The time of flight [60] subsystem covers the fiducial volume of the CLAS detector which corresponds to lab angles ranging from $8^o \leq \Theta \leq 142^o$ and a total area of $206\,m^2$. Coverage of this active region is achieved by using 57 scintillator paddles per each of the six sectors, with the last 18 paddles coupled into nine logical pairs, giving a total of 48 logical counters/channels per sector. All of these scintillators are $5.08\,cm$ in thickness although their lengths and widths vary depending upon position. The lengths vary from a minimum of $32\,cm$ at forward angles ($\sim 8^o$) upto a maximum of $445\,cm$ at a lab angle of $\sim 76^o$, and the widths either $15\,cm$ at forward angles or $22\,cm$ at large angles. These dimensions where chosen in order to satisfy both the consideration of spatial coverage and achievable timing resolution. The intrinsic timing resolution measured during cosmic ray tests was found to be $\sigma \sim 80\,ps$ for the short scintillators and $\sigma \sim 150\,ps$ for the long. Figure 3.12 shows a schematic view of the time of flight scintillators in a single sector. Note the grouping of the scintillators into a four panel configuration which allows for the required polar angle coverage.
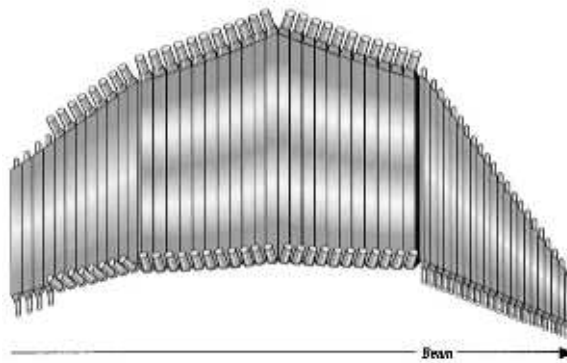
Figure 3.12: Schematic view of a single sector time of flight (TOF) configuration.

Each of the scintillators has a PMT attached at either end and the signal is readout by both an QDC and TDC. For any particle passing through CLAS, the flight time from the target to the TOF is used to calculate its velocity. This velocity along with the measurement of momentum obtained from the drift chambers allows the particle's mass to be determined using the relation $\beta = \frac{p}{E}$. Indeed, it is TOF mass that is used for initial particle identification in this analysis.

3.6.6   Electromagnetic Calorimeters

The electromagnetic calorimeters [61] are primarily used for the detection of neutral particles such as photons with energies above $0.2\,GeV$ and neutrons. They are also capable of detecting electrons with energies above $0.5\,GeV$. All six sectors of CLAS have an electromagnetic calorimeter subsystem with a polar angle coverage $8^o < \Theta < 45^o$ and consist of thirty-nine layers of scintillator and lead in a sandwich composition. The scintillator is $10\,mm$ in thickness and the lead is $2.2\,mm$. Interacting particles in the scintillator-lead sandwich will lose energy by the radiation of a bremsstrahlung photon (which in turn induces e^+e^- pair production thus more bremsstrahlung down to ionisation energies) typically within one radiation length and produce an energy shower. This energy is detected in the scintillators and is used to identify the interacting particle based upon both the positional information and the energy deposited. The scintillator-lead construction of the electromagnetic calorimeter is shown in figure 3.13. As can be seen, each layer has the form of an equilateral triangle in order to cover the hexagonal geometry of CLAS. Also apparent is the successive 120° rotation in the orientation of the scintillator strips in each layer, labeled as u, v and w planes. This recurring three plane configuration gives rise to stereo information on the position of the deposited energy in the scintillator.
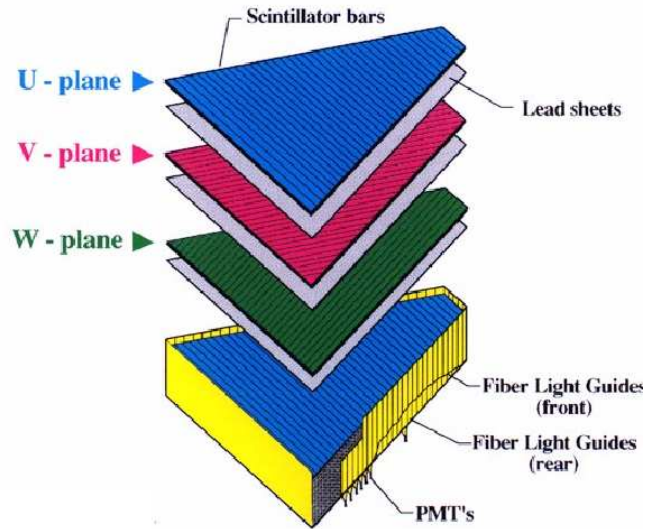
Figure 3.13: Schematic view of the electromagnet calorimeter, showing three orientations of scintillator.

3.6.7   Large Angle Electromagnetic Calorimeters

In the previous section 3.6.6, the role of the electromagnetic calorimeters was described. However, depending upon the experiment in operation, one might wish to extend the detection capabilities of the electromagnetic calorimeters to more backward angles. This capability is achieved by the large angle electromagnetic calorimeters in sectors 1 and 2 only and providing polar angle coverage $45^o <$ $\Theta < 70^o$. The interaction processes and detection principles are the same as for the electromagnetic calorimeters described previously. Again these are composed of scintillator-lead sandwiches, with the scintillator being $15\,mm$ in thickness and the lead $2\,mm$. In total there are thirty-three layers successively orientated at 90° to each other .

3.7   Downstream Devices

Situated downstream of the CLAS detector are two devices whose purpose is to monitor the quality of the photon beam. Detailed information on these is given in ref. [53]. These two devices are known as the Pair Counter (PC) and the Total Absorption Shower Counter (TA(S)C).

The pair counter is a device used as a backup to measure full beam intensity. A thin converter produces e^+e^- pairs which are detected in a single scintillator with four overlapping scintillators behind. Importantly, this device also has a charged particle veto which eliminates background from CLAS.

The second of the downstream devices is the total absorption shower counter. The TA(S)C is the primary device for the measurement of photon flux, *GFlux* (see section 6.4), and consists of four lead glass blocks with an absorption efficiency of almost 100%. Consequently, the TA(S)C cannot be operated at beam currents above $\sim 100\,pA$, with a corresponding photon rate of $\sim 10^5\,Hz$, and therefore is used for low intensity normalisation runs.

3.8   Trigger System

The trigger system in CLAS uses logic signals from the detector subsystems to determine whether or not an event is to be recorded and readout. The trigger configuration is set up to maximise the proportion of triggers from events of interest, and minimise those from accidentals or detector noise as well as detector deadtime. The configuration of such a trigger is dependent upon the conditions and needs of the individual experiment. CLAS has a two level (level 1 and level 2)

trigger system which passes or rejects events based on the configuration. The level 1 trigger processes digital signals, via a memory lookup, from the outer detector subsystems, for example time of flight or the electromagnetic calorimeters. The level 2 trigger utilises tracking information from the drift chambers to form a more stringent requirement for the acceptability of an event.

3.8.1 Level 1 Trigger

The CLAS level 1 trigger [62] utilises logic signals from the time of flight, electromagnetic calorimeters and the start counter (which is a requirement for photon running) subsystems along with tagger master-OR (MOR). For electron running the Čerenkov counters form part of the level 1 trigger. This trigger is formed by means of a coincidence between each of these detector subsystems. For the G10 experiment the level 1 condition was configured to require two charged particles per event. Sector based signals from each of the subsystems act as inputs for the level 1 trigger which consists of a three stage memory lookup, see figure 3.14 (note that for this experiment the Čerenkov counters do not form part of the level 1 trigger and their input was replaced with that of the start counter).
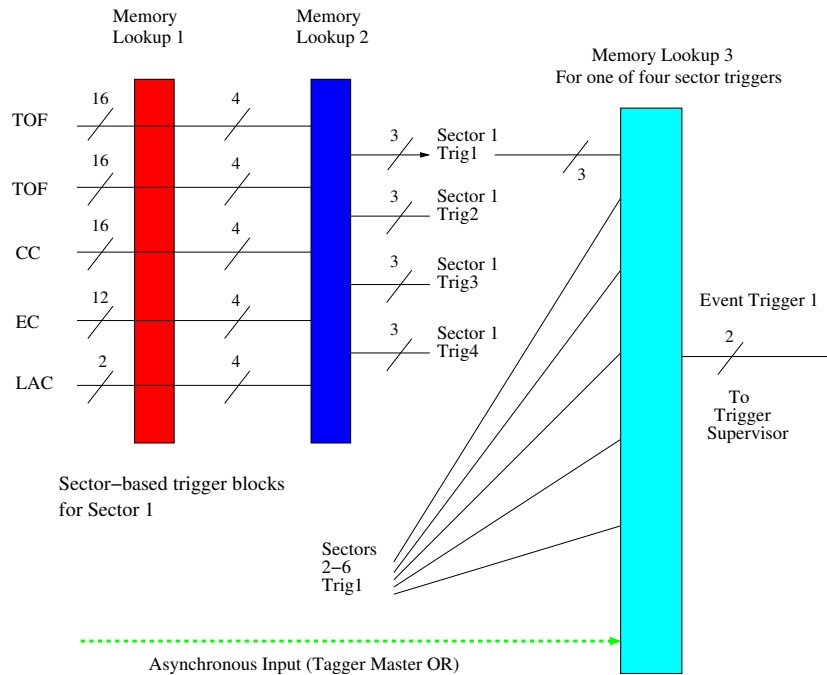
Figure 3.14: Level 1 trigger memory lookup.

Memory lookup 1 takes each of the pre-trigger inputs (62 bits) and maps them into four bits per input. Lookup 2 then reduces these further into four trigger

words, each 3 bits, per sector. The final level 1 trigger stage is memory lookup 3. Here correlations are made between sector events based upon geometrical considerations which account for multi-pronged events, that is to say events with hits in different sectors of CLAS. At this final stage of the level 1 trigger, the tagger master-OR is checked for coincidence before the level 1 trigger is passed to the trigger supervisor (see section 3.8.3).

3.8.2   Level 2 Trigger

It is possible for a level 1 trigger to be obtained from an event with no likely tracks detected in the drift chambers. An example of such an event could be a cosmic ray passing through CLAS. For this reason, the level 2 trigger specifically requires that a likely track is detected in the drift chambers, otherwise the event is rejected. A likely track is defined as one for which track segments are found in three of five drift chamber superlayers, matching an initial template. The level 2 trigger is satisfied with a logical OR from all six sectors or by directly comparing to the geometrical information from level 1. If no likely track is found for any of the six sectors, the event fails level 2 and is rejected.

3.8.3   Trigger Supervisor

The trigger supervisor is the electronics module which issues all common start/stop and clear signals, as well as gates and resets for the detector electronics. It also has the role of placing an event on the data acquisition queue. The supervisor module receives the outputs from both the level 1 and level 2 triggers, although it can be programmed and operated in one of two configurations known as CLASS 1 and CLASS 2. CLASS 1 uses only level 1 trigger output whereas CLASS 2 uses the output of both level 1 and level 2 triggers.

Two trigger configurations were utilised for the G10 experiment:

1. 2 tracks in the drift chambers and 2 hits in the time of flight, with one time of flight hit in coincidence with a hit in the electromagnetic calorimeters.

2. As above but not requiring the EC coincidence, i.e. 2 tracks in the drift chambers and 2 hits in the time of flight.

These two conditions allowed for the clean identification of events with possible physics of interest as defined by the aims of the experiment.

3.8.4 Data Acquisition

Beyond the trigger supervisor, the process of data acquisition (DAQ) begins. The system used at Jefferson Lab is known as CODA [63]. Event fragments, which consist of tabulated and labelled digitised values, read out from each detector subsystem are sent to an online acquisition computer. Here the event fragments are processed in the Event Builder which collates each fragment and converts the resulting data word into BOS [64,65] format. Next the Event Transport transfers the complete event to shared memory where it can be used for online analysis or data monitoring. Figure 3.15 shows an online reconstruction of a hadronic event using CLAS Event Display (CED). Finally, the Event Recorder writes the event to a RAID[1] array from where it is transferred via a fibre link to the JLab Tape Silo and becomes available for offline analysis.
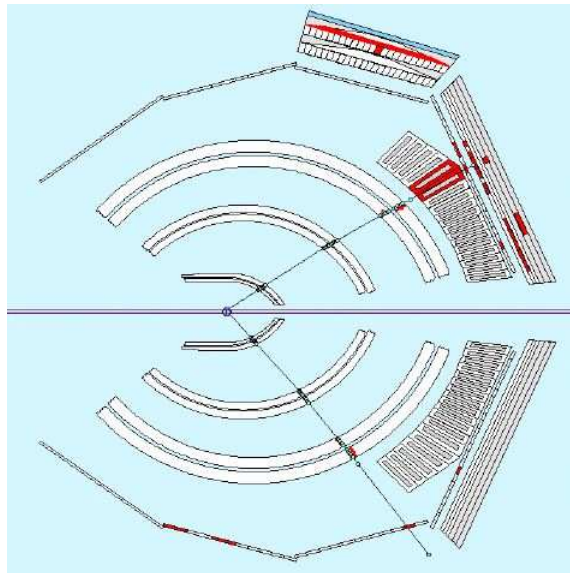
Figure 3.15: An online reconstructed hadronic event in CLAS, displayed using CED.

The maximum event rate is approximately $4\,kHz$, however G10 ran with an event rate of $\sim 3.5\,kHz$ in order to maintain a DAQ livetime of $\sim 85\%$ and therefore maximise overall efficiency.

---

[1]RAID - Redundant Array of Independent (Inexpensive) Disks. D. A. Patterrson *et al*, SIGMOD Conf. 1988.

Summary

This chapter detailed the experimental apparatus and setup utilised to conduct the G10 experiment. Before any analysis can be performed, it is necessary to calibrate the detector subsystems and convert the output to data in a meaningful physical format (e.g. time, position, momentum). The following chapter describes the processes involved in the calibration of the detector subsystems and data reconstruction.

Chapter 4

Data Processing and Calibrations

In order to perform physics analysis of the experimental data acquired during the run period, it is necessary to convert the raw signal information from the detector subsystems into meaningful physical values. These physical values take the form of timing, position, energy and/or momentum of the detected particles. The initial stages of this conversion process require the undertaking of two parallel tasks; data reconstruction, known as *cooking*, and calibration of the detector subsystems. Each detector subsystem has an offline software package to produce calibration constants which are used in the *cooking* process. Several iterations of these parallel tasks are necessary in order to refine the data into the final form for physics analysis. The author had the overall responsibility for the *cooking* of the G10 data, as well as performing the photon tagger calibration.

4.1 Run Conditions and Data

The following is a summary of the G10 experiment run conditions:

- Continuous-wave electron beam with energy (E) $3.776\,GeV$ and current approximately $25\,nA$.

- Tagged photon energy range from $0.8 - 3.6\,GeV$.

- Bremsstrahlung photons produced on a $10^{-4}\,X_0$ radiator (X_0 is radiation length).

- Targets of liquid deuterium LD_2 and liquid hydrogen LH_2: $24\,cm$ length and $40\,mm$ diameter target cell positioned at $Z = -25\,cm$ (upstream of CLAS centre).

- CLAS configuration of ST (start counter), DC (drift chambers), TOF (time of flight scintillators), EC (electromagnetic calorimeters) and LAC (large angle electromagnetic calorimeter).

- Torus magnet settings of $2250\,A$ (Low Field) and $3375\,A$ (High Field). The $2250\,A$ setting allowed increased acceptance of negative particles for the inclusive analysis, and the $3375\,A$ setting provided similar geometrical acceptance and single track resolution as the original G2a experiment.

- 2 Trigger configurations:
  $(TOF \times EC)^i \times TOF^j$ and $TRK^i \times TRK^k$; 2 tracks and 2 hits in the time of flight, one in coincidence with the electromagnetic calorimeters.
  $TOF^i \times TOF^j$ and $TRK^i \times TRK^k$; as above but not requiring the hit in EC.

Given the above run conditions, a large amount of data were acquired, satisfying the high statistics nature of the proposal. The data are summarised below:

- Production data on LD_2 at torus current $2250\,A$ gave a total of 4710×10^6 triggers and an integrated electron charge of $51.64\,mC$.

- Calibration data on LH_2 at torus current $2250\,A$ gave a total of 133×10^6 triggers and an integrated electron charge of $2.92\,mC$.

- Production data on LD_2 at torus current $3375\,A$ gave a total of 5000×10^6 triggers and an integrated electron charge of $48.78\,mC$.

- Calibration data on LH_2 at torus current $3375\,A$ gave a total of 267×10^6 triggers and an integrated electron charge of $4.49\,mC$.

- Integrated luminosity of approximately $50\,pb^{-1}$ collected during the run period.

4.2 CLAS Output

Output (see section 3.8.4) from the CLAS detector subsystems is transferred and collated on an event-by-event basis within a dynamic memory structure (FORTRAN 77) known as BOS (Bank Operating System) [64, 65]. Each detector subsystem within CLAS has at least one BOS bank containing the relevant raw output. These banks can then be accessed using function calls for the purposes of calibration and *cooking*. Typically, the output of each data run is split into

files of $\sim 2\,Gb$ in size, and one standard data run (~ 2 hours for G10) will give rise to ~ 25 files. During uninterrupted *production* running, it can be possible to acquire $\sim 10 - 12$ data runs per day.

4.3   Data Reconstruction / *Cooking*

The process of data reconstruction or *cooking* [66], converts the raw BOS bank outputs (see sect. 3.8.4) into reconstructed or *cooked* BOS banks. A *cooked* bank is a collection of data words containing detector subsystem information which is now in physical format (e.g. position, time, momentum). This process utilises a software package called RECSIS (REConstruction and analySIS package). The raw data are first calibrated in the appropriate manner dependent upon the detector subsystem, which results in a set of calibration constants. Each of these constants is stored in a centralised MySql [67] database and linked to RECSIS via an experiment specific run index. When adequate calibration constants have been produced they are used to adjust the reconstructed physical information in the BOS banks and one iteration of data *cooking* is complete. The previously mentioned adjustment of the bank information accounts for aspects such as detector position, trigger times and offsets of each detector subsystem with respect to the others.

For the G10 experiment, 2 passes of *cooking*, each consisting of multiple versions were required in order to produce the final high quality data for physics analysis. (Pass refers to the current iteration of the overall process, while version refers to current status of the calibrations.) Data processing in this manner is computationally intensive and took nine months of constant running on the JLab computing farm with, ~ 12200 raw input and ~ 120000 subsequent output files.

4.3.1   Quality Monitoring

One vital requirement during the data reconstruction process is the monitoring of the subsequent outputs. For G10 the author implemented a package called CSQL [68], which allows for the storage and visual monitoring of the *cooking* process results via a web interface. The package was linked to RECSIS and during processing, various outputs of interest were monitored on a run by run basis and over entire versions or passes. Consequently, data runs which required further refinement could readily be identified. An example of a CSQL monitoring display, showing normalised number of protons versus run number, can be seen in figure 4.1. The main purpose of this monitoring process is to check the drift of
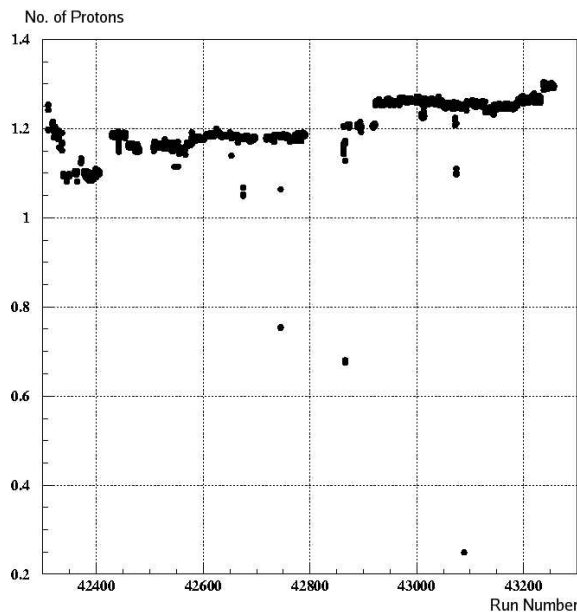
Figure 4.1: Example of a CSQL monitoring display.

calibration constants, and highlight any other detector problems throughout the experimental run.

4.4 Subsystem Calibrations

As was mentioned previously, each of the detector subsystems is required to be calibrated in order to refine the data for physics analysis. Of particular importance with CLAS are timing calibrations, since timings are the basis of particle identification (PID) and the determination of particle momenta. Furthermore, the determination of the correct beam bucket, from timings, is vital in order to identify the event photon. In this section brief overviews of the calibration principles and methods for each of these subsystems will be presented. More detail will be given in relation to the calibration of the photon tagger, for which the author was responsible.

The overall calibration procedure has the following steps:

1. Calibration of the start counter and alignment to the time of flight.

2. Calibration of the photon tagger, the beam RF time and alignment to the time of flight.

3. Calibration of the time of flight.

4. Calibration of the drift chambers.

5. Calibration of the electromagnetic calorimeters with respect to the time of flight.

These steps are looped over many times until satisfactory calibration constants are converged upon and acceptable physics data reconstructed. In order to ensure these constants are satisfactory throughout the entire experimental run range, calibrations are conducted on reference runs which are chosen at regular intervals spanning the entire range. Given the necessity for high quality particle identification and accuracy of reconstructed masses (invariant and missing) within the G10 analysis, these references were taken to be at least every ten runs. However, in ranges where the calibrations were deemed to have drifted, as determined through the monitoring process explained previously, the calibrations were carried out often on a run by run basis.

4.4.1 Start Counter Calibration

The calibration of the start counter (see section 3.6.2) is performed in two stages, followed by the alignment of the start counter time to the time of flight subsystem. The first stage of the calibration process involves internally aligning each pair of coupled paddle scintillators, whilst the second stage aligns the three pairs with respect to each other.

When a hit is registered in a coupled paddle pair, two TDC timings result (T_1 and T_2). The difference between these two timings should be a constant for real physical events. These real events are selected and their timing distribution ($T_1 - T_2$) is plotted and, by the adjustment of a constant for each paddle, is centred on zero. This internal alignment procedure is carried out for each of the three coupled paddle scintillator pairs.

The second stage requires the alignment of each of the now internally aligned pairs relative to one another. In order to do this, an external reference time is required with which to compare the start counter time of each pair. A tagger T-counter provides this external reference time, and for each coupled paddle pair the start counter time is subtracted from this T-counter time. Again the constants for each coupled paddle pair are adjusted (now by the same amount) in order to align the main peak of this time difference distribution, with the main peaks from the distributions of the other pairs. This alignment need not be centred on a timing difference of zero since this is an internal calibration of the start counter subsystem and will be accounted for in the photon tagger and time of

flight calibrations. When all three pairs are aligned in this way, the start counter has been calibrated.

The final step in the overall start counter calibration is the determination of a constant time offset, known as *st2tof*. As discussed in sections 3.6.2 and 3.6.5, the start counter time must be aligned to the time of flight subsystem in order to obtain accurate time of flight measurements, since the start counter provides the event start time. By subtracting the vertex time of a track as measured by the time of flight, from the vertex time of the track as measured by the start counter, and adjusting the resulting distribution's offset to be centred on zero, this alignment of start counter to time of flight is achieved. The final determination of *st2tof* cannot be completed until the drift chamber and time of flight calibrations are deemed to be complete. Consequently, the value changes after each iteration of the overall calibration procedure as previously defined (see section 4.4).

4.4.2   Photon Tagger Calibration / Beam RF

Calibration procedures for the photon tagger (see section 3.3) and beam RF are detailed in Refs. [69, 70]. This section contains a brief description of the stages involved, along with histograms which represent the quality of the G10 calibration (the fact that this procedure is described in greater detail compared with the others, reflects the author's responsibility for this process).

Conceptually, the calibration of the tagger is as follows. The TDC values from the E-counters and T-counters PMTs are required to be converted into times. This is achieved by calculating and storing some calibration constants ($ps/channel$) for each TDC. These values are then used in the conversion of the TDC channels into times. Once these times are determined, geometrical matching between E-counter hits and T-counter hits is performed. This matching is only performed if the E-counter and T-counter hits represent a certain combination, based on the overlap of the E and T focal planes in relation to typical electron trajectories, as shown in figure 4.2. This combination must be one in which the electron did not scatter after interacting with the radiator foil. At this same stage of geometrical matching, a timing coincidence between the E-counter hit and T-counter hit is also required. Determination of the final timing involves using the T-counters, which are individually corrected for offsets, to identify the $2\,ns$ beam bucket. Finer ($< 2\,ns$) corrections to this timing are achieved using the RF machine time. The remainder of this section details the procedures involved in this calibration.

The process of this calibration can be broken down into the following distinct
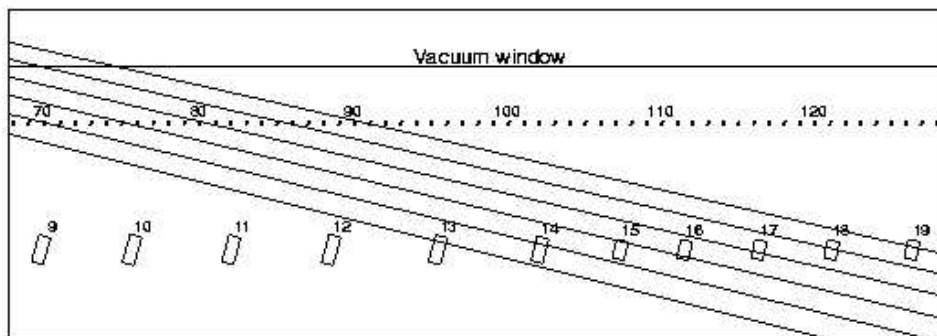
Figure 4.2: Schematic representation of a portion of the tagger hodoscope. The orientation of the scintillators (counters) in both the E and T plane can be seen, as can the overlap of the E-counters and T-counters relative to electron trajectories.

stages, each of which produce calibration constants to be used in the reconstruction/*cooking* process:

1. T-counter TDC Left-Right slope calibrations.

2. Base peak calibrations.

3. RF timing adjustments, C_i's.

4. Tagger to time of flight offset.

Once the photon tagger is calibrated and the constants obtained, an output bank known as **TAGR** is produced in the *cooking*. This bank contains time, energy and T and E-counter information. It should be noted that in order for a tagger event to be properly reconstructed, E-T coincidences are matched via a lookup table. Furthermore, this E-T coincidence is required, via hardware, to be within $20\,ns$. Figure 4.3 shows this coincidence, T-counter time minus E-counter time versus E-counter number (E-id). When a hit falls within this coincidence window, the timing of the photon is determined by the T-counter time and the RF.

At this point one can look at the RF offset calibration. The machine RF time is measured via a PMT situated at the entrance to Hall B. The resulting TDC signal (RF TDC time) is pre-scaled by a factor 40 giving rise to a signal with period $80\,ns$. A good RF calibration should result in the difference between tagger time (TTAG), for all 121 T-counters, minus RF corrected tagger time (TPHO) equal to zero. Figure 4.4 shows this difference plotted against RF TDC time, after the completed calibration process. Details of each stage in this process are given in the following subsections.
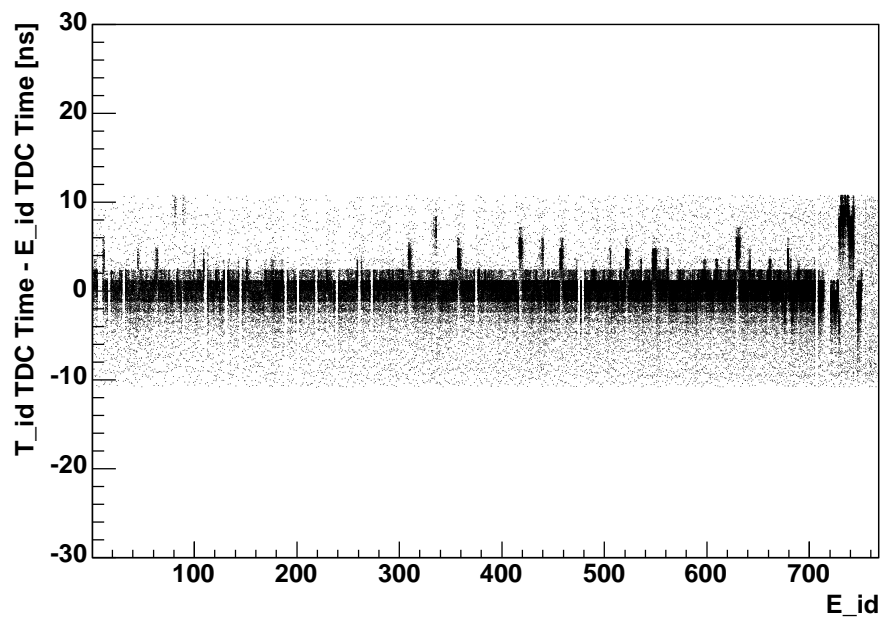
Figure 4.3: E-T Counter timing coincidence for a well calibrated G10 run.
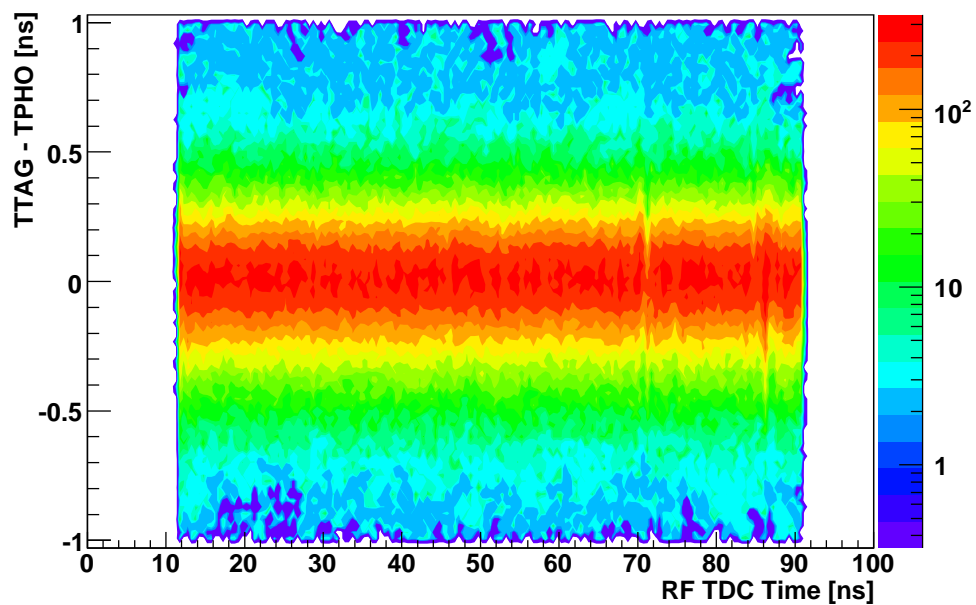
Figure 4.4: Calibrated RF time for a G10 run.

4.4.2.1   T-counter TDC Left-Right Slope Calibration

It is necessary to correct the timings obtained from the left and right TDCs on each T-counter. This process involves making a comparison between the time as calculated by both TDCs and correcting them relative to each other and the RF, on a counter by counter basis. The photon tagger calibration software plots and measures two slopes β_{LR} and β_{RF}, from which the corrections can be determined, as defined below:

β_{LR} is the slope of $\frac{<t_L - t_R>}{2}$ versus t_{mean}

β_{RF} is the slope of $< t_{mean} - t_{eb} >$ versus t_{mean}

where, t_L and t_R are the measured left and right TDC times respectively, t_{mean} is the mean of these two times ($\frac{<t_L + t_R>}{2}$) and t_{eb} is the electron bucket time which produced the photon.

Calculation of the new/corrected slope constants (the multiplicative factor which converts TDC channel to ns), S_L and S_R, uses the following definitions:

$$S_L = s_l \times \frac{1}{(1 - \beta_{LR})(1 - \beta_{RF})} \simeq s_l \times (1 + \beta_{LR})(1 + \beta_{RF}) \qquad (4.1)$$

$$S_R = s_r \times \frac{1}{(1 + \beta_{LR})(1 - \beta_{RF})} \simeq s_r \times (1 - \beta_{LR})(1 + \beta_{RF}) \qquad (4.2)$$

where, S_L and S_R are the new slopes for the left and right TDCs respectively and s_l and s_r are the pre-calibration slopes for the left and right TDCs respectively. A well calibrated T-counter should have a flat slopes at zero time difference, when plots of $\frac{<t_L - t_R>}{2}$ versus t_{mean} and $< t_{mean} - t_{eb} >$ versus t_{mean} are studied. Figure 4.5 shows the results of a good calibration of these TDC slopes. Note that the slopes for all T-counters are shown using an arbitrary scale, the times are ns.

4.4.2.2   Base Peak Calibrations

The tagger TDCs operate in what is known as common-start self-triggered mode. That is to say, they will start to measure time when either the CLAS level 1 trigger fires (common-start) or when a hit is recorded on a T-counter (self-triggered). The base peak calibration constant is the mean position of the TDC peak since either left or right TDC will register the first time and become the trigger. Consequently, the actual time measured by the T-counter TDCs is the TDC time with this calculated base peak constant subtracted, and thus corrected for the signal delay.
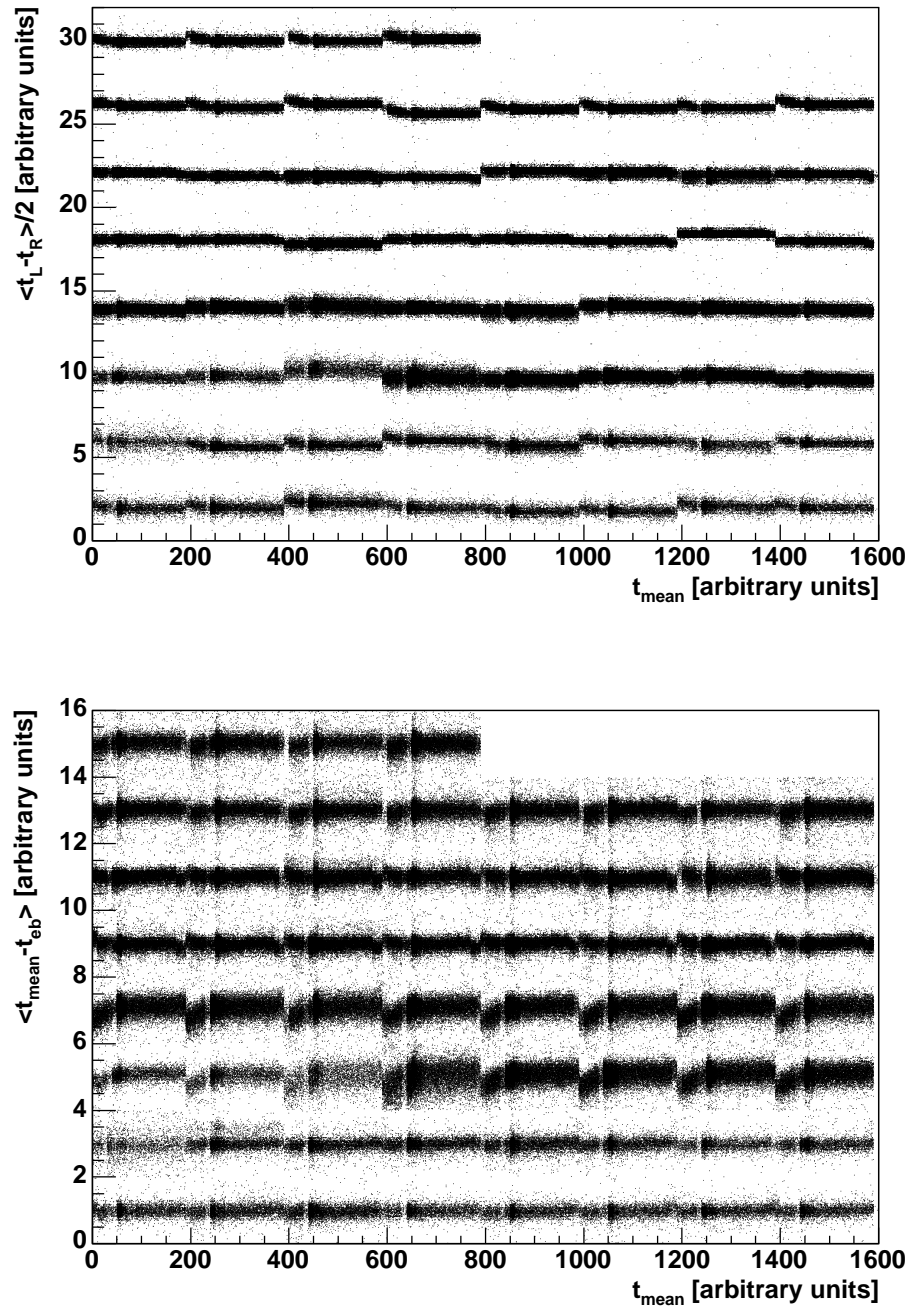
Figure 4.5: A G10 TDC slopes calibration for one run.

The constants are calculated using the following definitions for each T-counter T_i ($i = 1...61$):

$$< Peak(L)_i >=< TDC(L)_i > - < T(L/R)_i > \qquad (4.3)$$

$$< Peak(R)_i >=< TDC(R)_i > - < T(R/L)_i > \qquad (4.4)$$

where, $Peak(L)_i$ and $Peak(R)_i$ are the new constants (absolute peak positions) for the T-counter TDCs (left and right respectively), $TDC(L)_i$ and $TDC(R)_i$ are the measured TDC times for the left and right respectively and $T(L/R)_i$ and $T(R/L)_i$ are related to the relative time delays between the left and right (right and left) TDCs. This relative time delay accounts for physical factors such as fixed cable delays. The better the hardware alignment, the shorter the timing window for coincidences can be made and the better the real to random ratio. Even with perfect alignment, the timing window will have to be at least as wide as the resolution of a single channel.

4.4.2.3 RF Timing Adjustments, C_i's

After the above stages have been completed, it is now important to identify the correct RF beam bucket from which the reconstructed hit was obtained. The available RF time (see figure 4.4) is actually given relative to the trigger time, t_{RF}. Therefore, the information which it provides concerns the phase shift between the machine RF time, with period $2.004\,ns$, and the trigger. The time of the tagged photon, t_{TPHO}, is given by the relation:

$$t_{RF} = t_{TPHO} + k_{event} \times 2.004 \qquad (4.5)$$

where, k_{event} is the RF beam bucket offset and determined on an event by event basis. The method of determining t_{TPHO} will now be explained.

In order to improve the timing alignment described in the previous section 4.4.2.2, a reference detector is chosen. The choice for the G10 experiment was the start counter, which is typical for photon running, since this is the first subsystem which will detect reaction products in CLAS. Using the time, t_{REF}, from the reference detector, the misalignment of the T-counters at the trigger level can be determined and corrected for by the application of a constant for each T-counter C_i^{REF} ($i = 1...121$), defined by the following relations:

$$C_i^{REF} =< t_{mean}^i - t_{REF} > \qquad (4.6)$$

$$C_i^{REF} = (<D_i> + <T_i>) - <D_{REF}> \qquad (4.7)$$

where, t_{REF}^i is defined previously, D_i is the delay between the production of a tagged photon and the signal output of the T-counter, T_i is the delay for the output signal to trigger and D_{REF} is the time delay between the photon production and the TDC stop signal. Figure 4.6 shows the distribution of $t_{mean} - t_{REF}$ for all T-counters as a function of T-counter number (T_id).
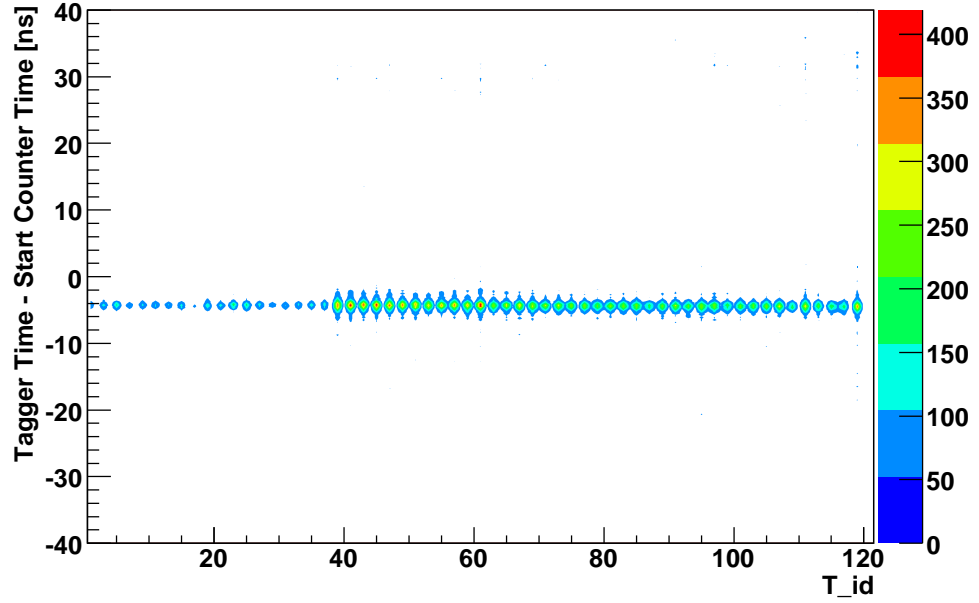
Figure 4.6: A G10 C_i^{REF} calibration for one run.

The procedure so far has utilised the start counter as a reference, however ideally one would reference the timing to the RF which is more accurate, having a resolution of $\sim 80\,ps$. In order to use the RF as a reference, the RF phase shift for each T-counter must be determined and accounted for by the constant C_i^{RF}, defined as:

$$C_i^{RF} = <D_i> + <T_i> - <t_{eb}> + k_i \times 2.004 \qquad (4.8)$$

where, k_i is an integer which can be different for each T-counter. Figure 4.7 shows the distribution of tagger time minus RF time for all T-counters, which is used to calculate C_i^{RF}.

Having now calculated the values of C_i^{REF} and C_i^{RF}, the value of k_i can be determined and consequently the exact C_i calibration constant for each T-counter
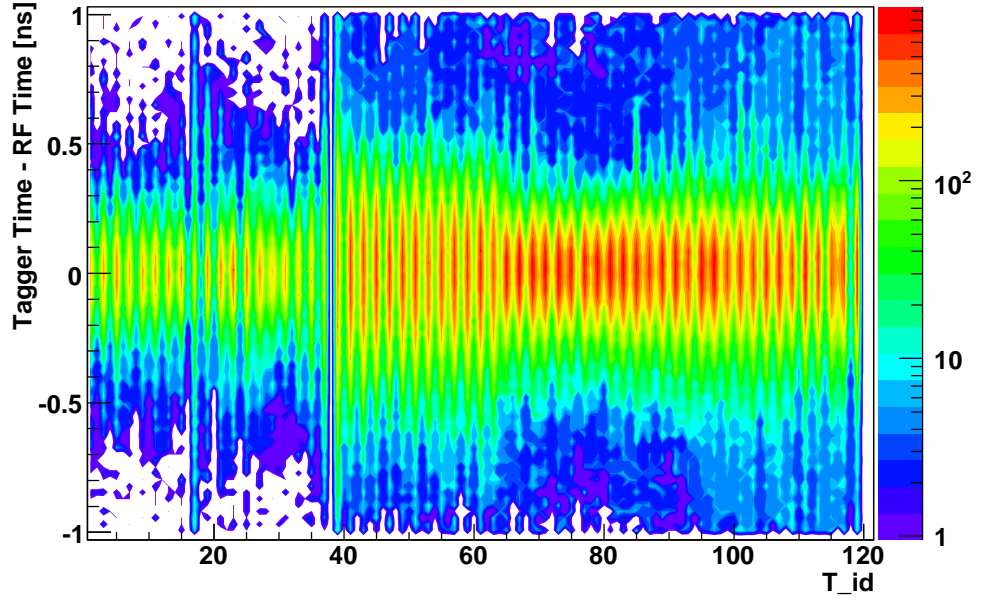
Figure 4.7: Alignment of tagger time to RF time for a G10 run.

obtained using the following relations:

$$C_i^{REF} - C_i^{RF} = - <D_{REF}> + <t_{eb}> -k_i \times 2.004 \tag{4.9}$$

$$C_i = <D_i> + <T_i> - <t_{eb}> \tag{4.10}$$

$$C_i = C_i^{RF} - k_i \times 2.004 \tag{4.11}$$

Finally, after completion of the above procedures and calculations, two times for an event are made available in the TAGR bank which (after aligning to the time of flight, see next section 4.4.2.4) can be used in subsequent physics analysis. The first is the tagger time reconstructed on an event by event basis t_{TTAG}, and the second is the real time of the RF bucket which is considered as being the photon time t_{TPHO}. These are defined in the following way:

$$t_{TTAG}^i = t_{mean}^i - C_i \tag{4.12}$$

$$t_{TPHO} = t_{RF} - k_i \times 2.004 \tag{4.13}$$

The photon tagger timing and beam RF timing are now calibrated and aligned

(again see figure 4.4).

4.4.2.4 Tagger to Time of Flight Offset

When performing physics analysis of photoproduction data, the time associated with the tagged photon should be defined as the time for the photon to reach the centre of the CLAS target (the assumed interaction point). This time is relative to the CLAS detector subsystems and can be defined, since the RF timing is now independent of the T-counter signal. The principles and method used to determine this tagger to time of flight offset, known as *tag2tof,* are the same as those for *st2tof* (see section 4.4.1). The simple addition (within the TAGR bank) of this constant *tag2tof* to the values of t_{TTAG} and t_{TPHO}, accounts for this timing convention in the physics analysis of the data.

4.4.3 Time of Flight Calibration

The process of time of flight calibration [71] is essential in determining the subsequent quality of charged particle identification and mass resolution (see section 3.6.5). Moreover, it is at this stage of the overall calibration process where the timings from the start counter, photon tagger and time of flight are aligned relative to each other.

This TOF calibration involves many stages, for which a brief description will be given:

1. Status and pedestals.

2. TDC calibration.

3. Time-walk correction.

4. Left-Right PMT alignment.

5. Energy loss and attenuation length calibration.

6. Effective velocity calibration.

7. Counter to counter delay calibration.

The **status** (whether or not one or both sides are dead) of a scintillator is flagged for subsequent stages of the calibration and the **pedestals** (ADC channel corresponding to zero value) are measured using a pulser trigger.

The **TDC calibration** takes the form of a channel to time (ns) conversion. Special pulser runs are performed from which the response of the TDC to the sent pulse for various start-stop delays is analysed. The resulting TDC channel vs time distribution is fitted with the following function:

$$t = c_0 + c_1 T + c_2 T^2 \tag{4.14}$$

where, c_0, c_1 and c_2 are the determined calibration constants, T is TDC channel number and t is time in ns.

Time-walk corrections as a function of pulse height are determined for each PMT by performing special laser runs. These corrections are necessary due to the height dependent rise time of an analogue pulse.

After completion of the first three stages of TOF calibration, **Left-Right PMT alignment** of each scintillator is required. This alignment and the consequent left-right time offsets allow for the determination of hit position within the scintillator. On a sector-by-sector basis, the hit position from TDC left and TDC right are plotted for each scintillator. This sector based distribution should be symmetric around zero, that is to say the x-projected left and right edges ($edge_L$ and $edge_R$) for each scintillator should be symmetric around zero. Any necessary left-right time offset Δt, is calculated using the following relation:

$$\Delta t = (edge_L + edge_R)/v_{eff} \tag{4.15}$$

where, v_{eff} is the effective velocity in the scintillator material with nominal value $16\,cmns^{-1}$.

The next stage of the process is the calibration of **energy loss**, $\delta E/\delta x$, in the scintillator, and the **attenuation length** of each scintillator. The method used requires already reasonable timing calibrations in order to select pions for the energy loss calibration. Loose timing cuts are applied to select pions and the geometric mean position of the Minimum Ionising Particle (MIP) is measured for each scintillator using the pulse height outputs of the left and right ADCs. These outputs are normalised such that the pulse height of a MIP incident normally at the centre of the scintillator is equivalent to $10\,MeV$. The attenuation length calculation follows by the determination of the relation between the amount of light arriving at each PMT and the position along the scintillator.

The penultimate stage is the calibration of the **effective velocity, v_{eff}.** The position of a hit along the scintillator with respect to the centre, y, can be determined using the timing information from both ends of the scintillator. Moreover,

position y can be determined from tracking information. Therefore, a fit to the difference between the left and right timings (t_L and t_R) versus y, can be used to determine v_{eff} and the position offset, y_{offset}, for each scintillators, using the relation:

$$y = \frac{v_{eff}}{2}(t_L - t_R - y_{offset}) \qquad (4.16)$$

where, t_L and t_R are the adjusted times from the left and right PMTs respectively. This calculated value is then used in the next calibration loop at stage 4.

Finally, the **counter to counter delays** are calibrated. Each of the 288 scintillator counters which make up the time of flight system is required to have their timing aligned with the start counter/photon tagger. Pions are selected by cutting on the energy deposited in the scintillator (as described earlier in this section) and a distribution of vertex time from time of flight minus vertex time from the start counter/photon tagger is studied. The main peak of this timing/delay distribution is fitted, and an offset determined which centres the peak on zero.

4.4.4   Drift Chamber Calibration

Calibration [58,72] of the drift chambers (see section 3.6.3) is necessary in order to obtain accurate reconstruction of a particle's track. This track reconstruction is based upon the measurement of the particle's position within the cells of the drift chambers and is performed in two stages, Hit Based Tracking (HBT) and Time Based Tracking (TBT).

Hit based tracking relies upon a least squares fit of the track to hit wire position and is calculated when at least three out of five superlayers register a hit. The resulting track segments are then linked across all superlayers per region and all three regions to reconstruct the particle track. However, due to the radially increasing diameters of the cells and the possibility of *holes* in the drift chamber, HBT has poor momentum resolution of the order $\sim 3-5\%$ for a $1\,GeV/c$ track. Holes are defined as areas with dead wires in the chamber and result in less than the maximum 34 layers registering track hits.

The second stage, time based tracking, relies upon the measurement of the *drift time*. In this procedure, flight time information of the particle from the target to the time of flight scintillators is used to correct the drift time. A pre-determined table is then used to convert the corrected drift times into drift

distances within the cells. These positions within each cell are fitted in order to determine the track parameters. Drift time, t_{drift}, is defined as:

$$t_{drift} = t_{start} + t_0 - t_{TDC} - t_{flight} - t_{prop} - t_{walk} \qquad (4.17)$$

where, t_{start} is the event start time, t_0 is the fixed time delay for the wire, t_{TDC} is the raw time measured by the TDC, t_{flight} is the particle flight time for the reaction vertex to the wire, t_{prop} is the signal propagation time along the wire, and t_{walk} is a time-walk correction made for short drift times due to differences in ionisations of slow and fast moving particles, i.e. minimum ionising particles produce smaller signals resulting in larger time smearings. It is important to note that t_{start} is defined based upon coincident signals from the photon tagger, start counter and time of flight subsystems, for photon experiments such as G10. TBT improves momentum resolution for a $1\,GeV/c$ particle to the order $\sim 0.5\%$.

4.4.5 Electromagnetic Calorimeters Calibration

The aim of the calibration process [73] for the electromagnetic calorimeters (see section 3.6.6) is to produce agreement between the vertex time of a track as seen by this subsystem and the vertex time of the track as seen by the time of flight. That is to say a distribution of EC vertex time minus TOF vertex time should be centred on zero. It is vital that this EC time be well defined since the discrimination between photons and neutrons is based solely upon the velocity of the particle detected. It should be noted that the energy deposition of a neutron in the calorimeters is not total. The calibration of the large angle electromagnetic calorimeters utilises a similar technique.

4.5 Photon Energy Calibration

During the analysis of the previous pentaquark search experiment at CLAS, known as G2a, it was found that the photon energy as measured by the photon tagger, E_{tagg}, and that which was reconstructed in CLAS were different. Using the reaction $\gamma d \rightarrow p\pi^+\pi^-(n)$, and constraining the neutron mass, the photon energy, E_γ, was calculated [74] and the distribution of the ratio $R = E_\gamma/E_{tagg}$ versus E-counter position was studied. The conclusion drawn from this study and corroborated by simulations [75], was that the frame which supports the E-counter was sagging, resulting in relative energy shifts between the E-counters of $\sim 0.5\%$.

During the G10 experiment, special measurements were conducted to determine this E-counter relative energy shift, independent of CLAS. Consequently, a photon energy correction factor was defined for use in the physics analysis of the data. This new method resulted in a calibration of the photon energy to a resolution of 0.1%.

The tagged photon energy, E_{tagg}, was measured in coincidence with e^+e^- pairs detected in the additionally instrumented pair spectrometer, PS (see section 3.5) at different PS magnetic field settings. The photon energy measured in the pair spectrometer, E_{calc}, is given using the simple relation below:

$$E_{calc} = E_{e^-} + E_{e^+} \qquad (4.18)$$

where, E_{e^-} and E_{e^+} are the energies (momenta) of the electron and positron respectively, as calculated from the reconstructed trajectories of the lepton pair and the PS magnetic field.

During these special runs, the data acquisition was triggered by a coincidence signal between the scintillator counters (in the PS) corresponding to the detection of an electron positron pair. For each triggered event, the information from the pair spectrometer and microstrip detectors, along with photon tagger E and T-counters, was recorded. Automation of this process allowed measurements to be taken at several settings of the PS dipole field, ranging from $-0.36\,T$ to $-1.4\,T$. This range of field values allowed for almost complete coverage of the tagged photon energy spectrum. Figure 4.8 shows the PS magnetic field, B, versus photon energy as measured by the photon tagger. The full range of photon energies in the G10 experiment was covered by these measurements.

At each PS field setting, figure 4.8 shows that there is a defined photon tagger energy range (acceptance) and consequently, E-counter range. Starting at a PS field setting $-0.36\,T$, and stepping up to $-1.4\,T$, the ratio $R = E_{calc}/E_{tagg}$, was calculated for each E-counter in the current acceptance, on an event by event basis.

Consequently, this ratio provides an independent energy calibration of the photon tagger E-counters, and a correction factor which can be applied to the photon energy at the physics analysis stage. Figure 4.9 shows this ratio, $R = E_{calc}/E_{tagg}$, versus E-counter ID from the G10 measurements. Note, the few outlying points around counters 120 and 440 are due to miscabling (this was fixed and accounted for), and counters above 700 had limited statistics and PS resolution.
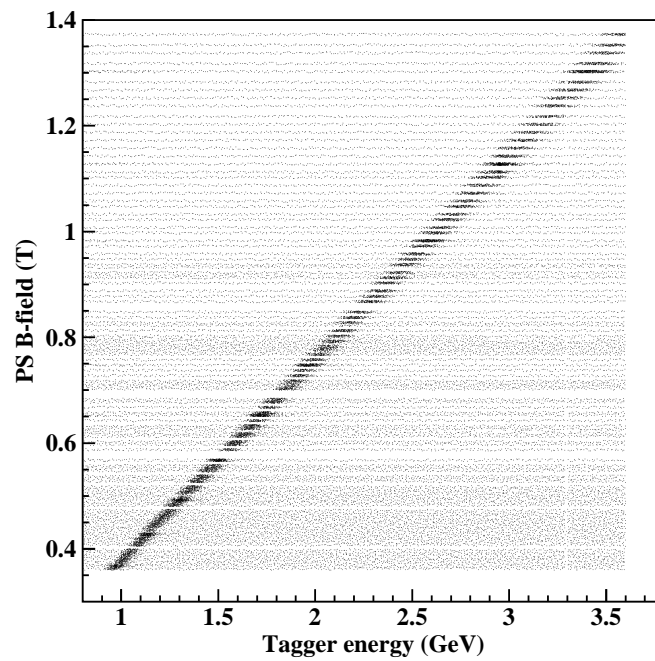
Figure 4.8: PS magnetic field vs tagger photon energy, E_{tagg}.
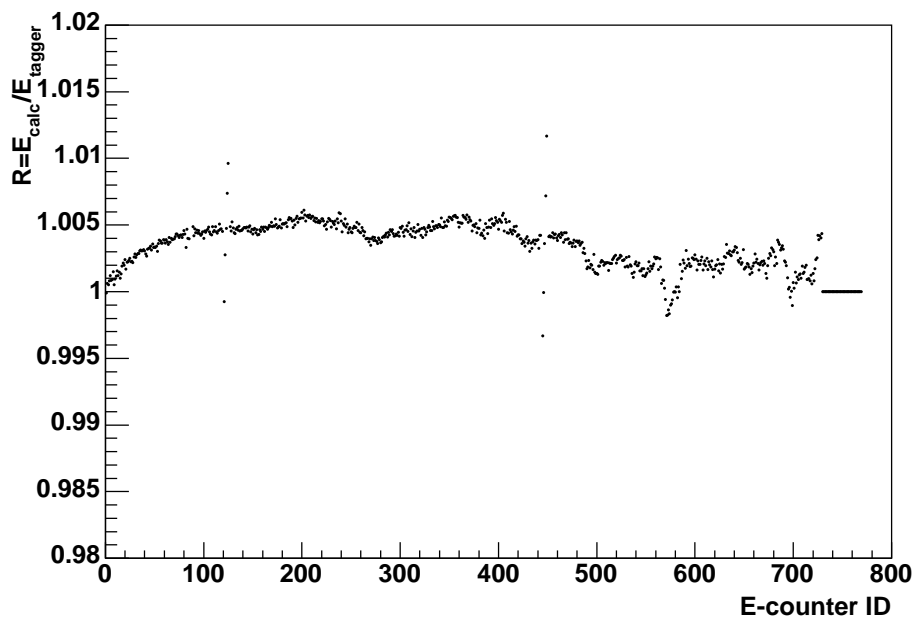
Figure 4.9: G10 Photon Energy Calibration / Correction

Summary

Once the processes described in this chapter are complete, the data are calibrated and in a physical format which can be used for analysis. The information contained within the data is used for initial particle identification and the construction of $4-vectors$. These particle $4-vectors$ allow for the *physics analysis* of events of interest within the data. The initial particle identification and event selection, along with the results of the data analysis, are presented in the following chapter.

Chapter 5

Data Analysis: Event Selection and $M(nK^+)$

This chapter describes the details in the analysis of $\gamma d \to pK^+K^-(n)$: $\Theta^+ \to nK^+$, where the neutron is reconstructed from the appropriate missing $4 - momentum$. The analysis will be presented for the data from both torus current settings ($2250A$ & $3375A$) used in the experiment. The details and steps follow the order of the analysis procedure, and results will be shown for the full range of photon energies. The analysis cuts presented here are considered to be the minimal set and this analysis is one of four independent analyses of the reaction $\gamma d \to pK^+K^-(n)$ for the same data. One should note from the outset that this analysis is not a direct study of the elementary process $\gamma n \to \Theta^+K^-$, since a final state interaction (see figure 5.1) is required in order to detect the proton in the CLAS spectrometer.

5.1   Particle Identification and Event Selection

In the following particle identification and event selection sections (sections 5.1.1 to 5.3), the histograms and cuts shown are from the high field data analysis. However, the steps and procedures are equivalent for both torus current settings.

5.1.1   Hit Multiplicity and TOF Mass Cuts

The reaction $\gamma d \to pK^+K^-n$ is exclusive, therefore, the first step in the initial selection requires the identification of events with four particles in the final state. The neutron detection efficiency of CLAS is low, and the momentum resolution of neutrons is poor. Hence, the three charged particles (p, K^+ and K^-) are measured
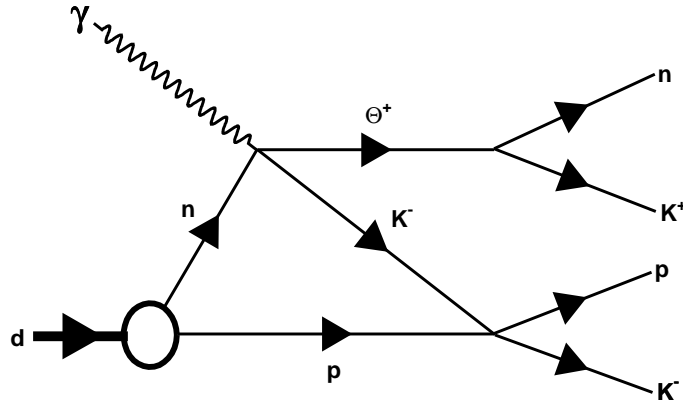
Figure 5.1: A rescattering diagram that could contribute to the production of the Θ^+ and an energetic proton.

in CLAS, and the neutron is reconstructed by missing mass ($\gamma d - pK^+K^-$). The data were skimmed to select events with three charged particles or three charged particles plus one neutral particle in CLAS, along with the additional requirement that at least one hit be registered in the photon tagger. The hit multiplicity of these events is seen on the left of figure 5.2. Further to this selection based on number of particles (hits), mass cuts were implemented to refine the particle identification. These cuts are made on the mass (mass squared) as calculated by the time of flight subsystem (see section 4.4.3), and are dependent upon particle charge. The criteria are as follows:

- charge zero particle, then identified as a neutral (neutron)

- non-zero charged particle, must have a valid drift chamber track, and either a valid time of flight hit or electromagnetic calorimeter hit

- the TOF mass windows selected for initial identification are as follows:

- $0.09 < M^2 < 0.49\,(GeV/c^2)^2$: either K^+ or K^-, dependent on charge

- $0.49 < M^2 < 1.44\,(GeV/c^2)^2$: proton

This hadron identification is preliminary, since there is no clear distinction between kaons and pions at this stage. This issue of mis-identification will be dealt with in a subsequent stage (see section 5.1.4).

The TOF masses for the proton and both kaons can be seen on the right of figure 5.2 (these are the masses after further hadron-photon vertex timing cuts).

When an event contains pK^+K^- or $pK^+K^-neutral$, based on the above criteria, it proceeds to further stages of event selection.
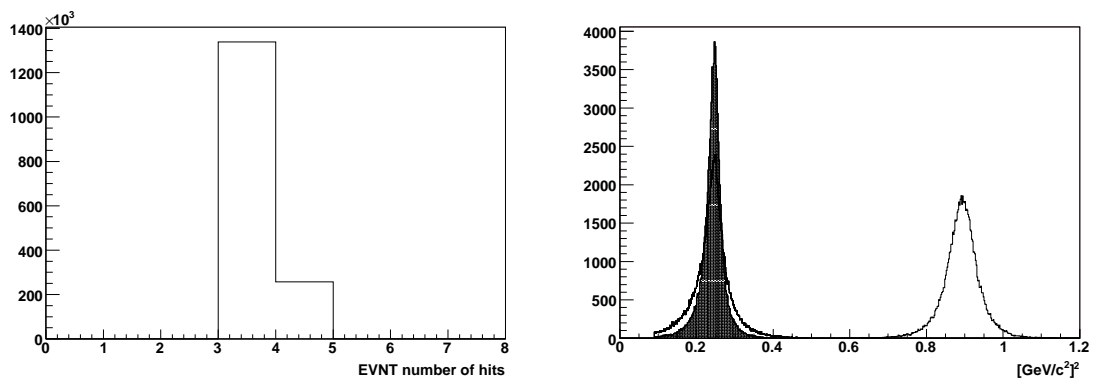
Figure 5.2: Hits multiplicity (left) showing 3 or 4 particles. TOF masses (right) of the proton and both kaons (K^- shaded).

5.1.2   Z-Vertex Cut

The first cut which was applied was on the $z - vertex$ of each of the particles, to be within the target geometry (see figure 5.3). This cut selects particles whose vertex lies between -16 and $-36\,cm$ downstream of CLAS centre (a relatively tight z-vertex cut).
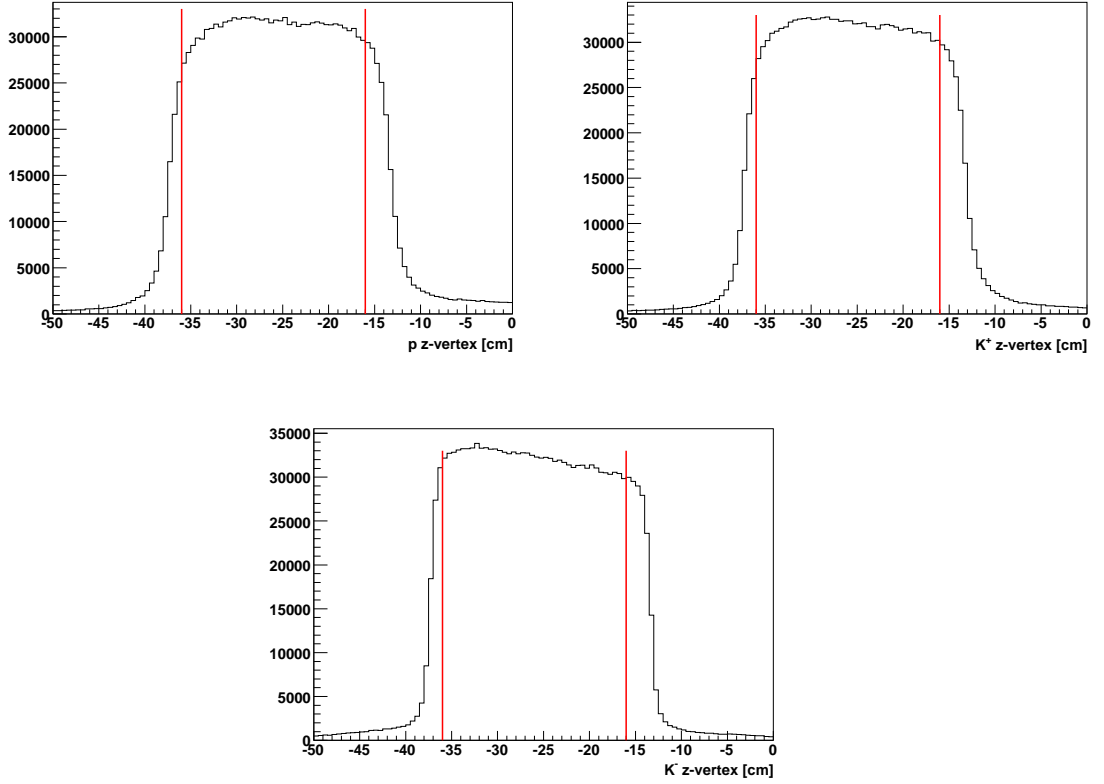
Figure 5.3: z-vertex distributions of the p (top left), K^+ (top right) and K^- (bottom). The red lines represent the boundaries of the cuts.

5.1.3 Photon Selection

The next stage in the event selection process is the identification of the photon corresponding to the event. Where an event has multiple photons (tagger hits) registered in the tagger bank, the actual event photon is identified as the photon whose time is closest to the event vertex time. This procedure involves minimising the difference ($Diff$) between the proton vertex time, and the photon vertex time, using the relations:

$$Diff = (SC^p_{time} - (\frac{SC^p_{path}}{c\beta^p_c}) - (\gamma_{time} + \frac{z^p}{c})) \tag{5.1}$$

and,

$$\beta^p_c = \frac{p_p}{\sqrt{p_p^2 + m^2_{PDG(p)}}} \tag{5.2}$$

where,

SC_{time}^p = proton flight time to the time of flight subsystem

SC_{path}^p = proton path length to the time of flight subsystem

γ_{time} = event photon vertex time

$z^p = z - vertex$ position of the proton (to account for the track offset from CLAS centre)

c = speed of light

p_p = proton momentum

$m_{PDG(p)}$ = mass of the proton from the particle data group

When an event has more than one photon, with the same minimal vertex time difference, it is rejected. This multiple photon condition occurred in less than 1% of the entire data set.

At this point, the tagger energy correction was applied (see section 4.5) to the identified photon. This correction was derived using the pair spectrometer, and accounts for E-counter to E-counter non-linearities in the form of a multiplicative factor to the photon energy E_γ. Further to this tagger energy correction, a run-by-run correction [76], derived from the kinematically complete reaction $\gamma d \rightarrow p\pi^+\pi^- n$, was also applied to the electron beam energy at this stage. This correction again was in the form of a multiplicative factor to E_γ, and accounts for slight run-by-run drifts in the delivered electron beam energy.

5.1.4 Mis-identification of Kaons

At this stage of the analysis the assumption is made that a number of charged particles have been wrongly identified as kaons. In order to remove these events where this mis-identification has occurred, the momentum based on the drift chamber track is retained, but the mass is reallocated to the PDG value of a charged pion or a proton. The $4 - vector$ is subsequently recalculated along with the missing mass of the system, and cuts are applied to remove events where one or more of the charged particles has been mis-identified as a kaon. Explicitly, the $MM^2(pK^+K^-)$ is assumed to be the following permutations, i.e. the 4-vectors are given the mass of either a pion or in one case a proton, and the measured momentum.

Case 1: $MM^2(p\pi^+\pi^-)$

It can be seen, figure 5.4 (top left), that there are events where both kaons are actually mis-identified pions, and these are rejected with the cut $MM^2(p\pi^+\pi^-) < 1.16\,GeV$. These events correspond to the horizontal band, at the mass squared of the missing neutron. Conversely, the missing neutron associated with actual pK^+K^- events can be seen as the vertical band.

Case 2: $MM^2(pK^+\pi^-)$

Figure 5.4 (top right) shows events within which the K^- is actually a mis-identified π^-. These events are rejected by cutting $MM^2(pK^+\pi^-) < 0.96\,GeV$ (this cut is applied to remove any excess of events in that region).

Case 3: $MM^2(pp\pi^-)$

Figure 5.4 (bottom). Since this is an exclusive process, a cut to reject events with $MM^2(pp\pi) \leq 0\,GeV$, is applied.

One should note at this stage, that the validity of these cuts is based upon the fact that the missing neutron cut (see section 5.1.7), is not a *straight* cut, and therefore would not remove the excess of mis-identified events in the region. As will be detailed, this missing neutron cut is made as a function of photon energy.
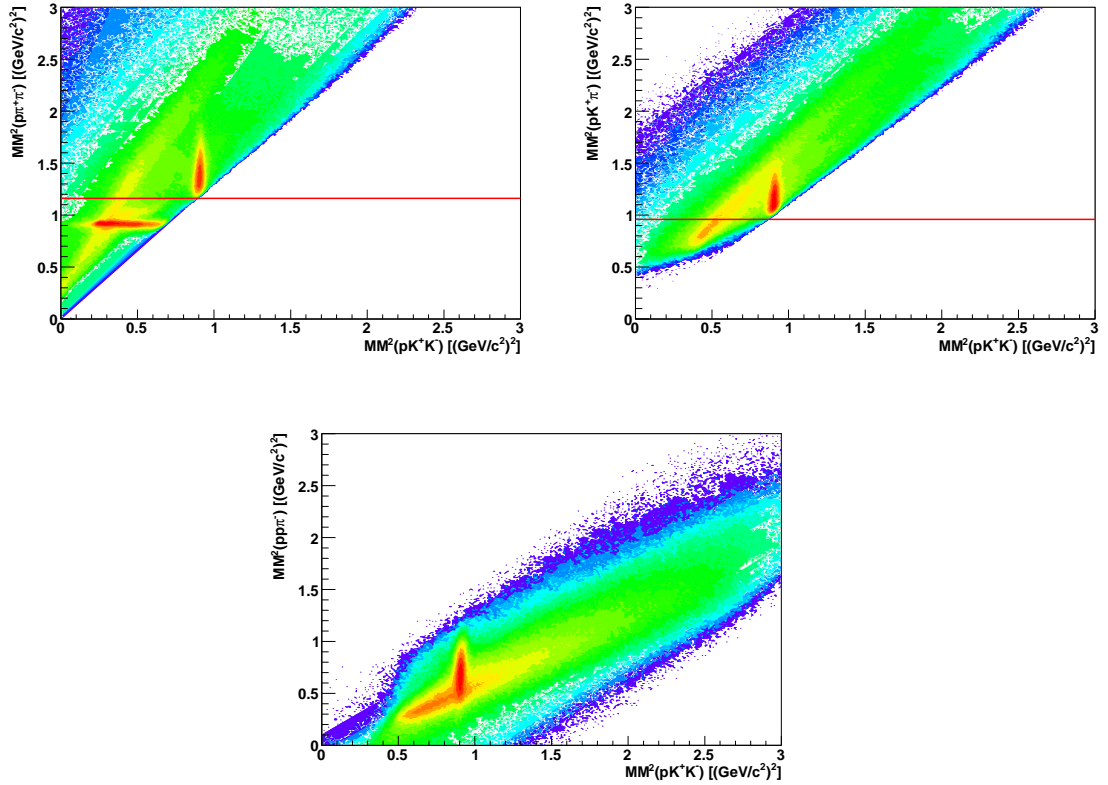
Figure 5.4: case 1: $MM^2(pK^+K^-)$ vs $MM^2(p\pi^+\pi^-)$ (top left), case 2: $MM^2(pK^+K^-)$ vs $MM^2(pK^+\pi^-)$ (top right) and case 3: $MM^2(pK^+K^-)$ vs $MM^2(pp\pi^-)$ (bottom). The red lines represent the applied cuts. High field data.

5.1.5 Hadron - Photon Vertex Timing Cuts

Before the application of vertex timing cuts, a cut of $300\,MeV/c$ minimum momentum is applied to the proton and both kaons. This $300\,MeV/c$ is the minimum detection momentum in CLAS.

In general, if the timing calibrations of the detector subsystems are well defined, the vertex time of the hadron would be the same as that of the photon (their difference would be centred on zero, see top left of figure 5.5). The asymmetric structure also present comes as a result of real protons whose associated photon came from a different beam bucket. This vertex time difference at 2, 4, 6 and 8 ns means that the associated identified photon came from a $(2\,ns)$ beam bucket 1, 2, 3, 4 earlier than the event proton.

Studies of the data, found that the proton-photon vertex time, $t_v^{p\gamma}$, distribution has a dependence upon the momentum of the proton, p_{mom}. Similarly, this dependence is also seen for both the kaon-photon vertex distributions. This de-

pendence was accounted for by the determination and application of momentum dependent $\pm 3\sigma$ cuts. These vertex times were fitted in $100\,MeV/c$ momentum bins. This procedure was developed specifically for this analysis, and became the standard for other G10 analyses.

Figure 5.5 shows the proton-photon vertex timing, its dependence on proton momentum, and the effect of this momentum dependent timing cut (quantitatively, the momentum dependence of the proton timing can be seen in the middle row of figure 5.5). Figure 5.6 shows the effect of the momentum dependent timing cuts derived for the K^+ and K^- respectively. Detailed plots (similar to the proton case) for both kaons can be found in Ref. [77].
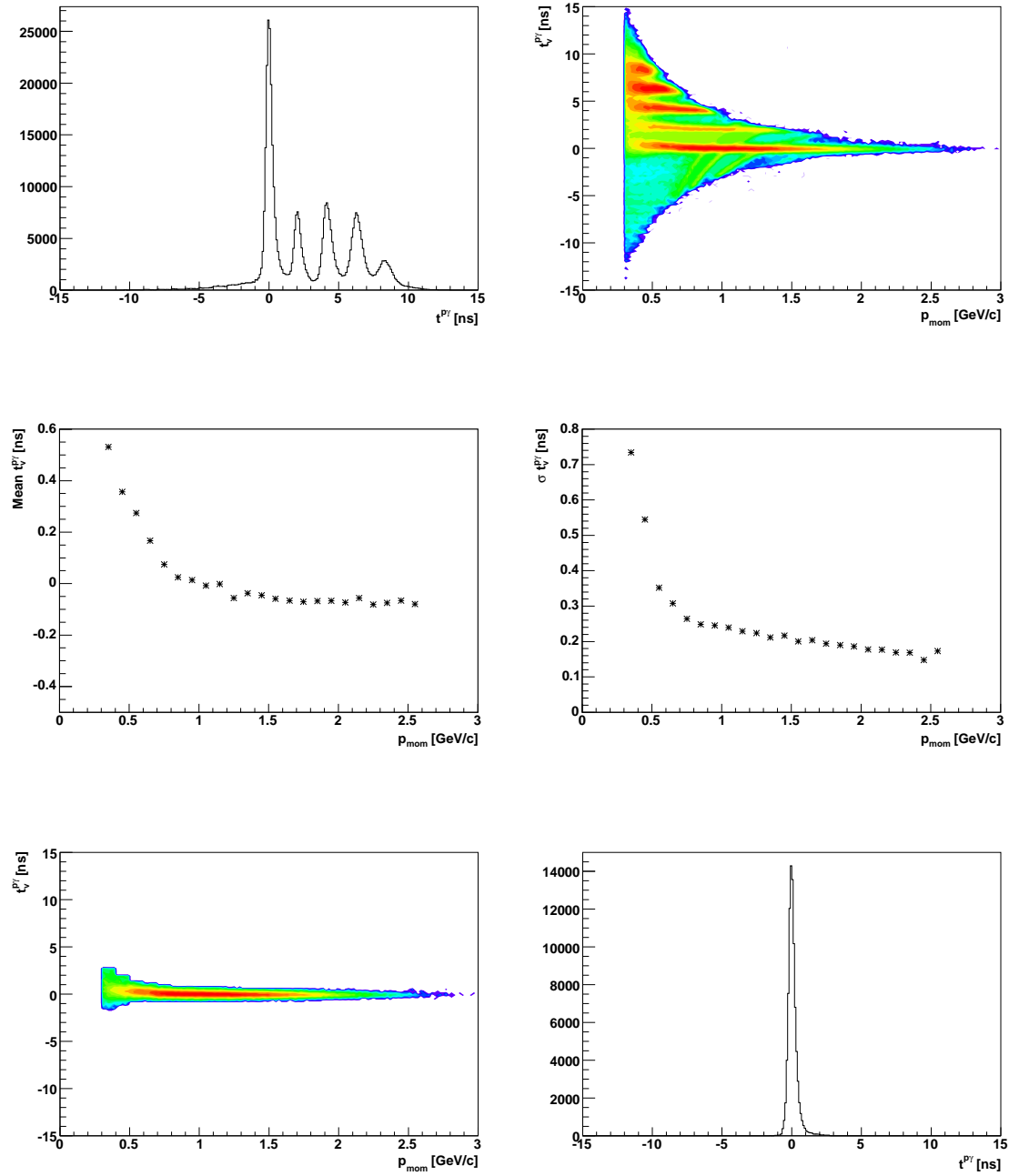
Figure 5.5: $t_v^{p\gamma}$ (top left), $t_v^{p\gamma}$ vs p_{mom} (top right), $t_v^{p\gamma}$ vs p_{mom} after timing cut (bottom left) and $t_v^{p\gamma}$ after timing cut (bottom right). Plots have $0.1\,ns$ bins in timing and $0.02\,GeV/c$ bins in momentum. The middle row shows the quantitative dependence of the mean (middle left) and sigma (middle right).
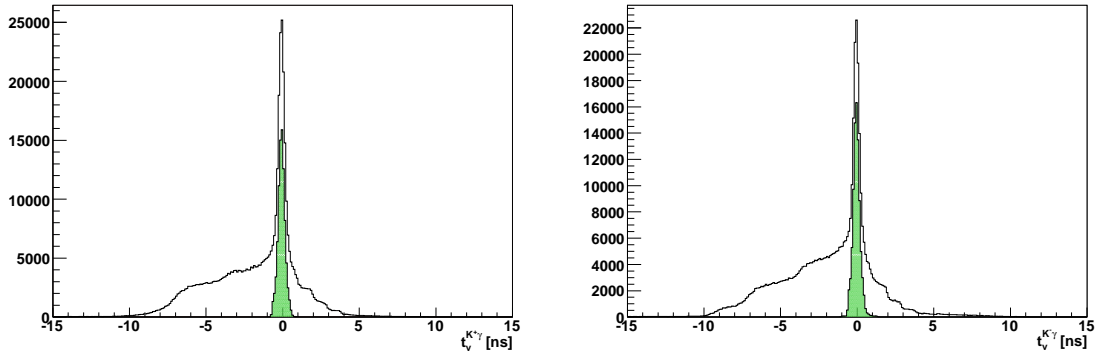
Figure 5.6: $t_v^{K^+\gamma}$ (left) and $t_v^{K^-\gamma}$ (right). The shaded peaks are the vertex timings after the application of the momentum dependent cuts.

5.1.6 Proton - Kaon Vertex Timing Cuts

The final timing cut which was applied, was on the proton-kaon vertex time, t_v^{pK}. A similar study as that for the hadron-photon vertex timing (see section 5.1.5), found that this vertex timing also has a momentum dependence. Again these timing are fitted and cut on $\pm 3\sigma$ for momentum bins of $100\,MeV/c$.

Figure 5.7 shows this dependence and the effect of the timing cut for the K^+, and figure 5.8 similarly for the K^-.
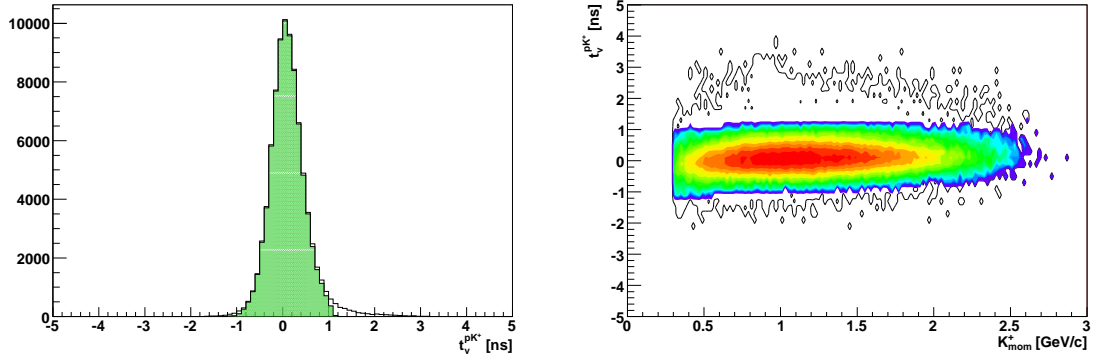
Figure 5.7: Left: $t_v^{pK^+}$ before and after (shaded) the timing cut. Right: $t_v^{pK^+}$ vs K_{mom}^+ before (outline) and after (contour) timing cut.
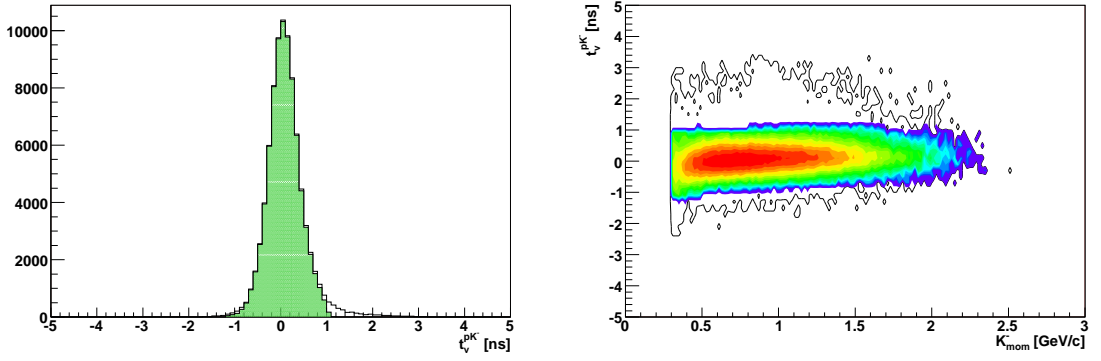
Figure 5.8: Left: $t_v^{pK^-}$ before and after (shaded) the timing cut. Right: $t_v^{pK^-}$ vs K_{mom}^- before (outline) and after (contour) timing cut.

5.1.7 $MM(pK^+K^-)$ / *Neutron Identification*

The neutron is reconstructed using missing mass $MM(pK^+K^-)$. One should note that the reconstruction of the neutron is performed after the application of momentum and energy loss corrections (see section 5.2) to the proton and both kaons. Figure 5.9 (top left) shows the reconstructed neutron for the high field data. The fitted mean of this distribution for high field data is $939.4\,MeV/c^2$ with a sigma of $9.7\,MeV/c^2$, and for the low field data is $938.3\,MeV/c^2$ with a sigma of $11.1\,MeV/c^2$. The momentum of this reconstructed neutron is shown in figure 5.9 (top right) for the high field data. As can be seen in these plots, there is a large contribution in this distribution coming from neutrons with momentum below $200\,MeV/c$. These are neutrons whose momentum arises from the Fermi momentum, and will subsequently be assumed to be spectators for the purposes of this analysis (see section 5.4.2). The estimated background under the neutron peak is $\sim 4\%$ for the high field, and $\sim 5\%$ for the low field.
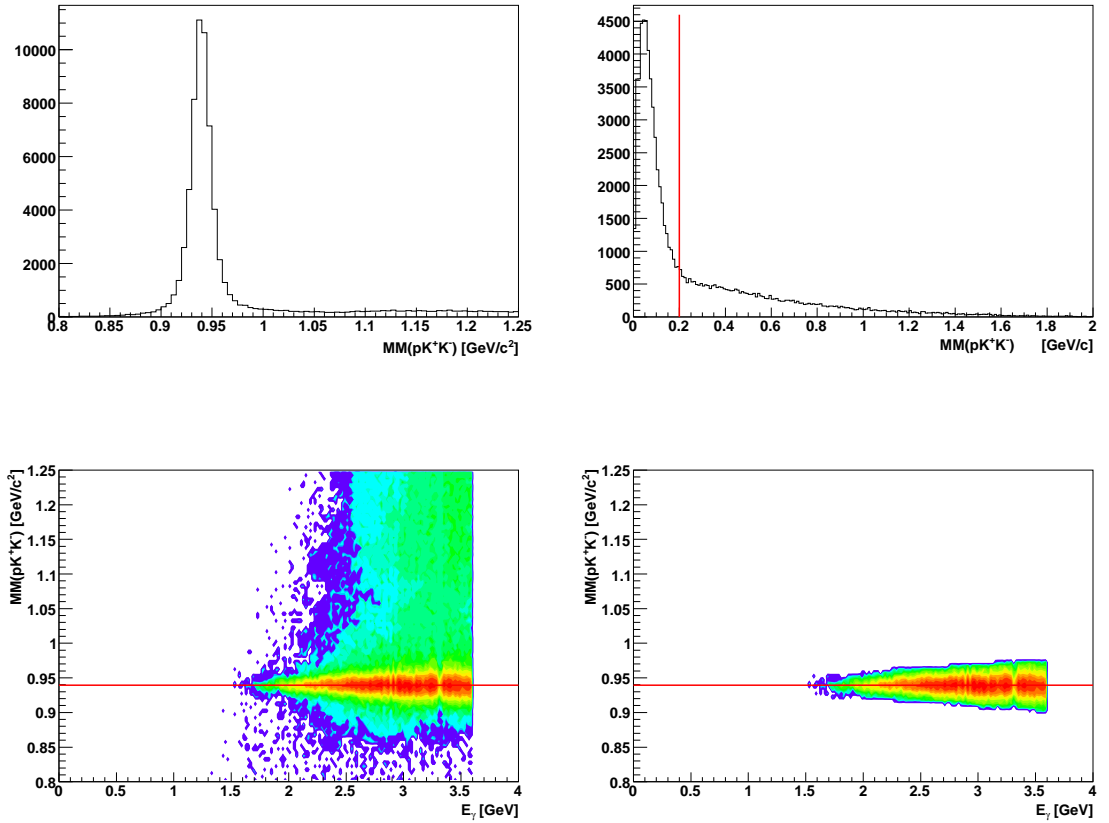
Figure 5.9: Missing mass $MM(pK^+K^-)$ (top left) showing the reconstructed neutron, the momentum distribution of the reconstructed neutron (top right), the mass of the neutron vs photon energy before cuts (bottom left), and after cuts (bottom right).

As can be seen, the neutron mass versus photon energy (figure 5.9), shows a neutron mass and width (sigma) dependence on the photon energy. Quantitatively, this dependence of the mean and sigma of neutron mass can be seen in figure 5.10, for the high field data (although the mean is relatively constant). The width of the neutron peak varies between $\sim 6 - 12\,MeV/c^2$ for the high field data, and $\sim 6 - 15\,MeV/c^2$ for the low field data. Consequently, a photon energy dependent cut on the reconstructed neutron was employed, with the neutron peak fitted, and $\pm 3\,\sigma$ cuts made in $125\,MeV$ E_γ bins. The effect of these energy dependent cuts can be seen in figure 5.9 (bottom right). A straight $\pm 3\,\sigma$ made on the reconstructed neutron would have resulted in a larger background contribution, particularly at photon energies below $2.5\,GeV$, where the width of the neutron reduces to approximately half the width at higher energies.

Once the neutron has been reconstructed and these energy dependent cuts made, the mass is then constrained to be the accepted PDG value. This is done
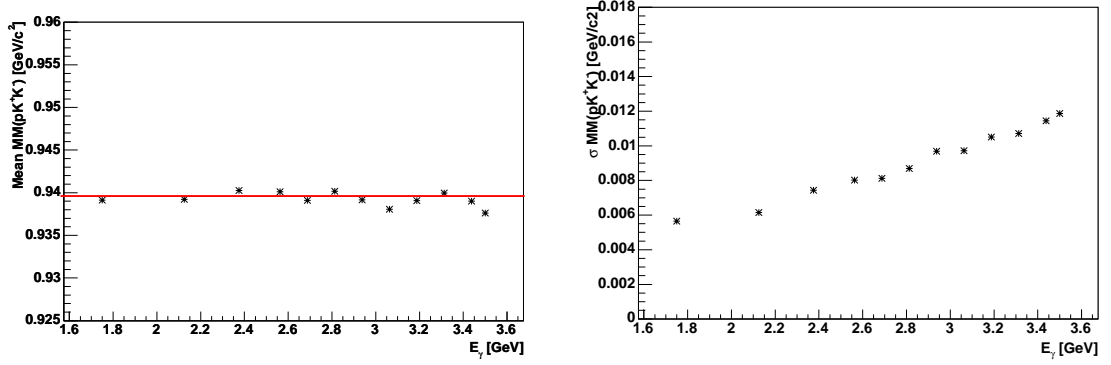
Figure 5.10: The photon energy dependence of the neutron mass mean (left), and sigma (right). The red line represents the PDG neutron mass.

by assigning the mass component of the neutron $4 - vector$ the PDG mass, and retaining the measured $3 - momentum$ component.

At this stage, the proton, both kaons, the neutron and the photon which make up an event in the exclusive reaction $\gamma d \rightarrow pK^+K^-n$ have been identified and selected for further analysis.

5.1.8 Time of Flight Scintillator Counters

Tracks involving any time of flight scintillator counters which are considered to have low occupancy and poorly determined mass calculations (due to poor time resolution or light collection), are removed over and above those removed in the *cooking* process. Those removed are, S1p17, S1p27, S3p23 and S3p41 and all paddles greater than 42, where S is sector and p is paddle number. The mass squared of all particles (M^2) vs paddle number for each sector is shown in figure 5.11. Removal of these scintillator counters improves the overall mass determination and resolution of the detected particles (since the identification and mass determination of particles in CLAS is explicitly related to the timing from the time of flight subsystem).
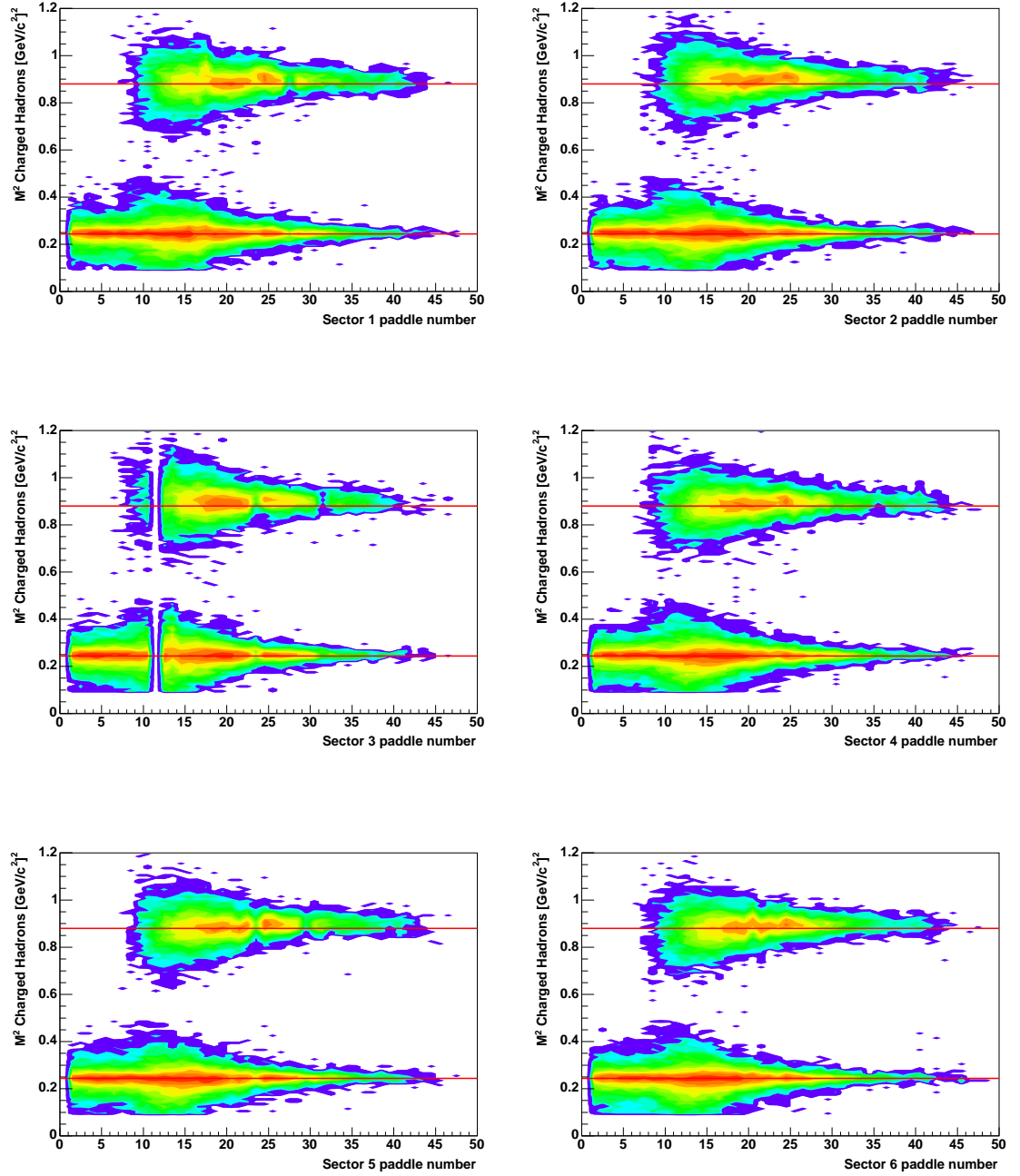
Figure 5.11: Charged Hadron mass (M^2) vs paddle for all 6 sectors. The red lines indicate the M^2 of the proton and charged kaons.

5.2 Corrections

Having identified and selected the detected constituent particles (p, K^+, K^-) of the exclusive events, corrections to the particles measured momenta must be applied. These corrections are described in the following two subsections.

5.2.1 Energy Loss / *ELOSS*

The original momentum of a charged particle at the production vertex will be greater than that which is measured by the drift chambers. This is because a charged particle will deposit energy in the target cell, the target walls, the beam pipe, supporting structures, and the start counter. This energy loss (*ELOSS*) must be determined and the measured momentum corrected. By passing the $4-momentum$ and vertex position of the charged particle, along with the geometry of the target cell, into the ELOSS routine [78, 79], the correction is determined. Top left of figure 5.12 shows the momentum correction distributions for the proton and both kaons.
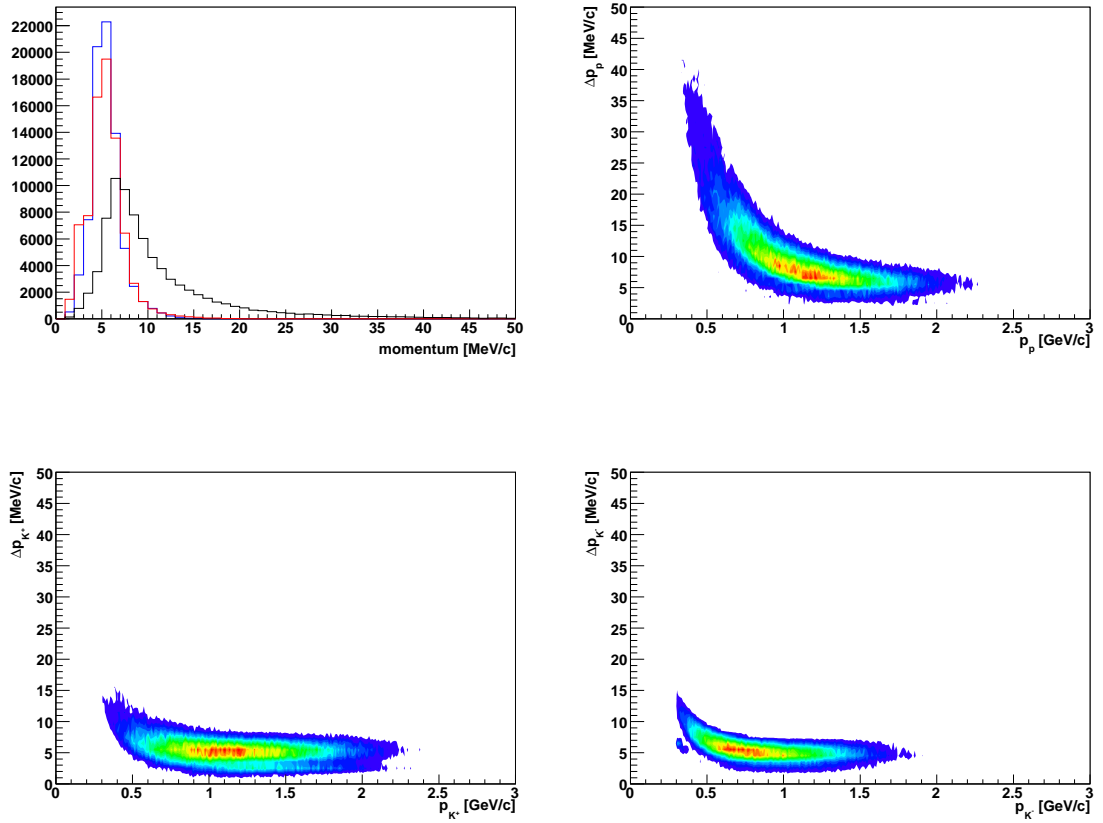
Figure 5.12: Top left: Momentum correction distributions for the proton (black), K^+ (red) and K^- (blue). Top right: Δp versus p for the proton. Bottom left: Δp versus p for the K^+. Bottom right: Δp versus p for the K^-.

A low momentum particle will deposit more energy and therefore require a larger correction. The converse is also true. This can be also be seen in figure 5.12, where the momentum correction, Δp, versus particle momentum, p, is shown for all three particles.

5.2.2   Momentum Corrections

Further to energy loss corrections, another correction to the momenta of the particles is required. These corrections are necessary since CLAS does not measure particle momentum exactly. This discrepancy can be attributed to some or all of the following reasons: the exact mapping and strength of the magnetic field is not known with high precision; the physical position and geometry of CLAS detector components may not agree exactly with the geometrical information in the data reconstruction software; each of the detector subsystems has an inherent resolution.

Three independent routines were developed [80], based upon transverse momentum and $4 - momentum$ conservation in $\gamma d \rightarrow pp\pi^-$, and K_s^0 mass in the $\pi^+ + \pi^-$ decay mode. These corrections assume that the variation in measured momentum and energy of detected particles will be a sector dependent function of momentum and angle $(p, cos\theta, \phi)$.

5.3   Fiducial Cuts

Fiducial cuts are used in order to exclude events which have a particle detected in a region of non-uniform acceptance in CLAS. Non-uniform acceptance is found in the edge regions of the drift chamber sectors, and in regions where particles may interact with the torus magnet coils. The cuts employed here are defined to be the same for all sectors of CLAS, and depend on particle momentum, angle (polar θ and azimuthal ϕ) and charge. These cuts when applied are done so after the application of all corrections, and the fiducial volume (which is symmetric about the sector mid-plane) is defined as follows, for positively charged hadrons:

$$\theta_{min}(deg) = 8 + 25(1 - \frac{p_h}{5})^{24}, \quad \theta_{max}(deg) = 120 \tag{5.3}$$

$$\Delta\phi(deg) = 26sin(\theta_{K^+} - 9)^{0.1p_h^{0.25}} \tag{5.4}$$

and for negatively charged hadrons:

$$\theta_{min}(deg) = 10 + 25(1 - \frac{p_h}{5})^{24}, \quad \theta_{max}(deg) = 120 \tag{5.5}$$

$$\Delta\phi(deg) = 26 \tag{5.6}$$

where, p_h is the momentum of the hadron.

Figure 5.13 shows the hit occupancy (ϕ vs θ angle) of the 6 drift chamber sectors, for positive and negative hadrons, and the effect of the fiducial cuts on one sampled sector (sector 4) for positive and negative hadrons.
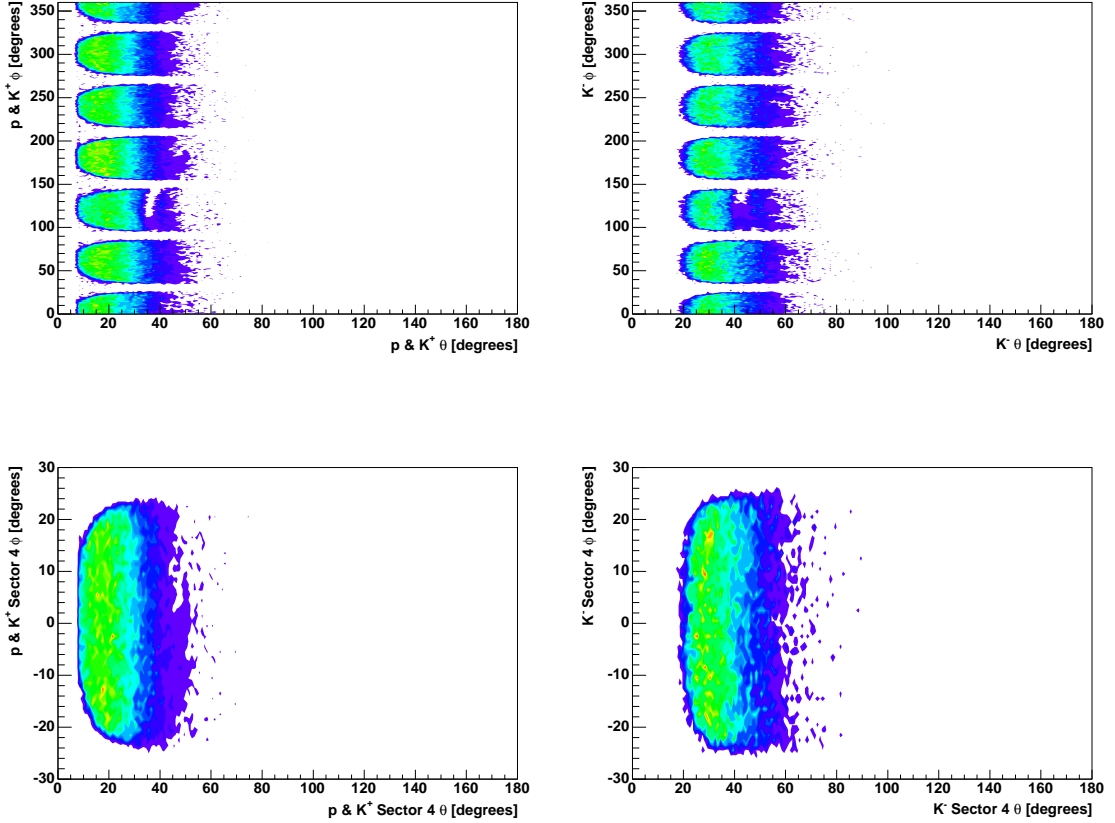
Figure 5.13: ϕ vs θ for p and K^+ before fiducial cuts, all sectors shown (top left), ϕ vs θ for K^- before fiducial cuts, all sectors shown (top right), ϕ vs θ for p and K^+ after fiducial cuts, one sector (bottom left) and ϕ vs θ for K^- after fiducial cuts, one sector (bottom right)

Studies of these fiducial cuts showed that their application only serves to reduce the number of events (and does not change the signal to noise ratio in any of the spectra studied), leaving the shape of any distribution unchanged. For this reason, the analysis presented does not have these fiducial cuts applied.

5.4 Physics Analysis of $\gamma d \rightarrow pK^+K^-n$

Having identified and selected the exclusive events $\gamma d \rightarrow pK^+K^-n$, the physics analysis involves calculating the invariant mass of the nK^+ system to determine whether a signal corresponding to a Θ^+ is present ($\Theta^+ \rightarrow nK^+$). One should

recall the previous reported CLAS signal in photoproduction from the deuteron (see figure 5.14).
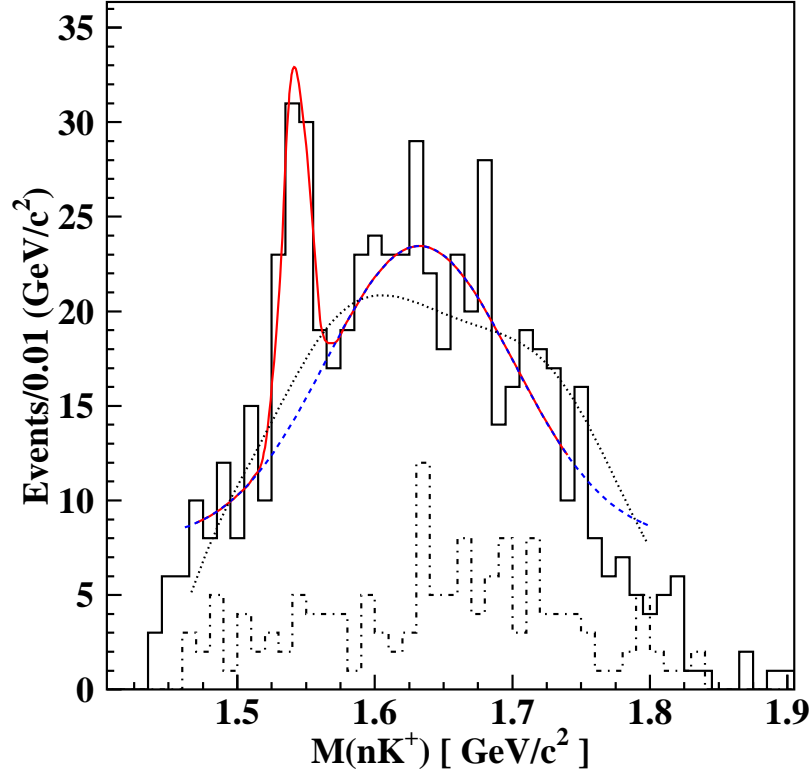
Figure 5.14: Previous reported Θ^+ signal in the reaction $\gamma d \to pK^+K^-n$, with $\Theta^+ \to nK^+$.

Two further stages are required in this analysis before the invariant mass $M(nK^+)$ can be calculated. The first of these requires removing the mesonic and hyperon contributions ($\phi(1020)\,and\,\Lambda(1520)$) from the reaction $\gamma d \to pK^+K^-n$, and the second involves cutting on the neutron and kaon momenta. The production of the $\phi(1020)$, via the process $\gamma d \to p\phi n$, excludes the possible production of the Θ^+. Events with production of the $\Lambda(1520)$, although not incompatible with Θ^+ production, are removed since the invariant mass $M(pK^-)$ contributes to the background under any possible Θ^+ signal. Higher mass Λ^*'s pose a difficulty for removal (as will be discussed in section 5.4.1).

The second stage in the physics analysis is a momentum cut. In particular the neutron momentum is restricted to remove low momentum (Fermi) neutrons. As will be seen (section 5.4.2), a cut can also be placed on the upper momentum of the K^+. This cut reduces the high mass contribution in the invariant mass spectrum $M(nK^+)$, and was employed in the previous published CLAS result (it will be shown in this analysis for comparison).

The details of the analysis is presented for the full photon energy range E_γ $(1.5 - 3.6\,GeV)$, and in subsequent sections summary plots are shown which represent the analysis in smaller (restricted) photon energy ranges.

5.4.1 $\phi(1020)$ Meson and $\Lambda(1520)$ Contributions

The first step in the analysis is the removal of the $\phi(1020)$ (which decays $\phi \rightarrow K^+K^-$) and the $\Lambda(1520)$ (which decays $\Lambda \rightarrow pK^-$). Figure 5.15 shows the kinematical overlap of both the $\phi(1020)$ (left) and the $\Lambda(1520)$ (right) into the region of interest $1.5 - 1.6\,GeV/c^2$ in the invariant mass $M(nK^+)$. This is shown for the high field data.
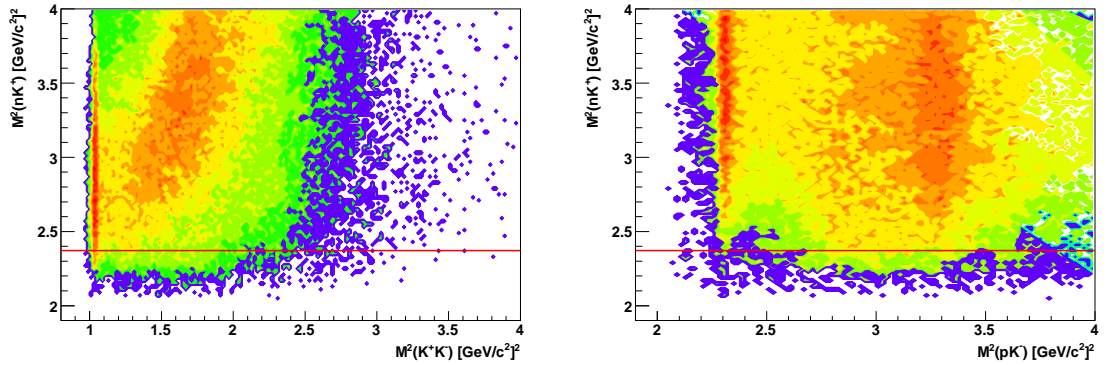
Figure 5.15: $M^2(nK^+)$ vs $M^2(K^+K^-)$ (left), and $M^2(nK^+)$ vs $M^2(pK^-)$ (right). The red line represents the mass squared of a possible $\Theta^+(1540)$. High field.

The invariant mass $M(K^+K^-)$ showing the ϕ, and the invariant mass $M(pK^-)$ showing the Λ, can be seen in figure 5.16, for the high (top) and low (bottom) fields respectively.
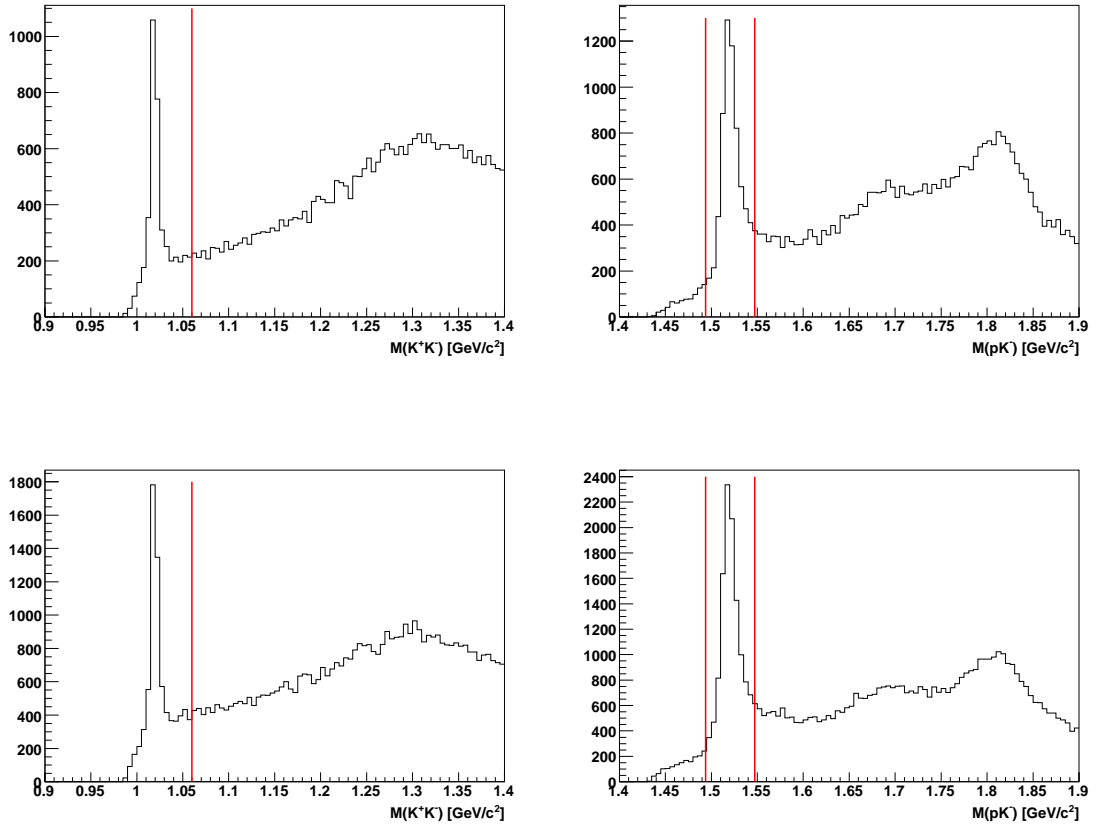
Figure 5.16: $M(K^+K^-)$ showing the $\phi(1020)$ (left), and $M(pK^-)$ showing the $\Lambda(1520)$ and other higher mass $\Lambda^{*'}s$ (right). The red lines are indicative of the cuts employed. High field (top row) and low field (bottom row).

The fitted mean and sigma for the phi peak in the high field data are, $1019.6\,MeV/c^2$ and $7.1\,MeV/c^2$, and in the low field data are, $1019.5\,MeV/c^2$ and $5.9\,MeV/c^2$. For the lambda peak in the high field data, the fitted mean is $1520.2\,MeV/c^2$, and the sigma is $9.2\,MeV/c^2$, and for the low field data, the fitted mean is $1519.8\,MeV/c^2$ and the sigma is $10.1\,MeV/c^2$.

For this analysis, the invariant mass, $M(K^+K^-)$, is required to be greater than $1.06 GeV/c^2$ to cut the ϕ. The removal of these $\phi(1020)$ events is necessary since ϕ production in this channel ($\gamma d \to pK^+K^-n$) excludes production of the Θ^+. A straight cut is made at $1.06\,GeV/c^2$ rather than a $\pm 3\,\sigma$, since studies of the data have shown that these events below $1.06\,GeV/c^2$ have little kinematical overlap into the region of interest (see figure 5.15).

The next cut made is that which removes the Λ background. A $\pm 3\,\sigma$ cut is made in this instance to remove the $\Lambda(1520)$, since Λ production does not exclude possible Θ^+ production (the production of both would still conserve strangeness), and events around $1.55\,GeV/c^2$ in the invariant mass $M(pK^-)$ may provide a

contribution to the $M(nK^+)$ background. The other higher state Λ^*'s are not removed in this analysis. Although these higher mass states do have a kinematical overlap into the region of interest, the number of these states, and their widths, exclude the possibility of employing a cut without an accurate model. Furthermore, a narrow Θ^+ pentaquark peak, with a sufficiently high cross-section, would still be seen on top of the background produced by these Λ^*'s.

5.4.2   Momentum Cuts

The final cuts which were made in this analysis were on the momentum of the neutron and the kaons. The p, K^+ and K^- are each required to have momentum greater than $300\,MeV/c$, and these cuts were applied before the vertex timing cuts as has already been shown (see section 5.1.5). This requirement is based on the detection threshold of CLAS. The neutron momentum cut is made to reject spectator neutrons, whose momentum is less than $200\,MeV/c$, at the end of the low momentum peak. Figure 5.17 shows the momentum distributions for the high and low field respectively. The relation of neutron momentum to invariant mass $M(nK^+)$ is shown in the left column plots of figure 5.18, for the high and low fields respectively.
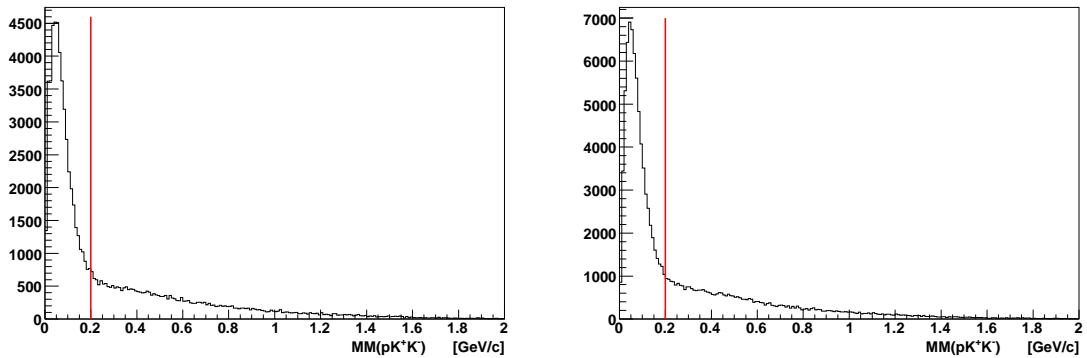
Figure 5.17: The neutron momentum distributions (right: high field, left: low field). The red line represents the cut at $200\,MeV/c$ which removes the spectator (Fermi momentum) neutrons.

Another cut studied was that the K^+ momentum is also required to be less than $1.0\,GeV/c$. The analyses with the application of this cut $P_{K^+}^{max} < 1\,GeV/c$ will be shown for comparison. In the previous CLAS G2a analysis, this cut (motivated by Monte Carlo studies) was employed to reduce the higher mass range of the $M(nK^+)$ spectrum, since it has minimal impact on the region of

interest $M(nK^+)$ < $1.6\,GeV/c^2$, as can be seen in the right column of figure 5.18, for the high and low fields respectively. However, if one assumes that Θ^+ production is *t-channel* dominated (produced via *t-channel* kaon exchange as is the case for the $\Lambda(1520)$), then one would not want to remove the upper end of the P_{K^+} range.
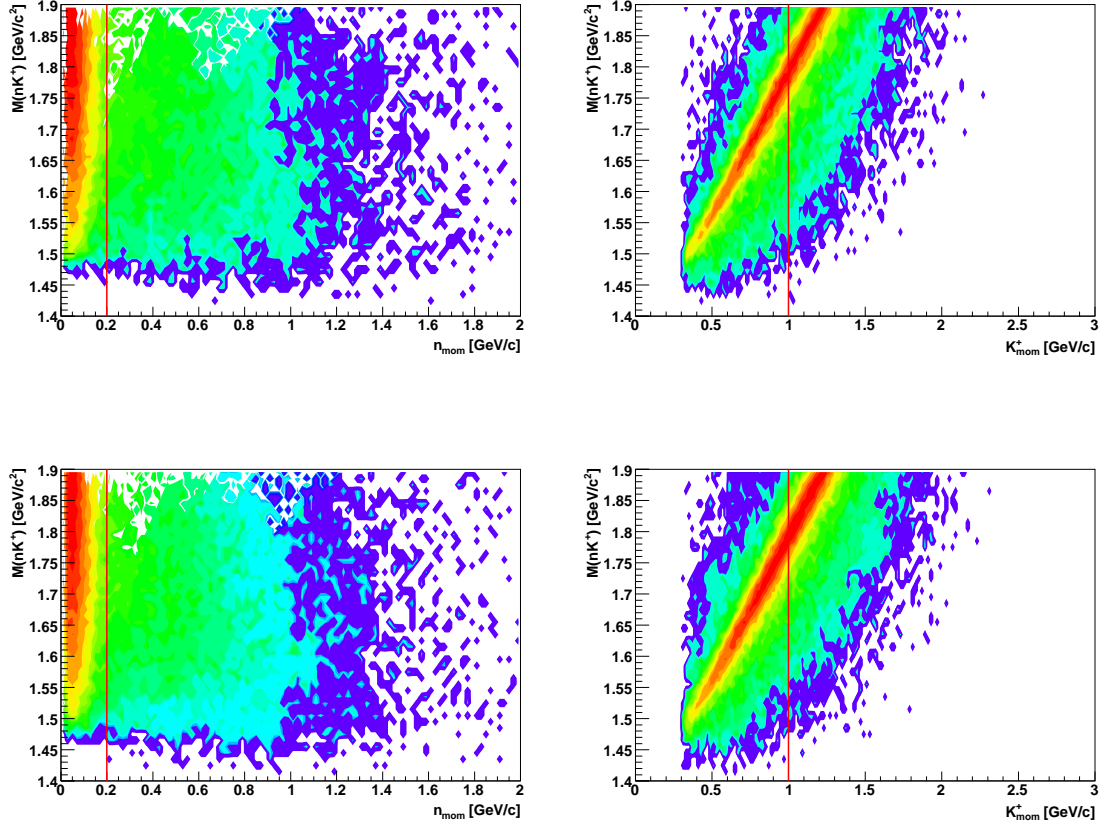
Figure 5.18: $M(nK^+)$ vs n_p (left) and $M(nK^+)$ vs p_{K^+} (right). The red lines indicate applicable cuts. High field (top row) and low field (bottom row).

5.5   Summary of Event and Analysis Cuts

Table 5.1 shows the cuts applied (in order) in this analysis of the G10 data.

Applied Cut	Cut Details
Raw Events Skimmed BOS	3 charged particles or 3 charged plus 1 neutral
z-vertex cut	$-16 \to -36\,cm$
$MM^2(p\pi^+\pi^-)$ mis-ID	$< 1.16\,(GeV/c^2)^2$
$MM^2(pK^+\pi^-)$ mis-ID	$< 0.96\,(GeV/c^2)^2$
$MM^2(pp\pi^-)$ mis-ID	$\leq 0\,(GeV/c^2)^2$
P_p cut	$> 300\,MeV/c$
P_K cut	$> 300\,MeV/c$
photon-proton vertex time	$3 - sigma$ momentum dependent
photon-kplus vertex time	$3 - sigma$ momentum dependent
photon-kminus vertex time	$3 - sigma$ momentum dependent
proton-kplus vertex time	$3 - sigma$ momentum dependent
proton-kminus vertex time	$3 - sigma$ momentum dependent
Bad SC cut	see text for list
E_γ	No cut for nominal analysis
$MM(pK^+K^-)$ cut	$3 - sigma\ E_\gamma$ dependent
$M(K^+K^-)$ cut	$3 - sigma$
$M(pK^-)$ cut	$3 - sigma$
P_n cut	$> 200\,MeV/c$
$P_{K^+}^{max}$ cut (when applicable)	$< 1.0\,GeV/c$

Table 5.1: Analysis Cuts.

5.6   Search for the Θ^+ in the reaction $\gamma d \to pK^+K^-n$

After the analysis detailed previously in this chapter, the invariant mass $M(nK^+)$, and missing mass $MM(pK^-)$, are inspected for evidence of the Θ^+ state. Figures 5.19 and 5.20 show the invariant mass $M(nK^+)$ (with and without the K^+ momentum cut at $1\,GeV/c$). The top plot of each figure represent the results of this analysis.

The conventions for invariant mass $M(nK^+)$ and missing mass $MM(pK^-)$ applied here are as follows:

- $MM(pK^-)$ has allocated PDG masses for d, p, K^+ and K^-. When calculated without a constraint on the neutron mass, $MM(pK^-) = (\gamma d - pK^-) \equiv$ *invariant mass* $M(nK^+)$

- This analysis requires an explicit constraint on the neutron mass (once reconstructed). This constraint improves the mass resolution of the calculated invariant mass $M(nK^+)$.

- Consequently, $M(nK^+)$ has allocated PDG masses for d, p, K^+ K^- and n.

The difference between the invariant mass and missing mass distributions is a result of this explicit constraint on the neutron mass.
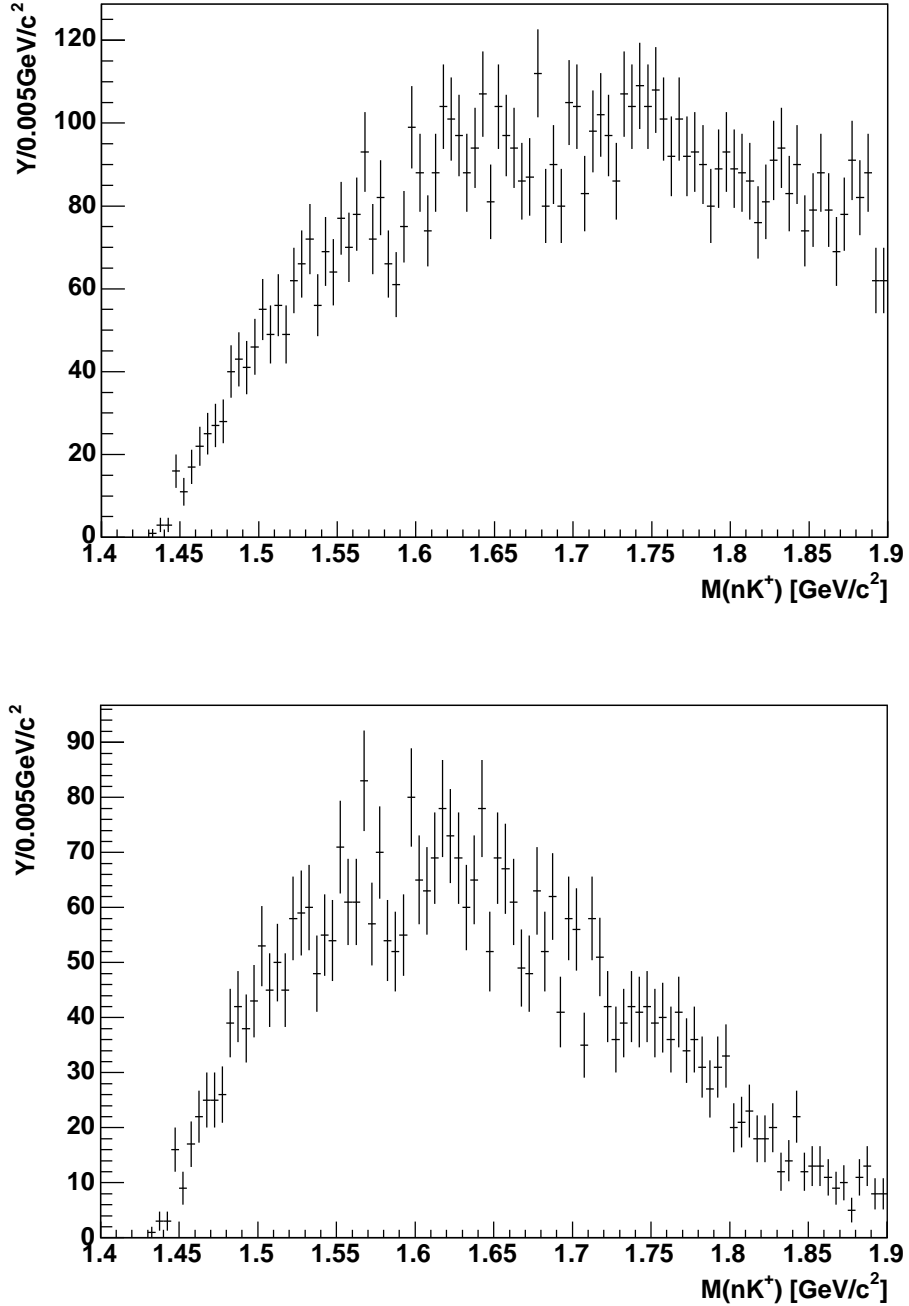
Figure 5.19: $M(nK^+)$ analysis result (top), and $M(nK^+)$ with $P_{K^+}^{max} < 1\,GeV/c$ cut (bottom). High field.
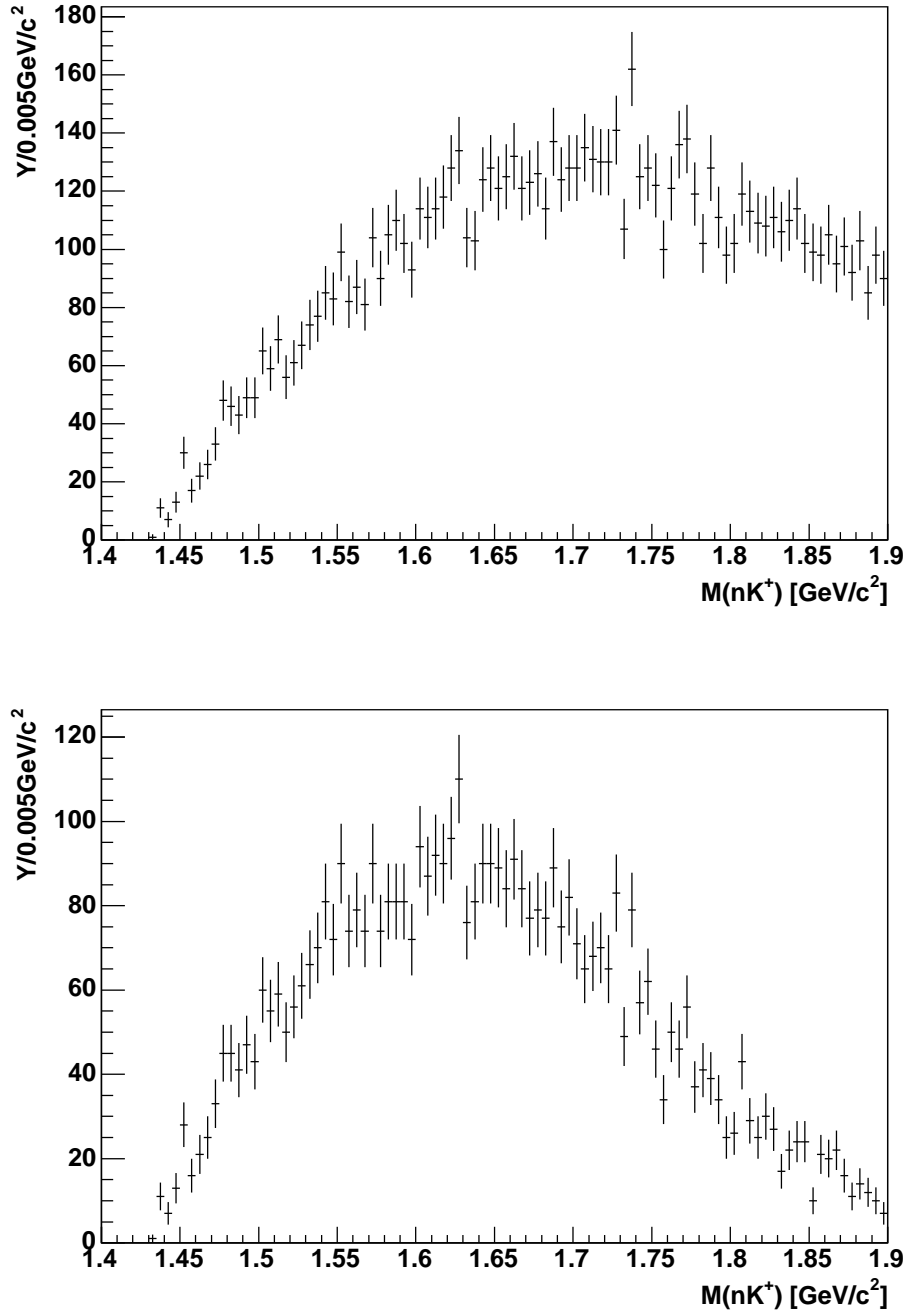
Figure 5.20: $M(nK^+)$ analysis result (top), and $M(nK^+)$ with $P_{K^+}^{max} < 1\,GeV/c$ cut (bottom). Low field.

As can be seen, no evidence of a narrow peak near $1.54\,GeV/c^2$, corresponding to the Θ^+ decaying into nK^+, is observed in this analysis of $\gamma d \rightarrow pK^+K^-n$.

Missing Mass $MM(pK^-)$

Figure 5.21 shows missing mass $MM(pK^-)$ spectra from this analysis, and one should note that the K^+ momentum cut applied. These are shown since they can be compared to the previous published result [2], and $10\,MeV/c^2$ bins are used based on previous missing mass resolution studies [81].
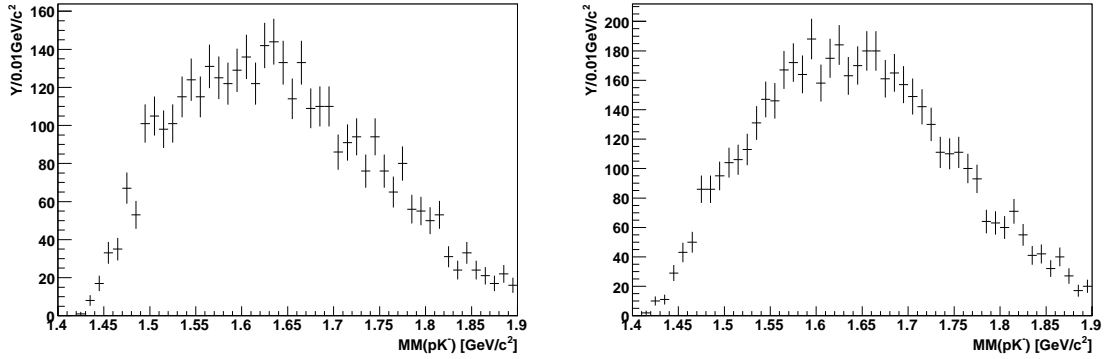
Figure 5.21: $MM(pK^-)$ with $P_{K^+}^{max} < 1\,GeV/c$ cut. High field (left) and Low field (right).

5.7   Effect of Photon Energy Cuts

In order to study the effect of any photon energy dependence on $M(nK^+)$, the equivalent analysis has also been performed for restricted E_γ ranges. The following section shows the results of analyses of $\gamma d \rightarrow pK^+K^-(n)$ carried out with the following cuts made on the photon energy $E_\gamma < 2.35\,GeV$, $E_\gamma < 2.4\,GeV$ and $E_\gamma < 2.7\,GeV$. These analyses proceed exactly as detailed previously and were conducted in order to be compared with the results of the other independent analyses of this reaction channel [82–85]. In each of these analyses, the invariant mass $M(nK^+)$ and missing mass $MM(pK^-)$, with the K^+ momentum cut $(P_{K^+}^{max} < 1\,GeV/c)$, are shown. The bin width of $10\,MeV/c^2$ is used for a qualitative comparison to the previous published analysis [2].

Cutting on the photon energy restricts the phase-space available for the production of higher state Λ^*'s. Again, no significant signal corresponding to the Θ^+ is seen in any of these spectra.

$E_\gamma < 2.35\,GeV$

Figure 5.22 shows the invariant mass and missing mass for the final state, for the high and low fields respectively.
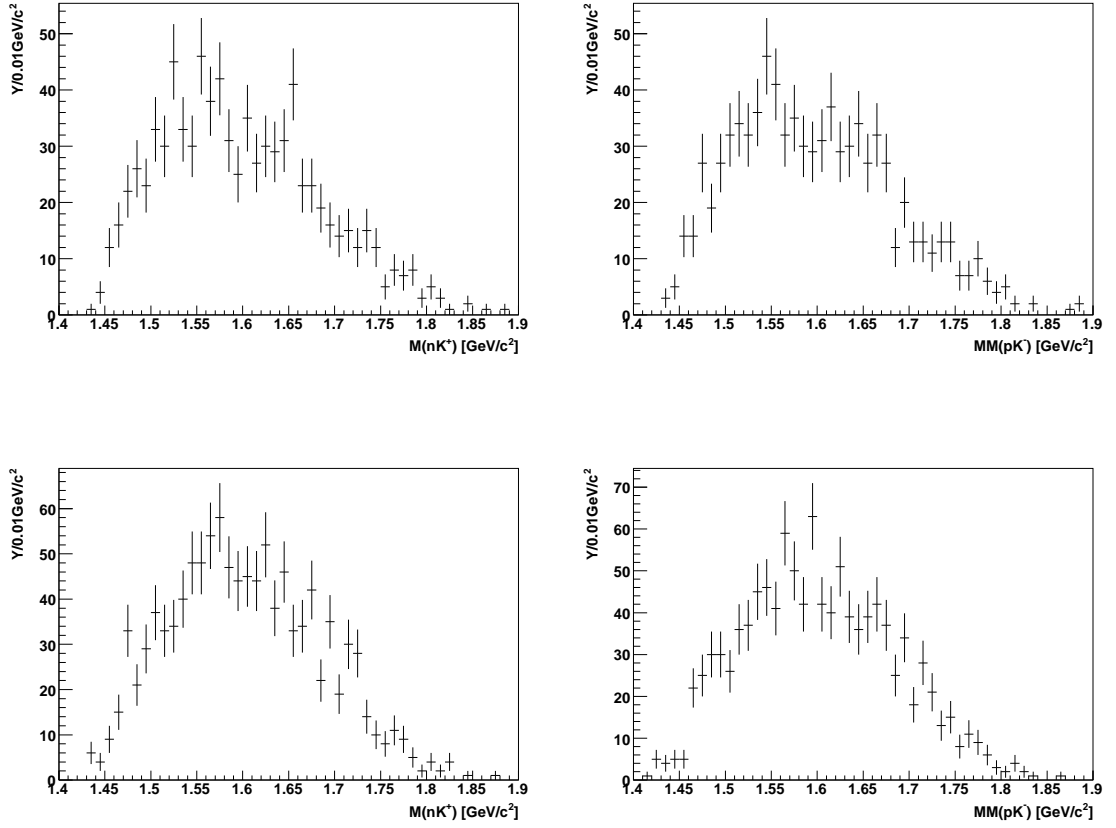
Figure 5.22: $M(nK^+)$ (left) and $MM(pK^-)$ (right), for the high (top) and low (bottom) field data .$[0.01GeV/c^2]$.

$E_\gamma < 2.4\,GeV$

Figure 5.23 shows the invariant mass and missing mass for the final state, for the high and low fields respectively.
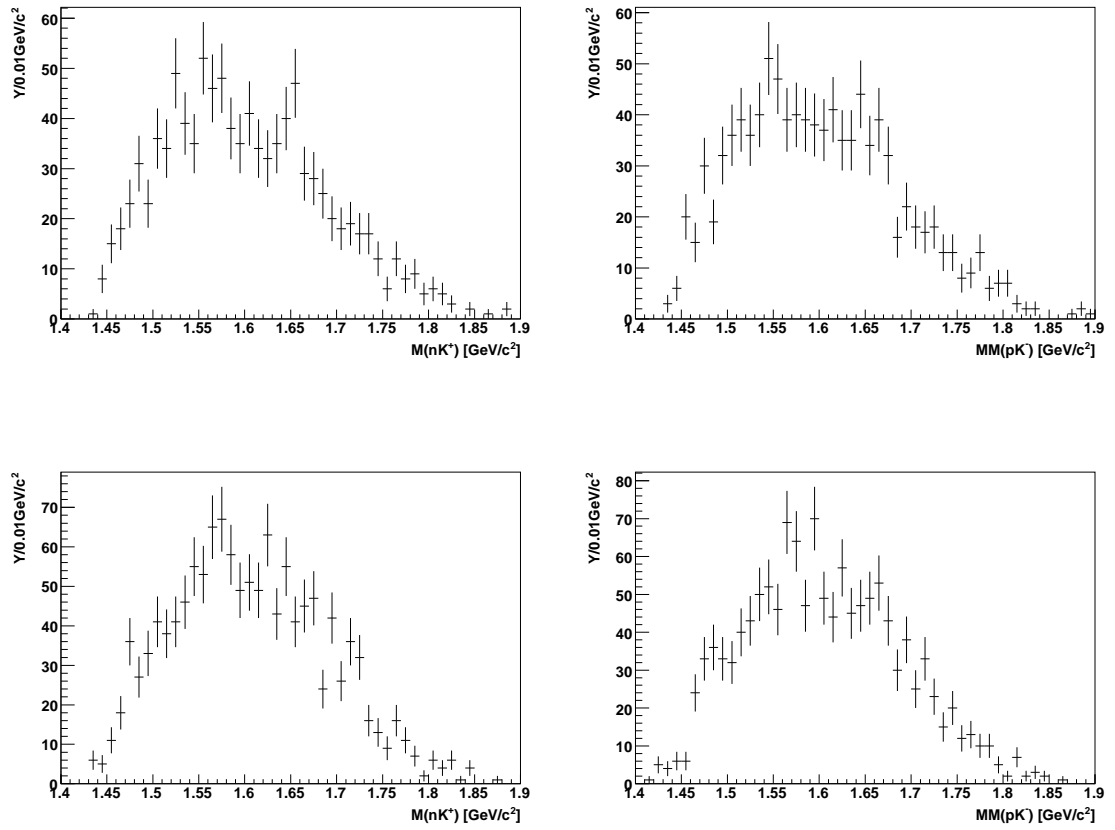
Figure 5.23: $M(nK^+)$ (left) and $MM(pK^-)$ (right), for the high (top) and low (bottom) field data $[0.01 GeV/c^2]$.

$E_\gamma < 2.7\, GeV$

Figure 5.24 shows the invariant mass and missing mass for the final state, for the high and low fields respectively.
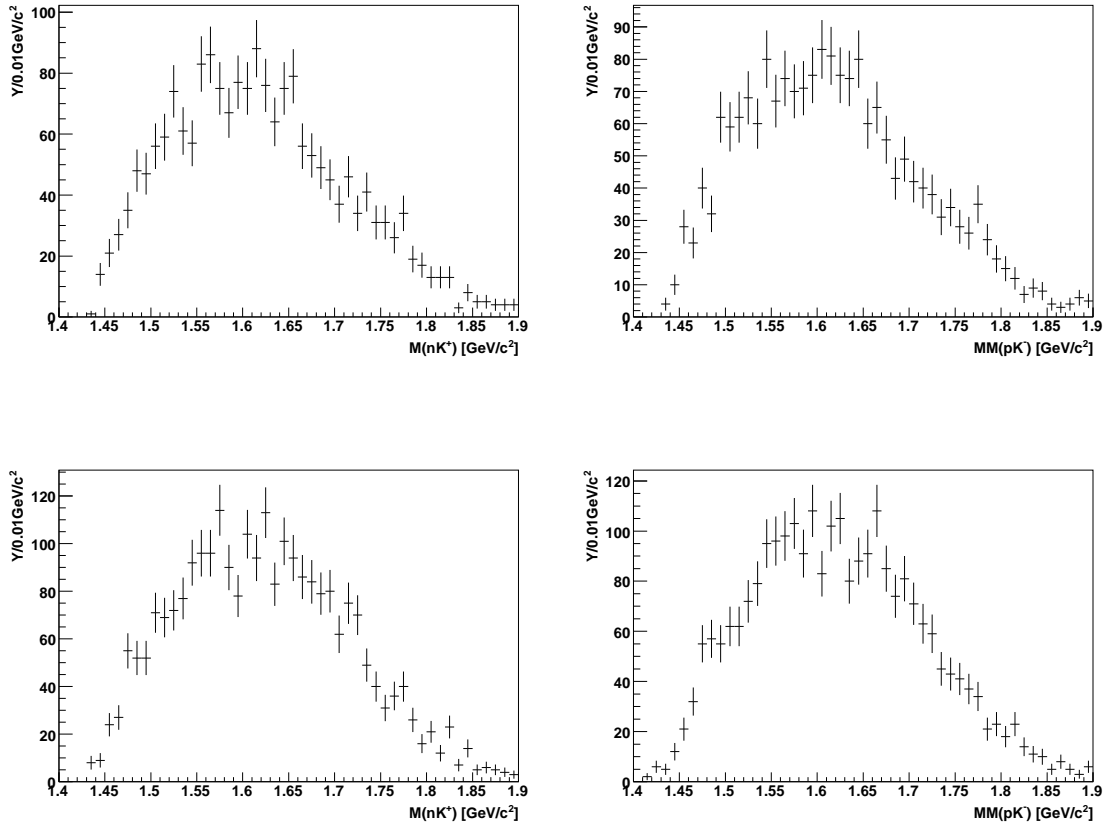
Figure 5.24: $M(nK^+)$ (left) and $MM(pK^-)$ (right), for the high (top) and low (bottom) field data $[0.01 \, GeV/c^2]$.

Summary

As has been presented in this chapter, the result of this analysis of $\gamma d \rightarrow pK^+K^-n$ shows no evidence of a narrow peak near $1.54 \, GeV/c^2$, corresponding to the Θ^+ decaying into nK^+. Consequently, further to the reporting of a null result, it is necessary to provide a quantitative statement. This statement takes the form of a production cross-section upper limit $\gamma d \rightarrow p\Theta^+K^-$. In order to calculate this upper limit, the CLAS acceptance must be determined along with a calculation of the photon flux (for normalisation). Details of the simulation performed to determine CLAS acceptance and the process of the photon flux calculation are presented in the following chapter.

Chapter 6

Data Analysis: Simulations and Acceptances

In the previous chapter, the results of the $\gamma d \rightarrow p K^+ K^- n$ analysis were presented, and ultimately the cross-section upper limit on Θ^+ production in this channel will be determined. In order to determine cross-sections and upper limits, the CLAS acceptance and photon normalisation must be computed.

The estimation of CLAS acceptance requires the creation of simulated events which are processed and analysed in the same manner as the real data. The simulation of events is a four stage process. First events are generated, then these events are passed through CLAS detector simulation and subsystem time smearing software, before finally being reconstructed (*cooked,* as described previously).

Although photon normalisation does not require simulation, it is a vital component of cross-section calculations and will therefore be described later in this chapter. Photon normalisation refers to the process by which the total number of photons, in a given energy bin, reaching the target over the duration of the experimental run is determined.

6.1   Monte Carlo Simulations

A $4 - body$ phase space was used as the starting point for the event generator, and $100M$ events were generated. These simulations were carried out at both torus settings used in the experiment ($3375A$ and $2250A$, i.e. high and low fields). Following the generation of events, the standard sequence of programs was used in these simulations: CLAS detector simulation, time smearing and data processing. The reconstructed data were analysed using the same analysis cuts and corrections, as were applied to the experimental data, with the exception of

momentum corrections.

6.1.1 GSIM and GPP

GSIM [86] is a GEANT [87] based simulation of the CLAS detector. Within GSIM, generated events are propagated through the simulated CLAS detector, generating a set of simulated hits (signals) in the various detector subsystems. These simulated particle tracks are then output in the standard CLAS BOS format and can be analysed with the same software as the experimental data.

However, GSIM produces simulated events with perfect timing resolution for each detector subsystem, which does not accurately reflect the timing resolution of CLAS. Consequently, before being ready for analysis, the GSIM output is further processed using a code called GPP [88], which smears the timing output of the drift chambers and time of flight subsystems to values more representative of true CLAS timing resolution. GPP also has the capability to remove dead cells from the drift chambers. This capability allows for the removal of simulated tracks, whose trajectory passed through known *holes* in the drift chamber (as determined from a database created via a monitoring process, during the experimental run).

6.1.2 Event Generator

The event generator [89] used was based on a $4 - body$ phase space model of $\gamma d \rightarrow pK^+K^-n$ (using PYTHIA [90]). Given the complexity of the possible reaction mechanism of Θ^+ production, and the lack of well developed theoretical models, *weighting factors* were applied to the generated events in order to better match kinematical distributions in the experimental data. These *weighting factors* were applied to the exponential $t-dependence$ of the K^+ and K^- momenta in the generated events to match those of the experimental data. The $4 - momentum$ transfer, t, for both $\gamma \rightarrow K^+$ and $\gamma \rightarrow K^-$, are defined as (after reduction):

$$t_{K+} = m_{K+} - 2(E_\gamma E_{K+} - E_\gamma P_{K+}^z) \tag{6.1}$$

$$t_{K-} = m_{K-} - 2(E_\gamma E_{K-} - E_\gamma P_{K-}^z) \tag{6.2}$$

where, m_{K+} is the mass of the K^+, E_γ is the energy of the photon, E_{K+} is the energy of the K^+ and P_{K+}^z is the z component of momentum of the K^+, and similarly for the K^-. In addition, the $4 - body$ phase space neutron momentum had a weighting factor applied again to better the match between simulated and

experimental data. Several iterations of this process were carried out until the $t-dependences$ of the simulated and experimental data reached agreement. Comparisons between the experimental and simulated data, for these $t-dependences$ and neutron momentum distributions after *weighting*, can be seen in figure 6.1 for the high field analysis (similar distributions for the low field can be found in Ref. [77]). Also shown in figure 6.1 is the comparison of photon energy distributions.

6.1.3   Kinematic Distributions

The level of agreement between the simulated and experimental data can be determined by the comparison of kinematic distributions. These comparisons were made for both the high and low field data, and with the application of the nominal/minimal analysis (as defined in chapter 5). The distributions shown in this section are from the high field analysis, with the low field equivalents again to be found in Ref. [77].

Figure 6.2 shows the comparisons between simulated and experimental data of the momentum and angular distributions, θ (degrees), for the proton and both kaons. θ is defined as:

$$\theta^{p,K^+,K^-}(radians) = cosine^{-1}(\frac{P_z^{p,K^+,K^-}}{P^{p,K^+,K^-}}) \qquad (6.3)$$

where, P^{p,K^+,K^-} is the momentum of the proton, K^+ or K^- respectively, and P_z^{p,K^+K^-} is the $z-component$ of momentum of the proton, K^+ or K^-.

As can be seen from these comparisons, the level of agreement between the simulation and the data is reasonable, considering the event generator used was a $4-body$ phase space, and does not include any specific reaction dynamics. One should consider that, given the G10 photon energy range, $1.5 - 3.6\,GeV$, there is significant phase space for the production of Λ^* resonances above the background component. The production of these resonances would clearly affect the kinematic distributions shown. However, the level of agreement (see section 6.2) between the simulated and experiment invariant masses, $M(nK^+)$, is more than sufficient for a CLAS acceptance to be determined.

6.1.4   Vertex Timing Distributions

Beyond the kinematic distributions of the simulated data (see section 6.1.3), the vertex timing distributions for all three final state particles (p, K^+, K^-) were
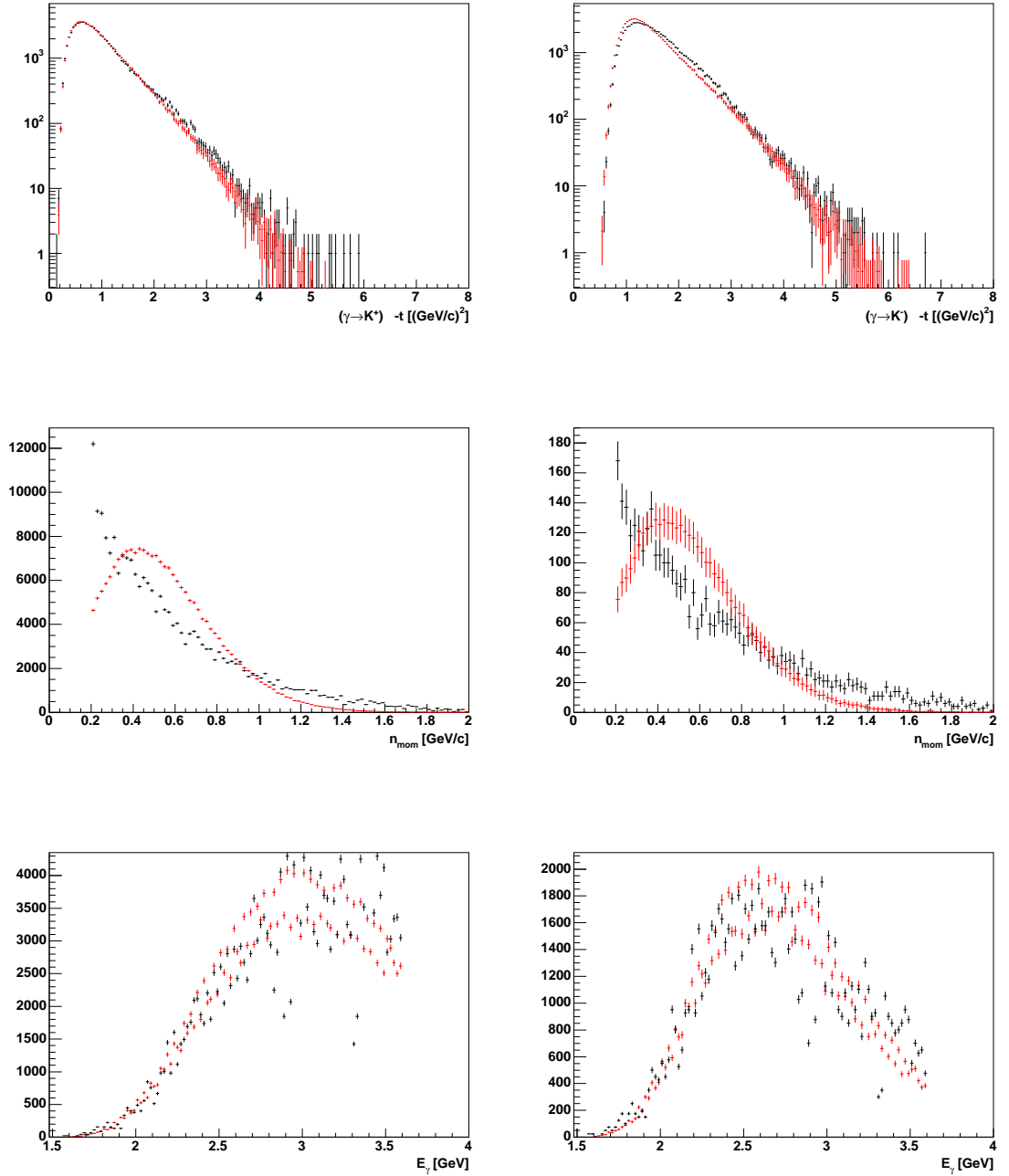
Figure 6.1: Comparison of simulated (red) and experimental data (black) distributions. $-t-dependences$ ($0.04\,(GeV/c)^2$ bins) for the reaction $\gamma d \rightarrow pK^+K^-(n)$ after exponential weighting for the K^+ (top left) and the K^- (top right), *Neutron* momentum distributions ($0.02\,GeV/c$ bins) before (middle left) and after (middle right) the $P_{K^+}^{max} < 1GeV/c$ cut and E_γ distributions ($0.02\,GeV$ bins) before (bottom left) and after (bottom right) the $P_{K^+}^{max} < 1GeV/c$ cut. All spectra are normalised by integrated number of counts. High field.
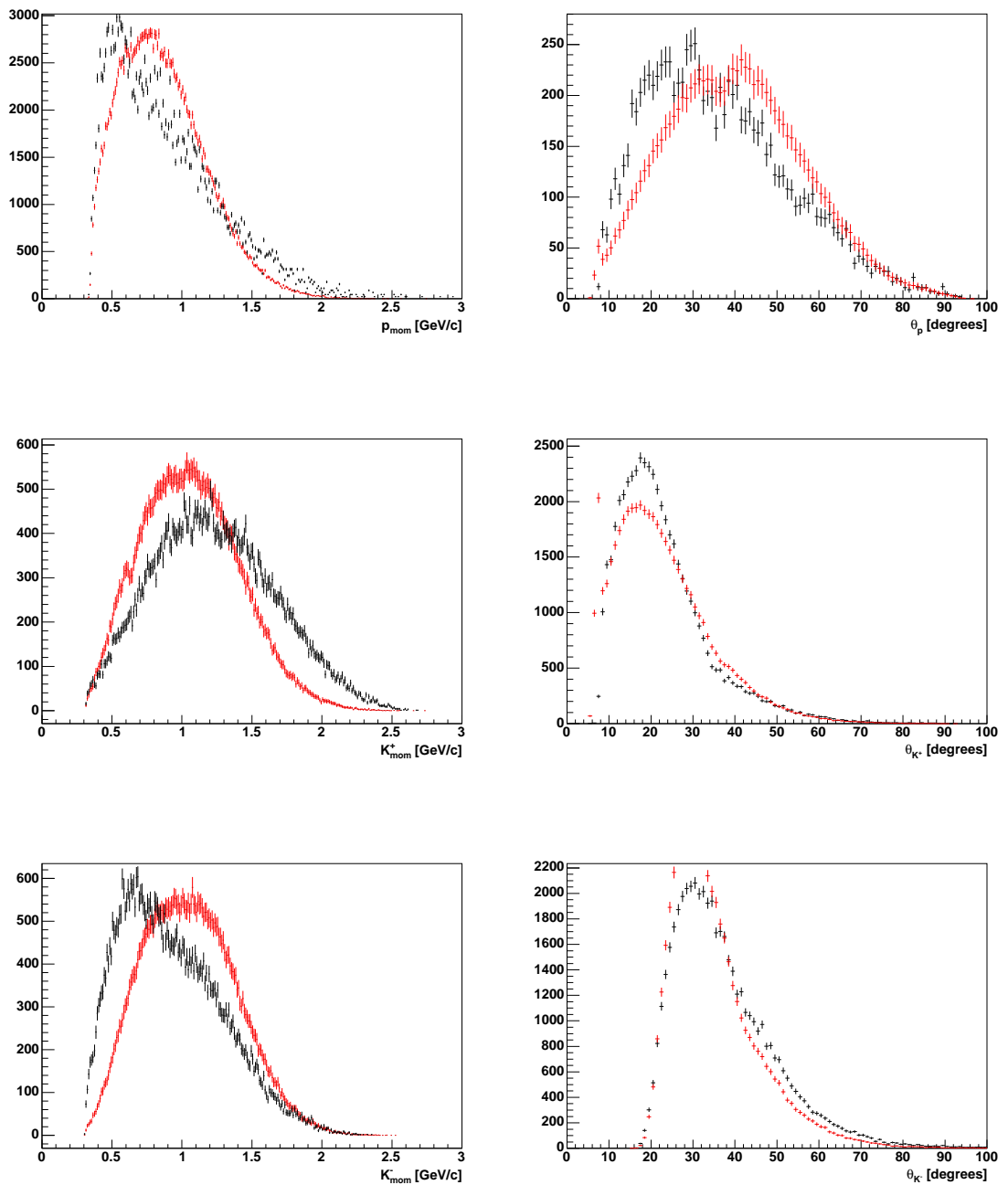
Figure 6.2: Comparison of simulated (red) and experimental data (black) distributions. Momentum distributions ($0.01\,GeV/c$ bins) for the proton (top left), K^+ (middle left) and K^- (bottom left). Angular distributions (1° bins) in $\theta(degrees)$ for the proton (top right), K^+ (middle right) and K^- (bottom left). All spectra are normalised by integrated number of counts. High field.

studied. It was found that the momentum dependence of the $hadron - photon$
vertex time was not smooth. This effect was attributed to the GPP time smearing
not being the same as the true time smearing (see section 6.1.1). However, given
that the velocity of a charged particle is calculated based on the flight time from
target to time of flight (see section 3.6.5), it was found that by loosening the
initial TOF mass cuts at the initial particle identification stage (in the analysis
of the simulated data) that a smoother momentum dependence was obtained.
Figure 6.3 shows the comparisons between simulated and experimental data of
this momentum dependent vertex time for the proton, K^+ and K^-, for the high
field data.

6.2   Acceptances

The acceptance of CLAS, for the reaction $\gamma d \to pK^+K^-n$, was determined from
the ratio of accepted (reconstructed) events to thrown (MC generated) events,
and was studied as a function of the invariant mass $M(nK^+)$. All nominal data
analysis cuts (as of chapter 5) were included in determining the accepted events
sample. Although no resonant contributions were included in the event generator,
the region of the invariant mass $M(pK^-)$ associated with the $\Lambda(1520)$ was cut
in the analysis of the simulated data, since this region would otherwise provide
a contribution to the background in $M(nK^+)$. The acceptance determination
includes all photon energies in the G10 range.

   Figures 6.4 & 6.6 show the $M(nK^+)$ spectrum comparison between the ex-
perimental and simulated data, the CLAS acceptance as a function of $M(nK^+)$,
and the acceptance corrected $M(nK^+)$ spectrum, for the high and low fields
respectively (all analysis cuts).

   Similarly, figures 6.5 & 6.7 show the $M(nK^+)$ spectrum comparison between
the experimental and simulated data, the CLAS acceptance as a function of
$M(nK^+)$, and the acceptance corrected $M(nK^+)$ spectrum, for the high and low
fields respectively (analysis without the K^+ momentum cut at $P_{K^+}^{max} < 1 GeV/c$).

   As can be seen from these figures (6.4, 6.5, 6.6 and 6.7), the CLAS acceptance
effects for the reaction $\gamma d \to pK^+K^-n$ are of the order $\sim 1\%$. Furthermore, over
the invariant mass range $(1.4 \, GeV/c^2 - 1.9 \, GeV/c^2)$, the acceptance for the low
field is slightly higher than that of the high field. This is to be expected in light
of the previous discussion about the magnetic field strength and torus polarity
(see section 3.6.1).

   These acceptances will be used in the calculation of cross-sections ($\gamma d \to$
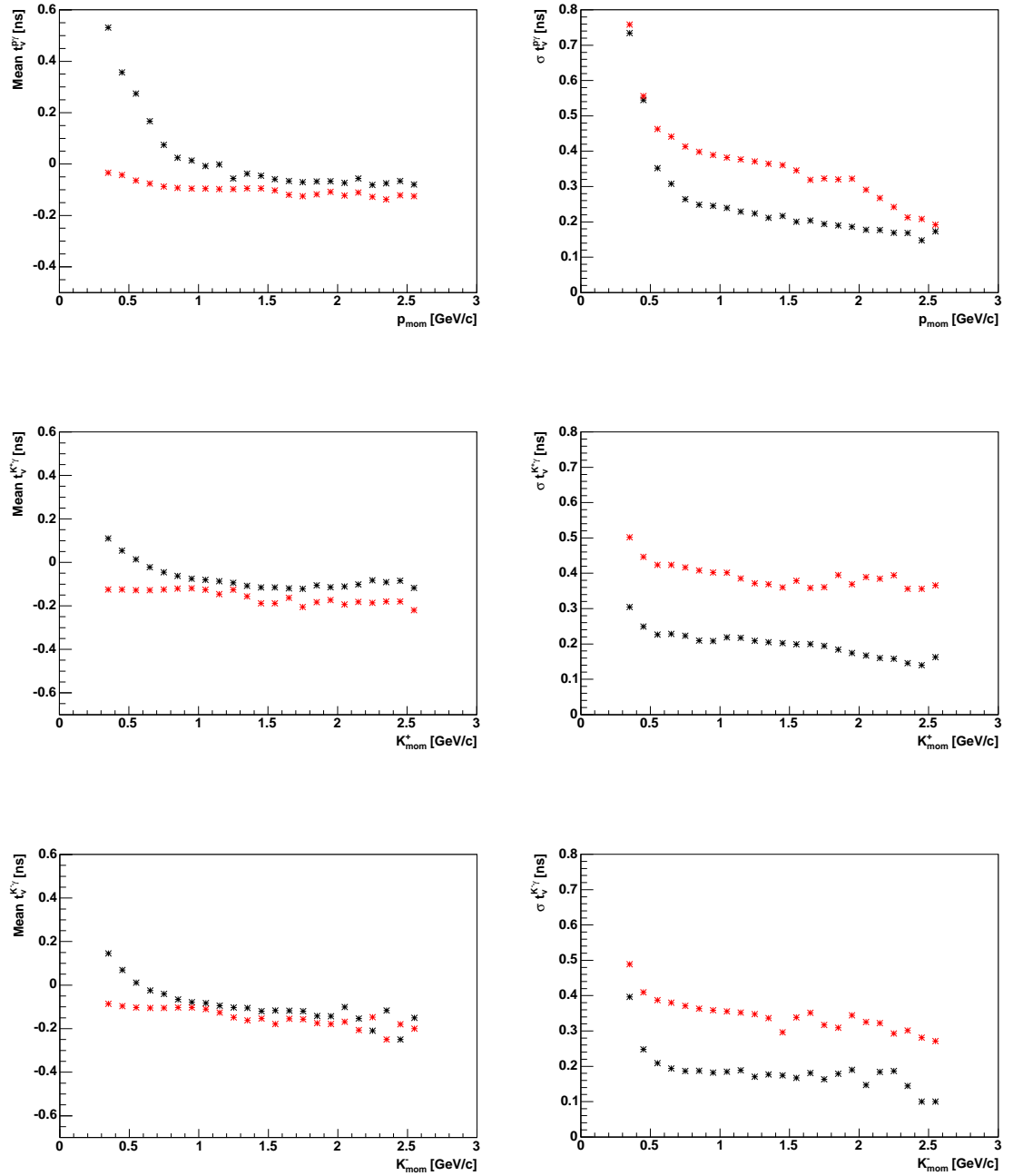
Figure 6.3: Comparison of simulated (red) and experimental data (black) distributions. The momentum dependence of vertex timing mean (left) and sigma (right), for the *Proton* (top). K^+ (middle). K^- (bottom). High field.
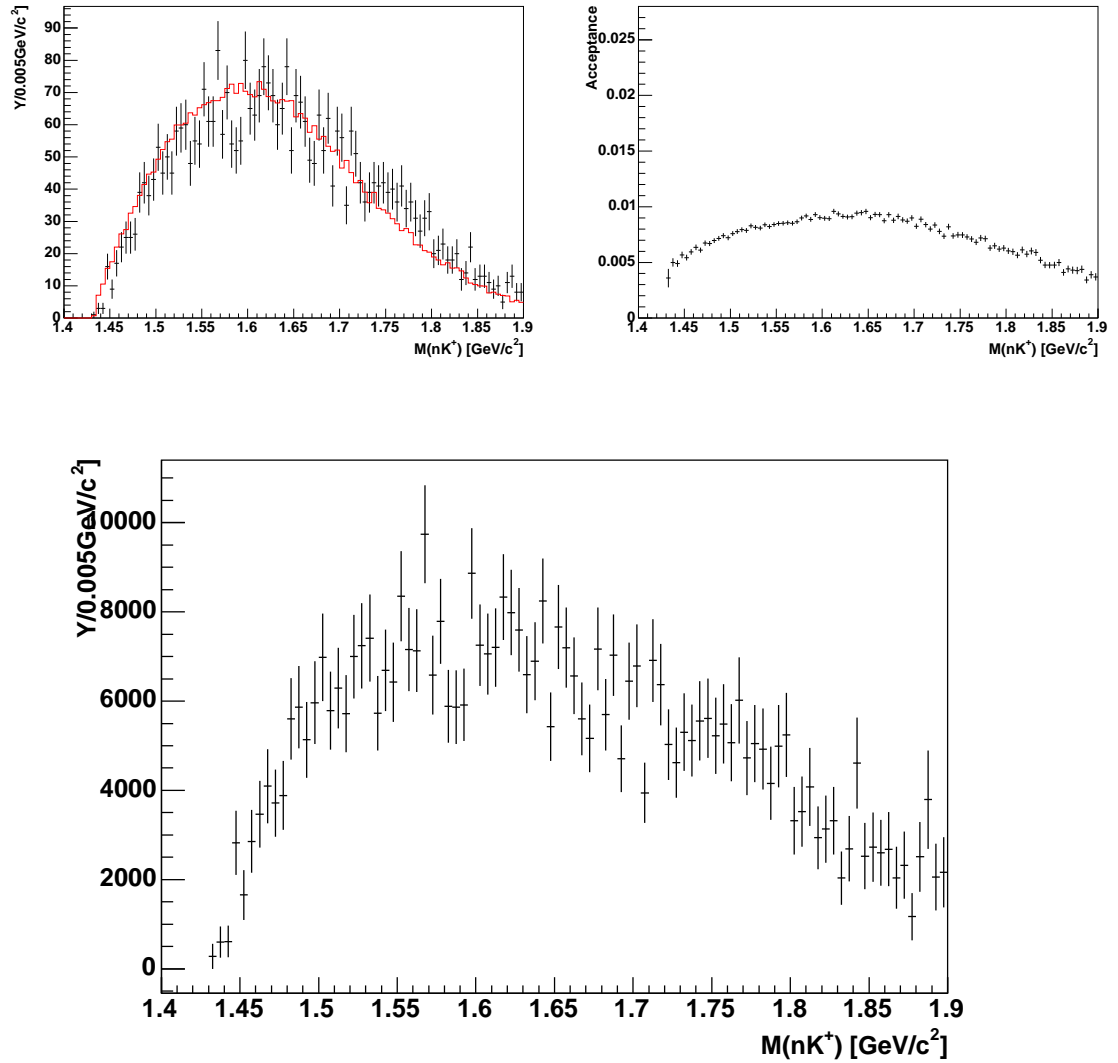
Figure 6.4: Top left: $M(nK^+)$ experimental data (black) and simulated (red), top right: acceptance as a function of $M(nK^+)$, bottom: acceptance corrected experimental data. High field (all analysis cuts).
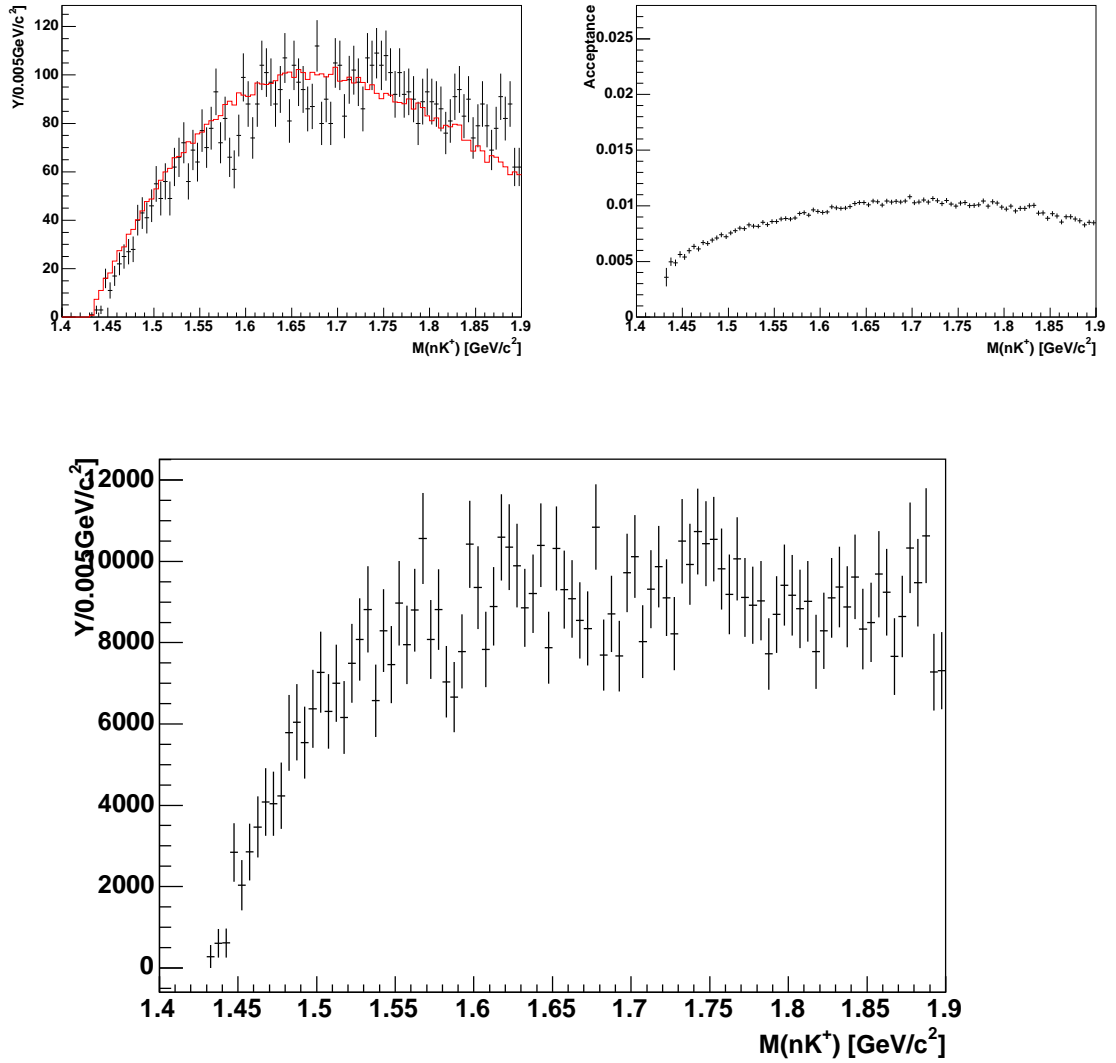
Figure 6.5: Top left: $M(nK^+)$ experimental data (black) and simulated (red), top right: acceptance as a function of $M(nK^+)$, bottom: acceptance corrected experimental data. High field (all analysis cuts except $P_{K^+}^{max} < 1 GeV/c$).
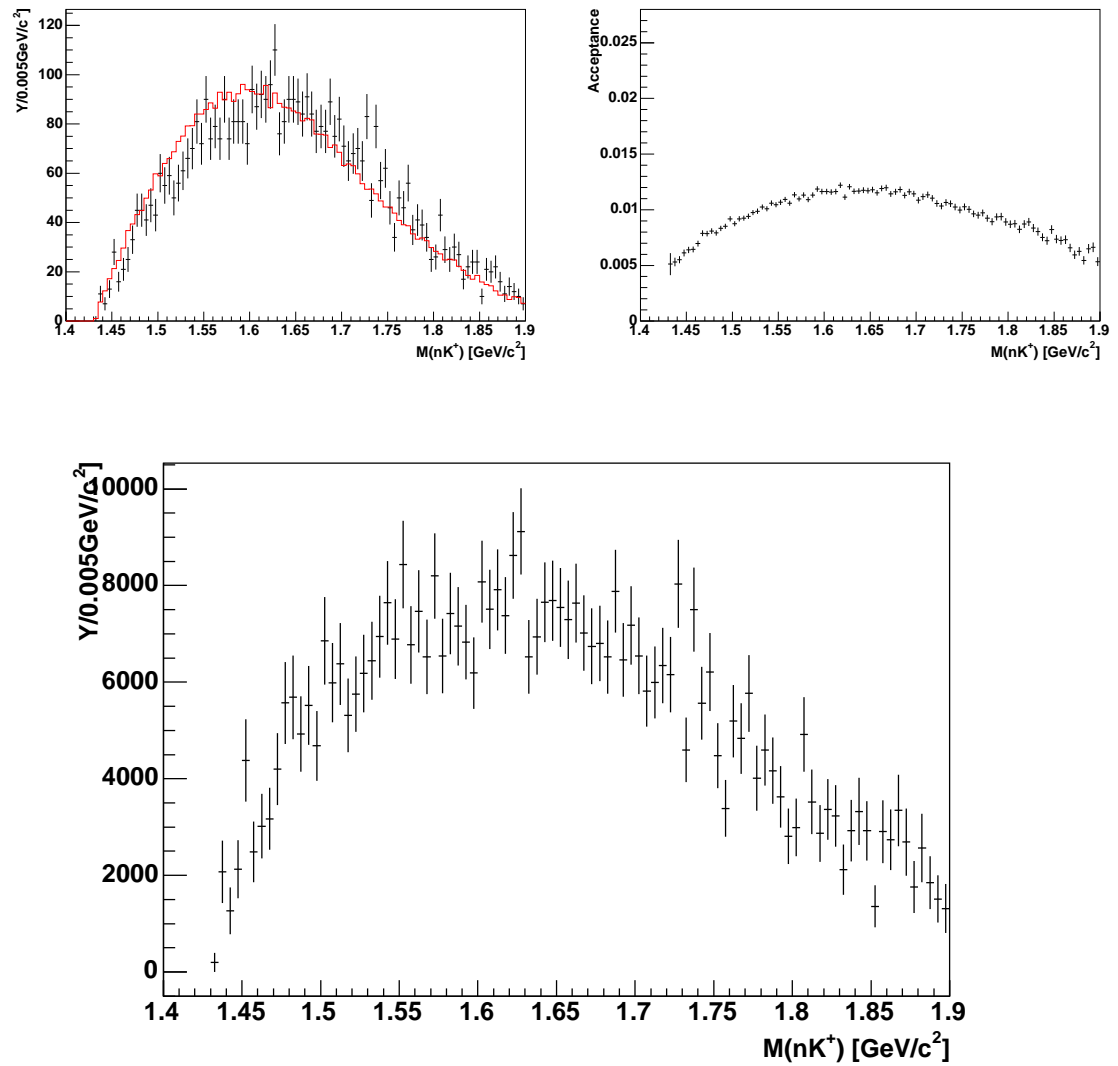
Figure 6.6: Top left: $M(nK^+)$ experimental data (black) and simulated (red), top right: acceptance as a function of $M(nK^+)$, bottom: acceptance corrected experimental data. Low field (all analysis cuts).
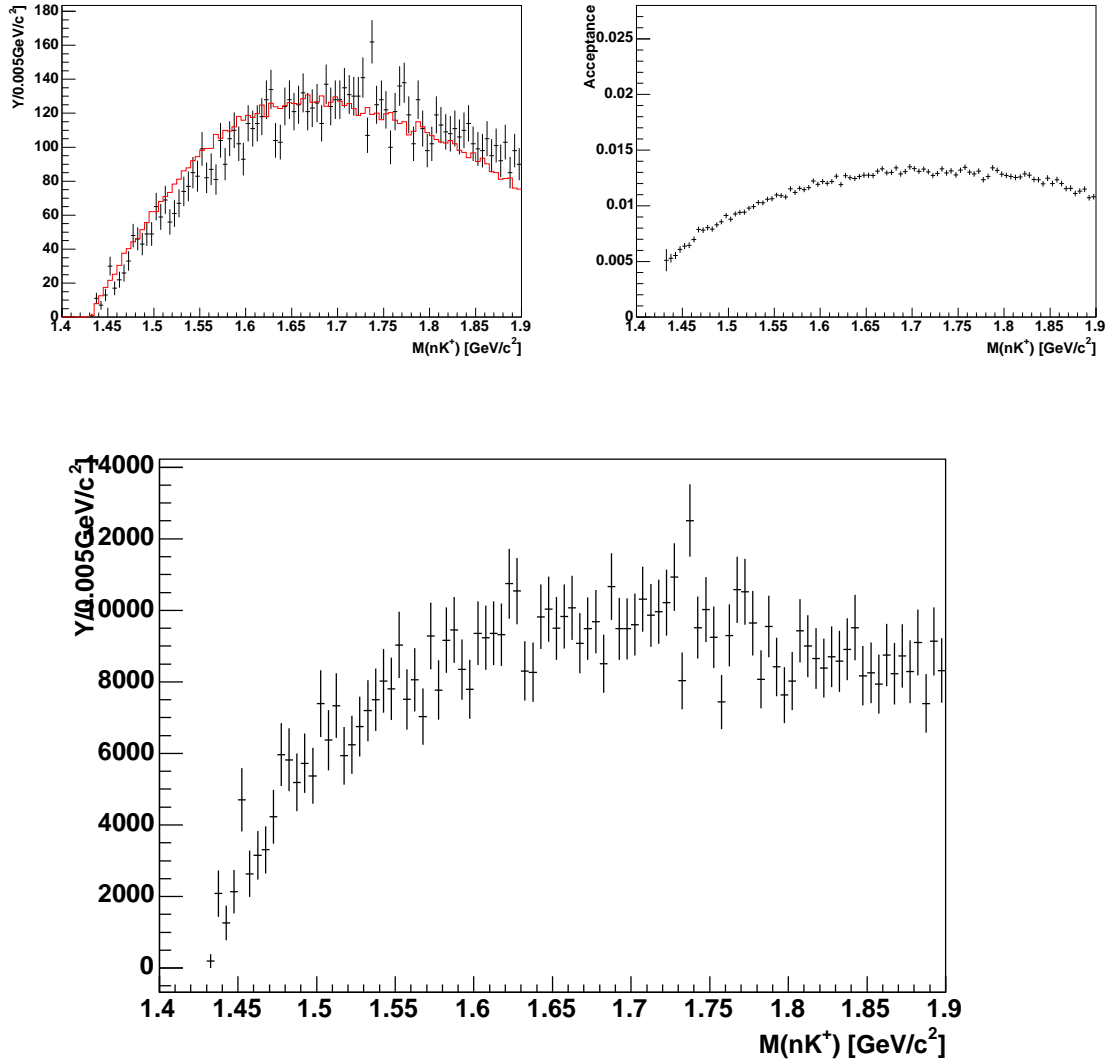
Figure 6.7: Top left: $M(nK^+)$ experimental data (black) and simulated (red), top right: acceptance as a function of $M(nK^+)$, bottom: acceptance corrected experimental data. Low field (all analysis cuts except $P_{K^+}^{max} < 1 GeV/c$).

pK^+K^-n) and upper limits ($\gamma d \to p\Theta^+K^-$) in the following chapter.

6.3   Invariant Mass $M(nK^+)$ Resolution

Further to the calculation of acceptances, the previously described simulations (see section 6.1) can be used to study the invariant mass $M(nK^+)$ resolution. The procedure for this study requires the calculation of the invariant mass using the generated $4-vectors$ of the neutron and K^+ and subtracting the invariant mass calculated using the reconstructed $4-vectors$, on an event by event basis. This calculation was carried out in 12 photon energy, E_γ, bins. Figure 6.8 shows an example of this difference and fit, in one of the E_γ bins.

χ^2 / ndf	25.03 / 12
Prob	0.0147
Constant	993.4 ± 14.0
Mean	0.0005743 ± 0.0000379
Sigma	0.003119 ± 0.000040
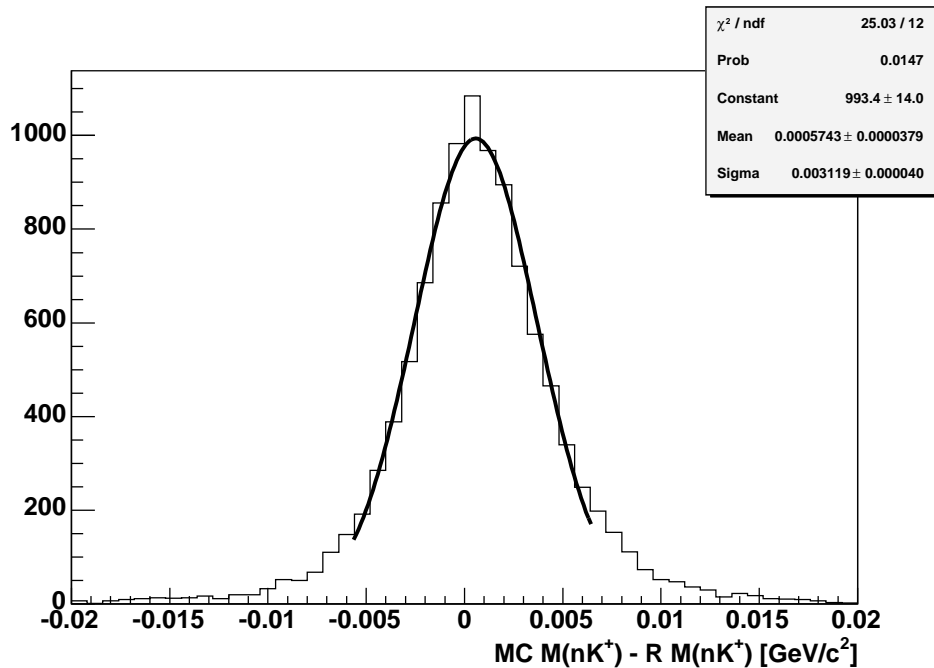
Figure 6.8: Difference in invariant mass $M(nK^+)$, as calculated by the Monte Carlo generated events (MC) and the reconstructed events (R). $2.0\,GeV/c^2 < E_\gamma < 2.25\,GeV/c^2$. High Field.

Given that the reconstructed 4-vectors have passed through the CLAS simulation and time smearing, this difference in the invariant mass can be attributed to the detector, and therefore allowing a determination of the mass resolution of CLAS. This resolution is dependent upon the simulation and the time smearing factors.

Figures 6.9 & 6.10 show the invariant mass resolution for the high and low fields respectively. The top of each figure shows the mean of the difference of in-

variant mass (described above) and the bottom shows the sigma of this difference. Both mean and sigma are shown as a function of photon energy E_γ. The mean for both field settings is less than $0.001\,GeV/c^2$, and the sigmas are $0.0033\,GeV/c^2$ and $0.0042\,GeV/c^2$, for the high and low fields respectively.
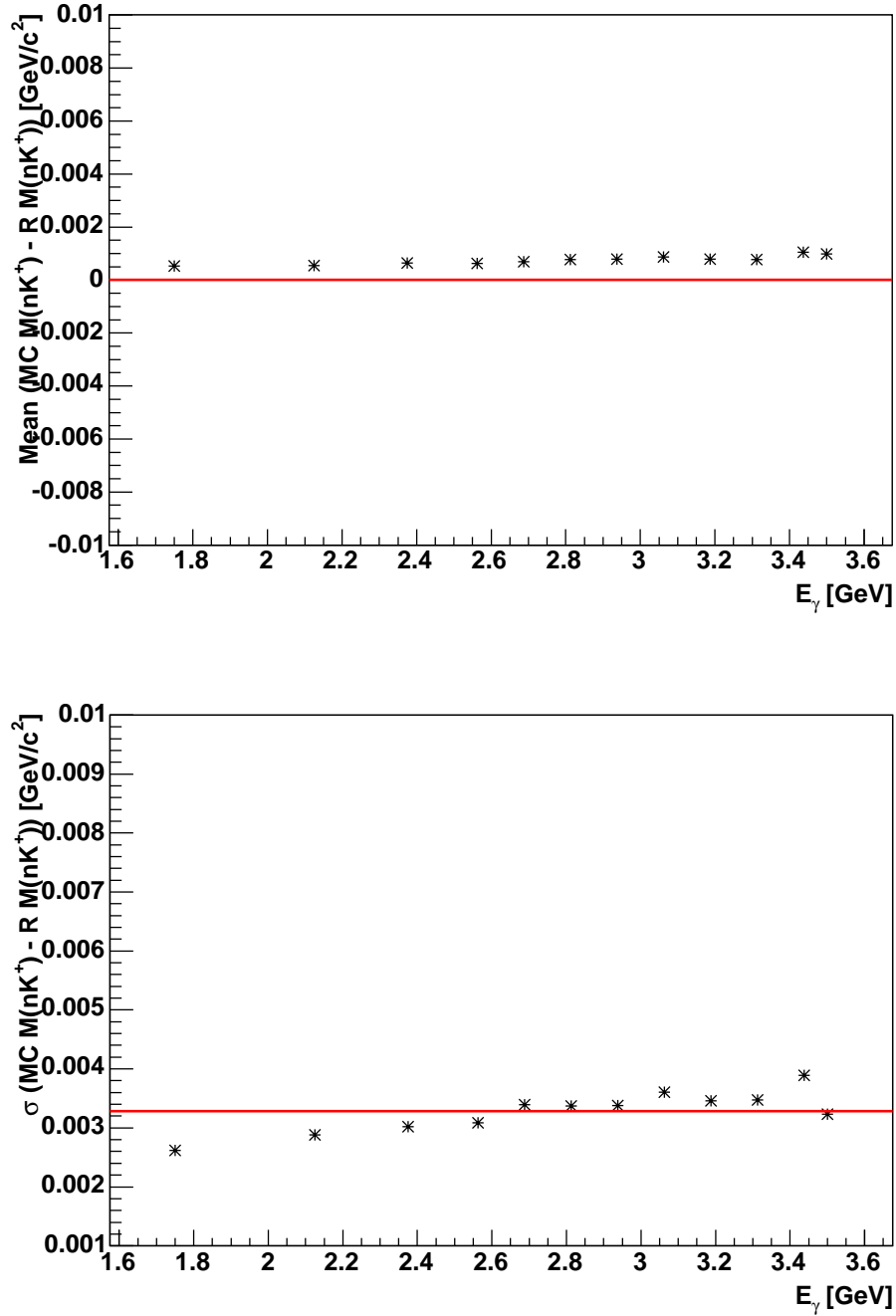
Figure 6.9: Invariant Mass Resolution for the High Field. Top: Mean $M(nK^+)$ as a function of E_γ (red line set at zero). Bottom: Sigma $M(nK^+)$ as a function of E_γ, with average (denoted by red line) $\sigma = 0.0033\,GeV/c^2$.
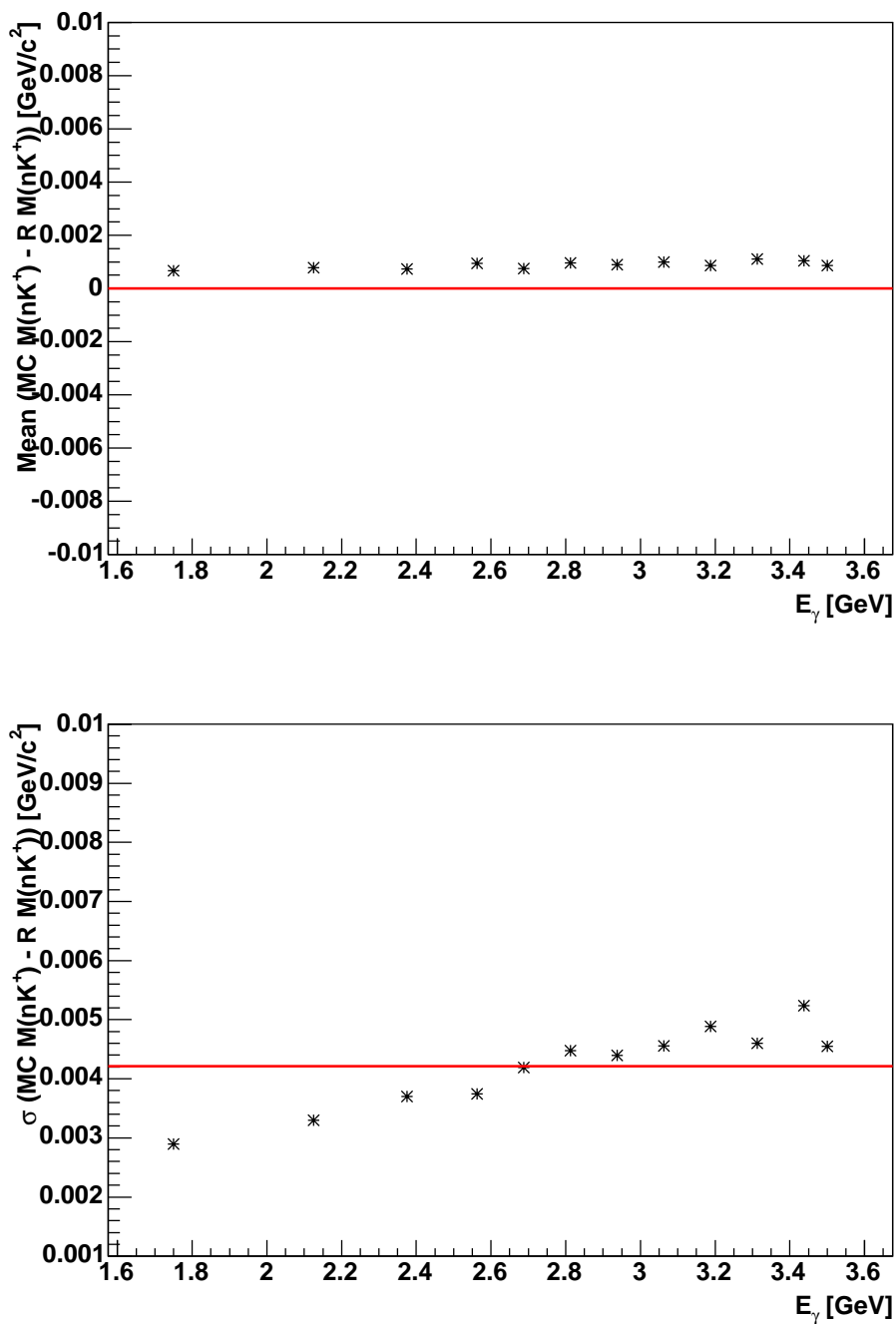
Figure 6.10: Invariant Mass Resolution for the Low Field. Top: Mean $M(nK^+)$ as a function of E_γ (red line set at zero). Bottom: Sigma $M(nK^+)$ as a function of E_γ, with average (denoted by red line) $\sigma = 0.0042\,GeV/c^2$.

Given the results of this invariant mass resolution study, one can be satisfied with the use of $0.005\,GeV/c^2$ binning when showing $M(nK^+)$ histograms.

6.4 Photon Normalisation / *GFlux*

As discussed previously, cross-section calculations require the number of photons incident on the target , N_γ, to be determined. The method used for the determination of this photon flux in the G10 analysis is known as *GFLUX* [91].

The main idea behind GFlux can be represented by the following relation:

$$N_\gamma^i = R^i \Delta T_{run} \qquad (6.4)$$

where, N_γ^i is the total photon flux within the energy range covered by a tagger T-bin, R^i is the rate of hits in that T-bin and ΔT_{run} is the time over which data were taken.

GFlux uses random, out of time hits in the tagger, which are not associated with the trigger, as its starting point to calculate N_γ^i. Central to determination of the rate, R^i, is the single hit nature of the tagger TDCs. Hits occurring $35\,ns$ to $150\,ns$ after the trigger hit (the hit satisfying the CLAS level 1 trigger), were considered by GFlux to be out of time. Given that a T-counter only registers the first hit which occurred during the active timing window, the probability for multiple out of time hits in the same T-counter is determined by Poisson statistics as:

$$P_{\geq 1} = 1 - e^{-R^i \Delta T_{out}} \qquad (6.5)$$

where, $\Delta T_{out} = 115\,ns$ is the width of the active timing window. The measured number of out of time hits for a given T-counter, N_{out}^i, can now be calculated, using this probability (equation 6.5), from the relation:

$$N_{out}^i = P_{\geq 1} N_{trig}^i = (1 - e^{-R^i \Delta T_{out}}) N_{trig}^i \qquad (6.6)$$

where, N_{trig}^i is the total number of random hits in the active timing window, that could have hit the ith counter. Solving equation 6.6 for the rate of hits in the TDC, R^i, gives:

$$R^i = \frac{-1}{\Delta T_{out}} ln(1 - \frac{N_{out}^i}{N_{trig}^i}) \qquad (6.7)$$

N_{trig}^i can be estimated by counting the total number of hits in the entire

tagger, N_{tot}, assuming that each TDC was active for the duration of the timing window. However, the single hit nature of the TDCs implies that it is possible for a T-counter not to have been active at all during the window. This would occur if the T-counter registered a hit before the out of time window became active at $35\,ns$. Therefore, to compensate for this possibility, N_{trig}^i is defined as the following:

$$N_{trig}^i = N_{tot} - N_{early}^i \tag{6.8}$$

where, N_{early}^i is the number of hits in the ith T-counter, before the opening of the timing window at $35\,ns$. The rate, R^i, defined by equation 6.7, is the rate at which photons are tagged by the ith T-counter.

The final requirement is to determine the number of photons which were incident on the target. This requires taking account of photons lost between the tagger and the target, referred to as the beamline transmission function. For this purpose, low beam intensity normalisation runs were conducted, utilising the total absorption shower counter (TA(S)C see section 3.7). The TA(S)C measures the photon flux downstream of the tagger, and differences between this flux and that measured at the tagger provide a determination of this beamline transmission function. Furthermore, it should be noted that this correction overestimates the photon loss in the beamline, since the total absorption shower counter is situated $\sim 15\,m$ downstream of the target, therefore leading to an additional loss, η, along the beamline between the target and the TA(S)C. The final correction for this overall loss of photons along the beamline, for a given T-bin, ϵ^i, is defined by:

$$\epsilon^i = \left(\frac{N_{coin}^i}{N_{tag}^i}\right)(1 + \eta) \tag{6.9}$$

where, N_{tag}^i is the number of hits in the given T-counter and N_{coin}^i is the number of hits in the given T-counter, with a coincident hit in the TA(S)C.

The last step required to calculate the photon normalisation is a measurement of ΔT_{run}, the experimental run time over which data were taken. This is calculated using the following relation:

$$\Delta T_{run} = \Delta T_{clock} L_t \tag{6.10}$$

where, ΔT_{clock} is the run-gated clock time, and L_t is the livetime fraction of ΔT_{clock} in which the detector systems are actually active (the systems become inactive during event readout). L_t is given by:

$$L_t = \frac{N_{tot}}{N_{scal}} \qquad (6.11)$$

where, N_{tot} is as previously defined, and N_{scal} is the total number of hits counted by the scalers during event readout.

Consequently, using the above relations and definitions, it is possible to calculate the photon normalisation:

$$N_\gamma^i = R^i \Delta T_{run} \epsilon^i \qquad (6.12)$$

The GFlux calculated number of photons incident on the target (during the G10 experiment) was $2.5 \times 10^{13} \pm 0.75 \times 10^{12}$ and $2.7 \times 10^{13} \pm 0.81 \times 10^{12}$, for the high and low field data respectively.

Summary

Details of the $4-body$ phase space simulations and the consequent determination of CLAS acceptance have been presented in this chapter. This CLAS acceptance together with the calculated photon flux, which was also detailed, are the major components necessary for a cross-section calculation. The calculation of the cross-section and the subsequent determination of the upper limit are presented in the following chapter.

Chapter 7

Data Analysis: Cross-Sections and Upper Limits

It is clear from figures 5.19 and 5.20 that there is no obvious Θ^+ signal in the invariant mass $M(nK^+)$ spectrum obtained as a result of this analysis of $\gamma d \to pK^+K^-n$. Consequently, further to reporting a null observation, a quantitative statement regarding the result of this analysis is necessary. This statement takes the form of a cross-section upper limit for production of the Θ^+ via the reaction $\gamma d \to p\Theta^+K^-$: $\Theta^+ \to nK^+$.

In order to determine the cross-section upper limit for Θ^+ production, the invariant mass $M(nK^+)$ spectra were corrected for CLAS acceptance, and normalised by the target and photon flux (luminosity). The acceptance and photon flux determinations are found in the previous chapter 6. The resulting cross-section spectra were fitted with a third order polynomial which was held constant. By scanning a Gaussian peak (with fixed width) across the spectrum, the number of events above or below the polynomial *background* were used to determine the cross-section upper limit, by the *Feldman & Cousins* approach [92].

These cross-sections ($\gamma d \to pK^+K^-n$), and upper limits ($\gamma d \to p\Theta^+K^-$), are calculated for both field settings and for the combined fields analysis. Furthermore, the differential cross-section upper limits, as a function of angle, are determined and presented for each of these cases. The cross-section upper limit for the combined fields analysis, and the resulting differential cross-section upper limit, are the quantitative statement of result from this analysis since no Θ^+ signal was observed.

7.1   Cross-Section $\gamma d \to p K^+ K^- n$

The first stage in the calculation of the cross-section upper limit $\gamma d \to p \Theta^+ K^-$ is the determination of the cross-section of the reaction $\gamma d \to p K^+ K^- n$. The total cross-section σ, as a function of $M(nK^+)$, of the process $\gamma d \to p K^+ K^- n$ is computed using the following definition:

$$\sigma = \frac{N}{AccL} \tag{7.1}$$

where, N is the number of counts in the mass bin, Acc is the acceptance in the mass bin, and L is the luminosity, defined as:

$$L^{-1} = \frac{A}{\rho l N_A \gamma} \tag{7.2}$$

where,

A = atomic mass weight of deuterium = $2.0140 gmol^{-1}$

ρ = density of liquid deuterium = $0.163 gcm^{-3}$

l = target length = $24cm$

N_A = Avogadros number = $6.022 \times 10^{23} mol^{-1}$

γ = GFlux (photon flux) = $2.5 \times 10^{13} \pm 0.75 \times 10^{12}$ (high field) / $2.7 \times 10^{13} \pm 0.81 \times 10^{12}$ (low field)

This results in a luminosity of $29.2 \pm 0.87 \, pb^{-1}$ for each the high field setting, and $31.5 \pm 0.94 \, pb^{-1}$ for the low field.

Using the data spectrum, the CLAS acceptance, and normalising the subsequent acceptance corrected $M(nK^+)$ spectrum by the target and photon flux (luminosity, as defined above), results in a calculation of the cross-section of $\gamma d \to p K^+ K^- n$ as a function of invariant mass $M(nK^+)$.

This calculation is done for the 4 cases as of the previous chapters 5 and 6. Figure 7.1 shows the analysis of one of these cases (high field data with no $P_{K^+}^{max} < 1 GeV/c$ cut). The top left of the figure is $M(nK^+)$ spectrum from the data, the top right is the acceptance for the case and the bottom is the cross-section. Figure 7.2 shows the cross-sections for these 4 cases.
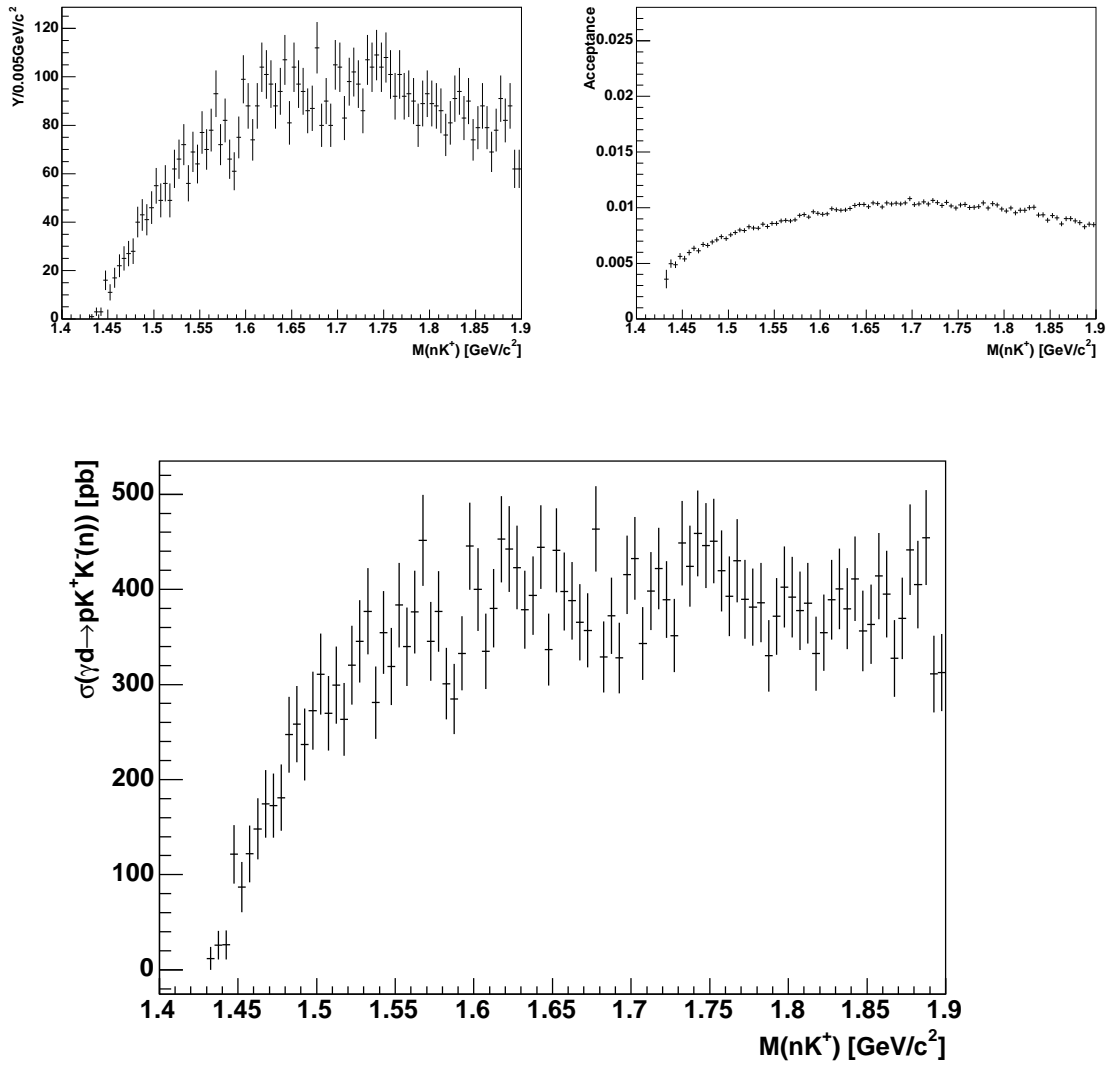
Figure 7.1: High Field (all analysis cuts except $P_{K^+}^{max} < 1GeV/c$) : $M(nK^+)$ spectrum (top left), acceptance (top right), and cross-section as defined previously [pb] (bottom).
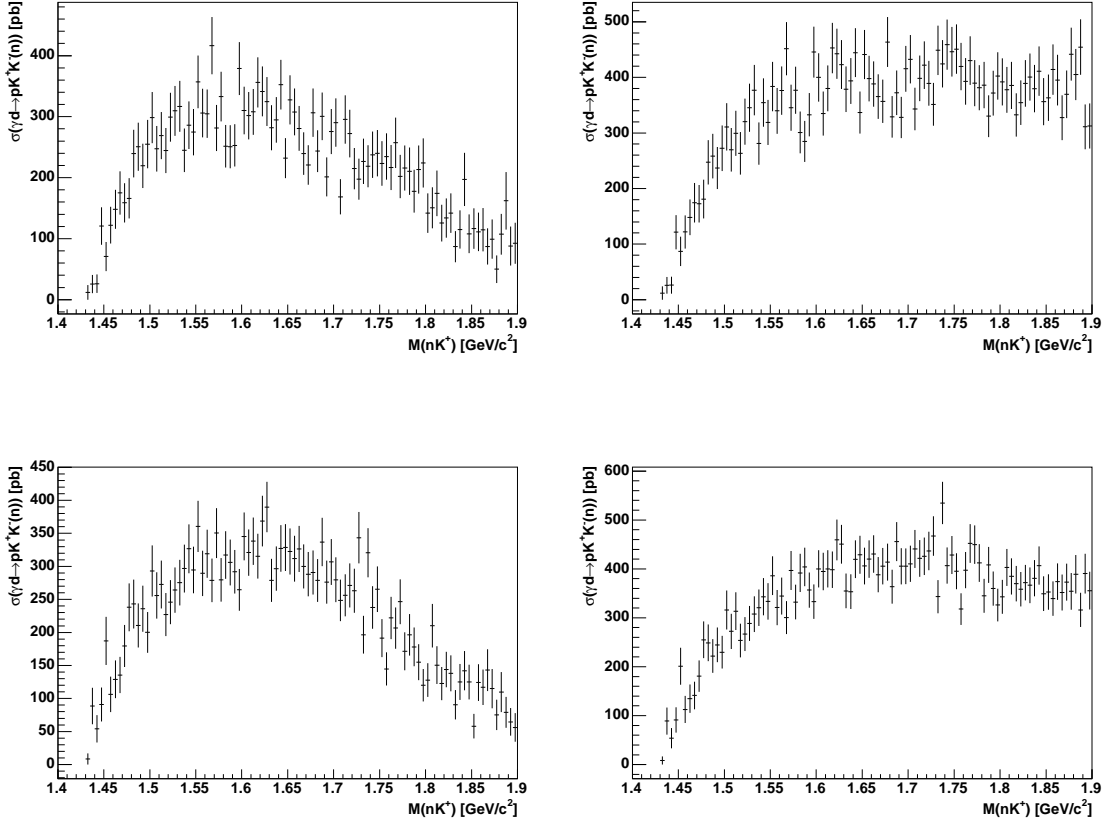
Figure 7.2: Cross-Section $\gamma d \rightarrow pK^+K^-n$ as defined previously [pb]. Top row: high field, Bottom row: low field. Left column: all analysis cuts, Right column: all analysis cuts except $P_{K+}^{max} < 1 GeV/c$.

As can be seen from these figures, the cross-sections are in close agreement with and without the K^+ momentum cut (for each field), and in comparison between both field settings.

7.2   Upper Limit Cross-Section $\gamma d \rightarrow p\Theta^+ K^-$

The method employed for the estimate of the upper limit of $\gamma d \rightarrow p\Theta^+ K^-$ is based upon the strength of a Gaussian peak above a smooth background. A Gaussian peak is scanned across the region of interest and the number of events above or below a polynomial *background* is determined and used to calculate the cross-section upper limit of a possible Θ^+. The *background* fit and Gaussian scan are performed on the cross-section spectrum (see figure 7.2). The background is fitted in the range $1.48 - 1.78 GeV/c^2$ by a $3rd-order$ polynomial, and once this background has been fixed, the region of interest $1.5 - 1.7 GeV/c^2$ is scanned in

steps of $5MeV/c^2$, using a Gaussian of fixed width, $\sigma = 5.5 \, MeV/c^2$ (the width of the Gaussian was chosen to be bigger than the bin width).

The upper limit on the cross-section $\gamma d \rightarrow p\Theta^+ K^-$ is then determined using the previously described method of section 7.1 and the definition:

$$\sigma = \frac{N_G}{AccL} \frac{1}{B.R.} \tag{7.3}$$

where the components are defined as previously (see section 7.1). However now, N_G is the number of counts in the Gaussian (*Feldman & Cousins* approach), and $B.R.$ is the branching ratio for $\Theta^+ \rightarrow nK^+$, which is assumed to be 0.5 (since isospin symmetry predicts that the Θ^+ should have an equal branching ratio into both nK^+ and pK^0). Again all 4 cases are studied, and figure 7.3 shows these estimated upper limits by the *Feldman & Cousins* approach (red lines). These upper limits are also calculated *by hand* for comparison to the *Feldman & Cousins* approach. Here, N_G is the strength in the Gaussian, which is taken as the number of counts plus 2 standard deviations (for 95% confidence level (c.l.)). The results obtained by this method are shown by the black lines in figures 7.3. One should note that in all subsequent determinations or quotes of upper limits, the values come from the *Feldman & Cousins* approach, and that from this point onwards in the calculation of cross-section upper limits, the *minimal* analysis condition with no cut on the K^+ momentum, ($P_{K^+}^{max} < 1GeV/c$), is analysed.

Feldman & Cousins

The *Feldman & Cousins* approach allows the determination of proper confidence level boundaries for small signals over a background, whilst accounting for the constraint that the *true* signal yield is bound to be positive. Additionally, this method decouples the goodness-of-fit confidence level from the confidence level interval. Use of this method has become the standard in experiments with weak or non-existent signals, and a detailed description can be found in Ref. [92]. As an example, figure 7.4 shows a confidence level (95% c.l.) band obtained from the fitting procedure described previously. The upper limit is obtained by intersecting the measured value, the red line in the plot, with the upper boundary of the confidence level band.
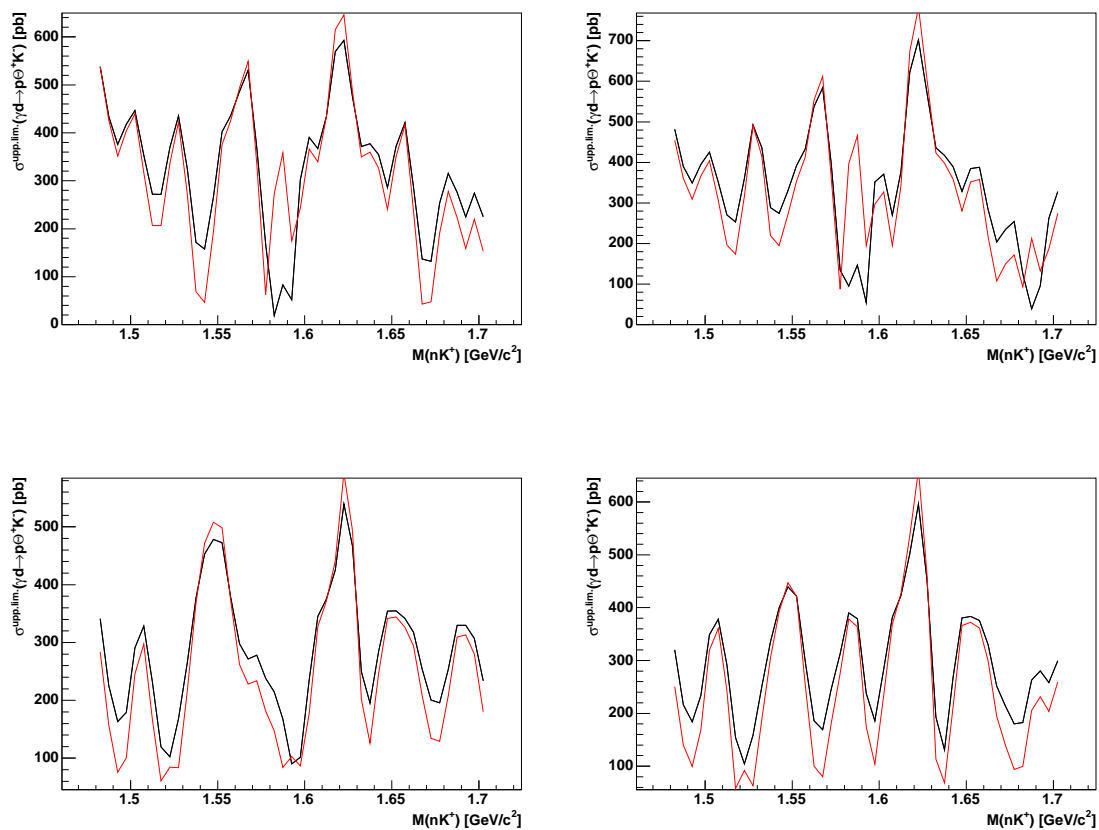
Figure 7.3: Upper limit cross-section (95% c.l.) $\gamma d \rightarrow p\Theta^+ K^-$ [pb]. Top row: high field, Bottom row: low field. Left column: all analysis cuts, Right column: all analysis cuts except $P_{K^+}^{max} < 1 GeV/c$. Red lines are by *Feldman & Cousins* approach.
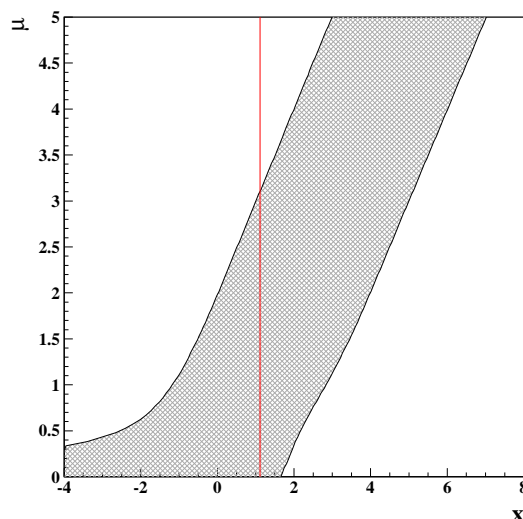
Figure 7.4: An example of a 95% confidence level band. The axes show the measured (x) and *true* values (μ), in units of σ.

7.3 Upper Limit as a function of $cos\theta_{cm}^{nK^+}$

The next step is to determine the differential cross-section upper limit, as a function of $cos\theta_{cm}^{nK^+}$, where, $\theta_{cm}^{nK^+}$ is the angle of the nK^+ system (corresponding to the Θ^+ decay) in the centre-of-mass frame (γd). For the purposes of this study 4 $cos\theta$ bins were chosen (see table 7.1).

Bin	$cos\theta_{min}$	$cos\theta_{max}$
1	-1.0	-0.5
2	-0.5	0.0
3	0.0	0.5
4	0.5	1.0

Table 7.1: cosine θ bins.

For each of these 4 bins, the acceptance, cross-section $\gamma d \rightarrow pK^+K^-(n)$ and upper limit $\gamma d \rightarrow p\Theta^+K^-$ are determined, using the procedures described previously in this chapter. Figure 7.5 shows an analysis for one of these $cos\theta$ bins, $(-1.0 \rightarrow -0.5)$, for the high field. Top left shows the comparison between the invariant mass $M(nK^+)$ from the experimental data (black), and the simulation (red). Top right shows the resulting acceptance as a function of $M(nK^+)$, for this angular bin. Middle left shows the acceptance corrected spectrum. Middle right shows the differential cross-section $\gamma d \rightarrow pK^+K^-n$, in this angular bin. Bottom histogram in the figure shows the differential cross-section upper limit $\gamma d \rightarrow p\Theta^+K^-$, as a function of $M(nK^+)$, for this angular bin.
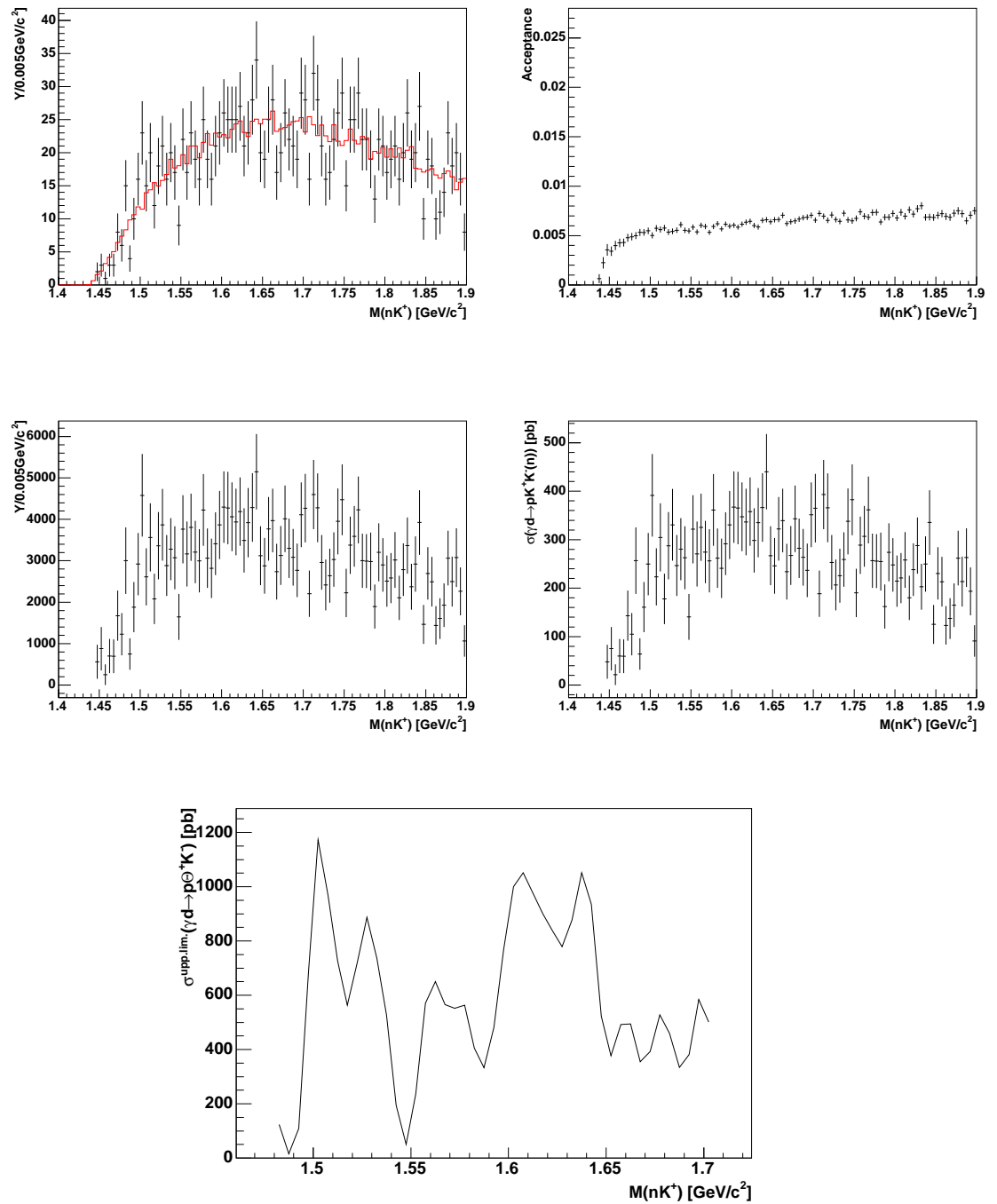
Figure 7.5: $cos\theta = -1.0 \rightarrow -0.5$. High Field. Shown are differential cross-sections.

Similar figures for the remaining three angular bins in the high field analysis, and the equivalent four low field angular bins, can be found in Ref. [77]. The four differential cross-sections, and differential cross-section upper limits, for each angular bin can be seen in figure 7.6 for the high field, and figure 7.7 for the low field.
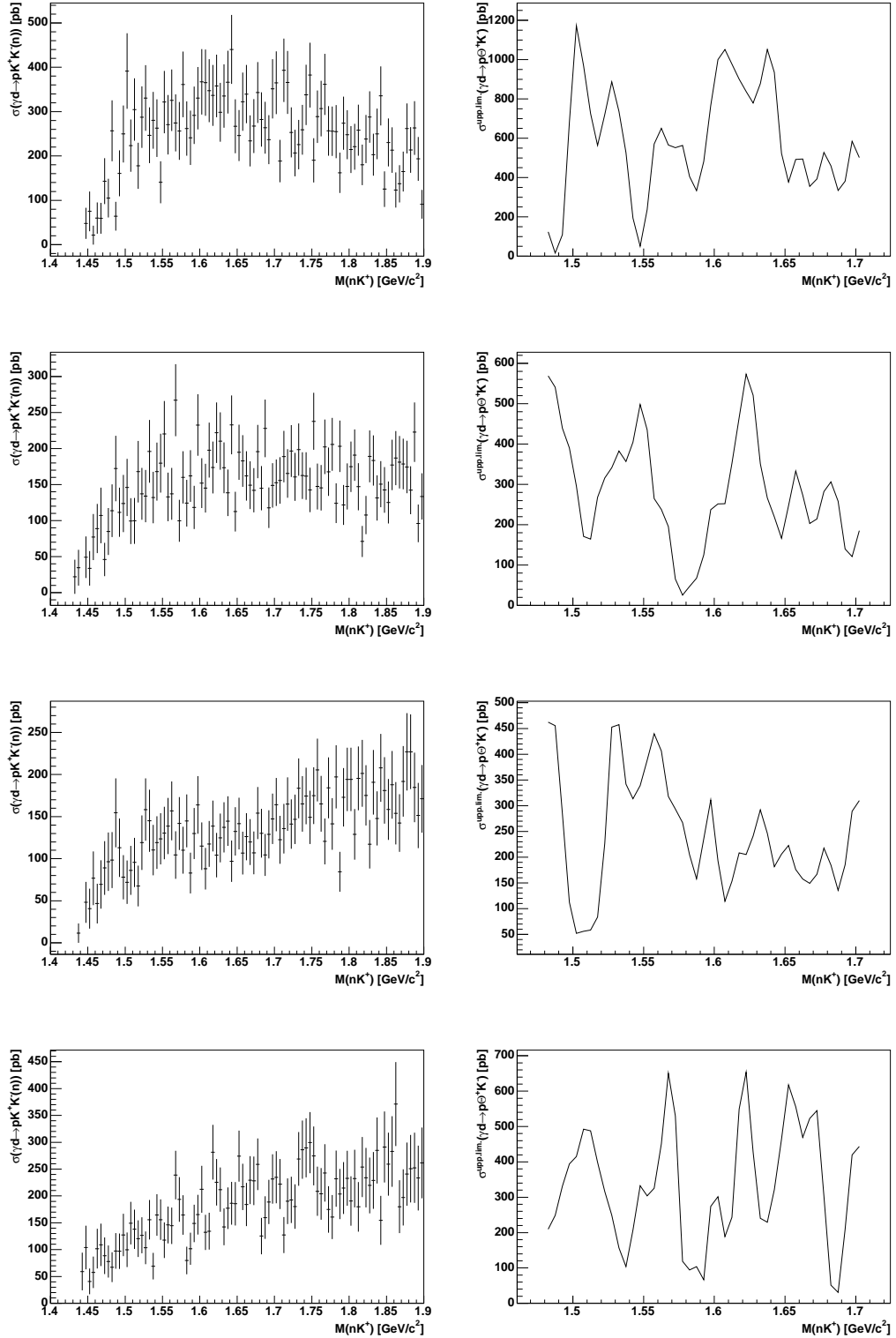
Figure 7.6: 4 *cosθ* bins, showing differential cross-section (left) and differential cross-section upper limit (right). Top: $cos\theta = -1.0 \rightarrow -0.5$, Upper middle: $cos\theta = -0.5 \rightarrow 0.0$, Lower middle: $cos\theta = 0.0 \rightarrow 0.5$, Bottom: $cos\theta = 0.5 \rightarrow 1.0$. High Field. Shown are differential cross-sections.
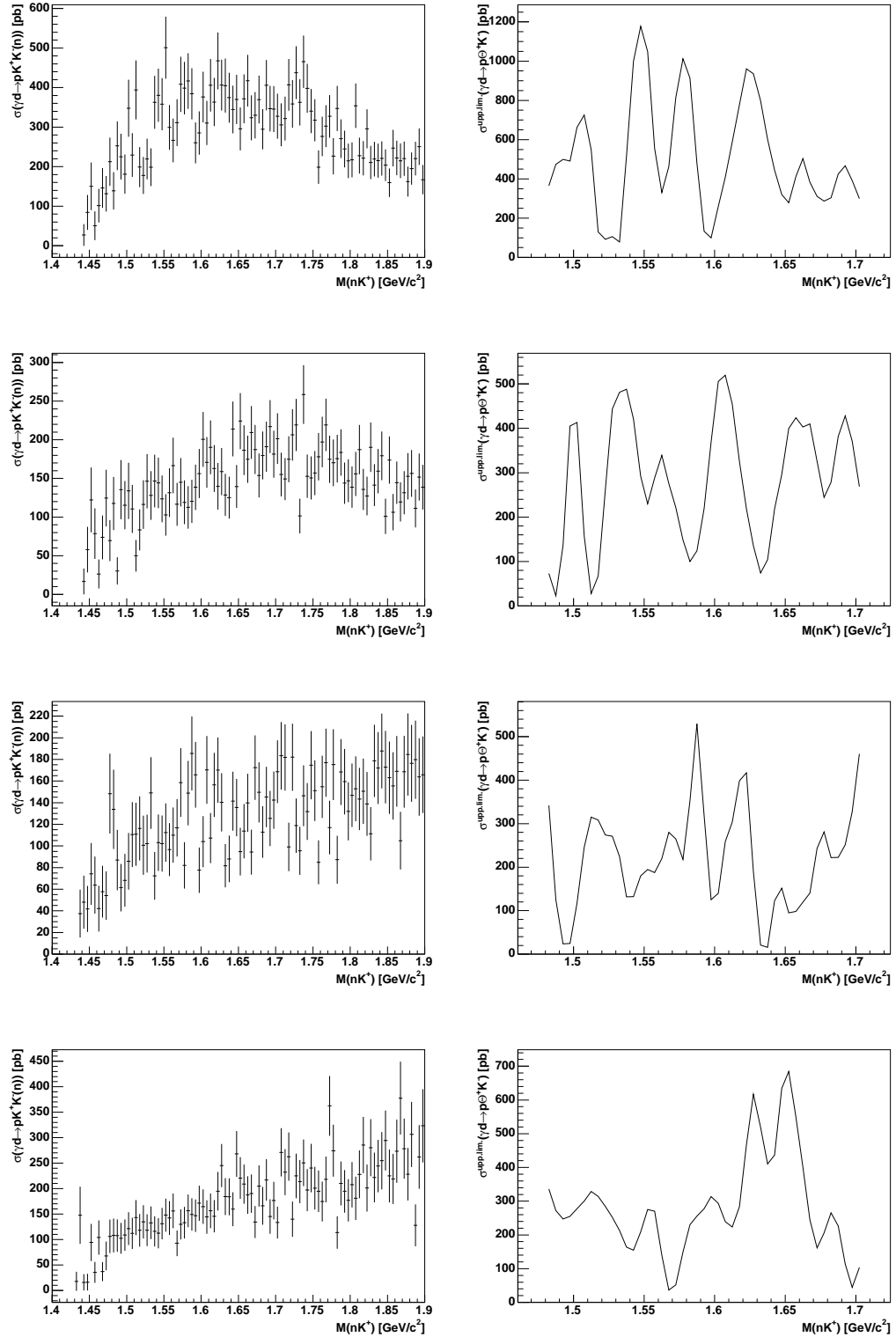
Figure 7.7: 4 *cosθ* bins, showing differential cross-section (left) and differential cross-section upper limit (right). Top: *cosθ* = −1.0 → −0.5, Upper middle: *cosθ* = −0.5 → 0.0, Lower middle: *cosθ* = 0.0 → 0.5, Bottom: *cosθ* = 0.5 → 1.0. Low Field. Shown are differential cross-sections.

To study the behaviour of the upper limit as a function of $cos\theta_{cm}^{nK^+}$, an invariant mass *range of interest* was selected. This range was chosen to be $1.52 - 1.56\,GeV/c^2$, since this spans the mass range within which previous observations of a possible Θ^+ have been made (see table 1.1). For each of the 4 $cos\theta$ bins, the maximum upper limit in this mass range was determined. Figure 7.8 shows this maximum upper limit as a function of $cos\theta_{cm}^{nK^+}$, for the high field (left) and low field (right).
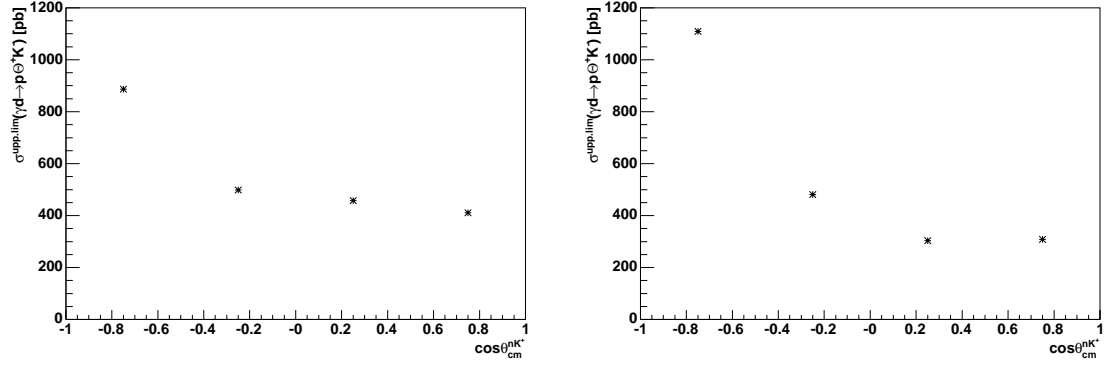
Figure 7.8: Maximum Upper Limit in the range $1.52 - 1.56\,GeV/c^2$, as a function of $cos\theta_{cm}^{nK^+}$, for High Field (left) and Low Field (right).

7.4   Combined Fields Cross-Section & Upper Limit

So far in this analysis both field settings, high and low, have been shown as separate data sets. However, since each have a calculated CLAS acceptance and a consequent acceptance corrected data $M(nK^+)$ spectrum, they can be combined into one data set, and the cross-section upper limit $\gamma d \rightarrow p\Theta^+ K^-$ can be determined. This upper limit is the result of this analysis of the reaction channel $\gamma d \rightarrow pK^+K^-n$.

Starting with the high and low fields acceptance corrected spectra, an addition of yields (on a bin-by-bin basis) was performed (figure 7.9 shows this combined yield), and a similar analysis as described previously in this chapter was conducted in order to calculate the cross-section $\gamma d \rightarrow pK^+K^-(n)$, and cross-section upper limit $\gamma d \rightarrow p\Theta^+ K^-$.
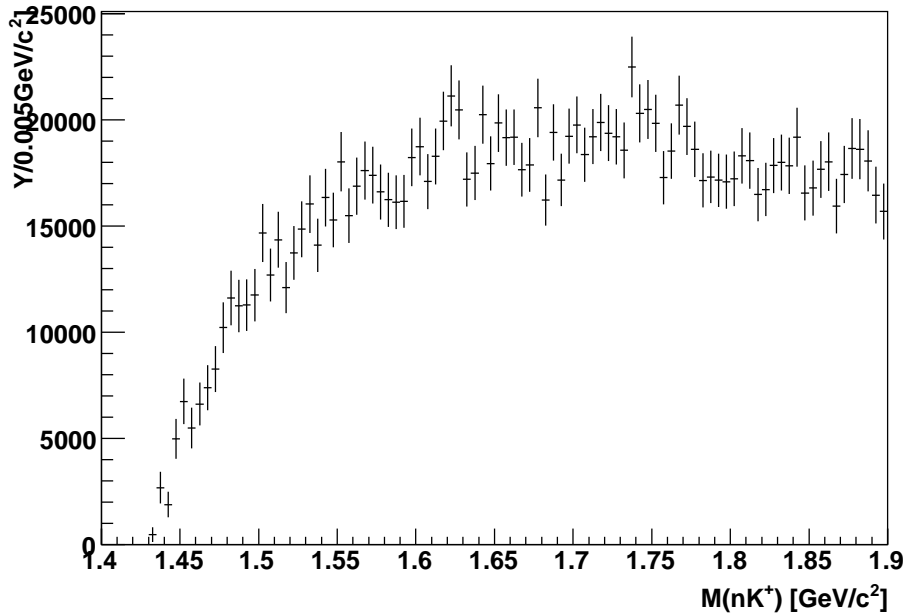
Figure 7.9: Combined Fields: Acceptance corrected yield addition.

Figure 7.10 shows the resulting cross-section (top) and the calculated cross-section upper limit (bottom).
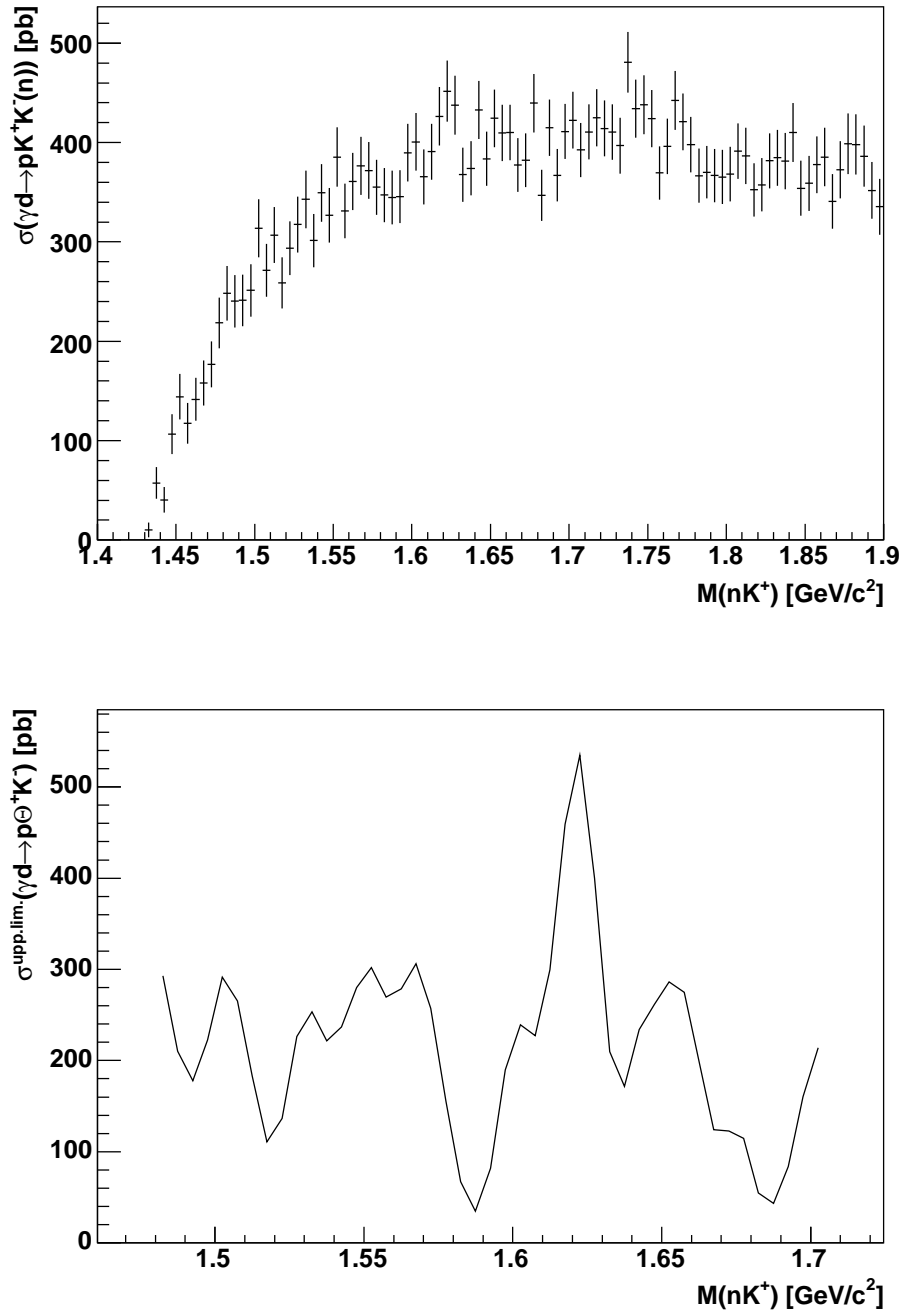
Figure 7.10: Combined Fields: Cross-Section $\gamma d \to pK^+K^-(n)$ (top). Cross-Section Upper Limit $\gamma d \to p\Theta^+K^-$ (bottom).

Consequently, the cross-section upper limit on the process $\gamma d \to p\Theta^+K^-$, is estimated to be less than $600\,pb$ in the range 1.61 to $1.63\,GeV/c^2$, and less than $300\,pb$ elsewhere in the range 1.5 to $1.6\,GeV/c^2$.

The calculation of the combined field cross-section was possible through the use of another method. A weighted mean of the high and low field cross-sections (see figure 7.2) was calculated. The resulting combined field cross-section, compared to the calculated cross-section using an addition of acceptance corrected high and low field yields, and the application of the cross-section equation (see section 7.1), can be seen in figure 7.11. As can be seen, an assumption that the error on the number of counts is proportional to the number of photons (without any corrections of second order effects) allows the simple addition of acceptance corrected yields, whilst preserving the statistical correctness of the analysis to a fraction of a percent.
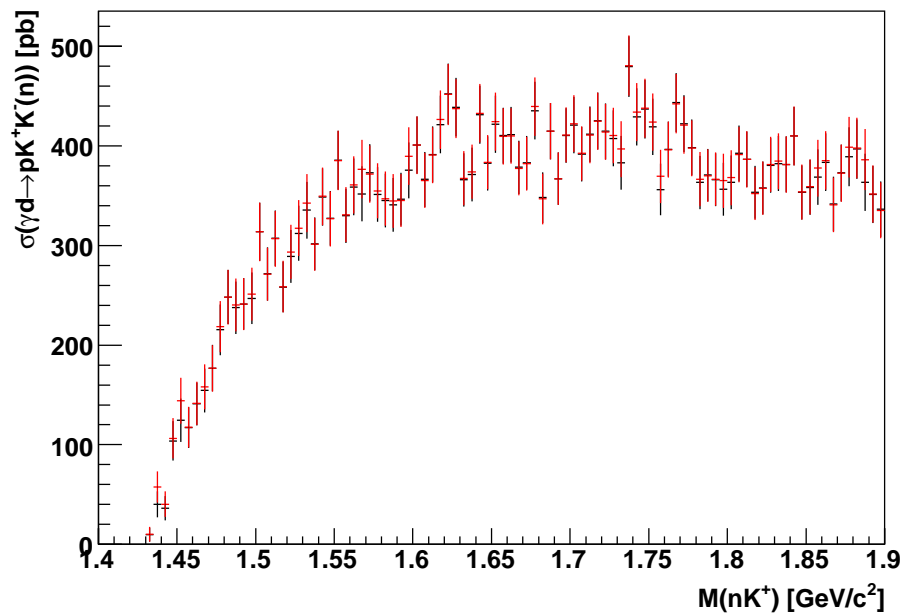
Figure 7.11: Combined fields cross-section. Black: Calculated from the addition of the acceptance corrected yields from high field and low field, followed by the application of the cross-section relation. Red: Cross-Section obtained from the weighted mean of the high and low field cross-sections.

7.5 Combined Fields Upper Limit as a function of $cos\theta_{cm}^{nK^+}$

Again, the differential cross-section upper limit, as a function of $cos\theta_{cm}^{nK^+}$, was determined for the combined fields. The procedure is exactly the same as previously detailed (see section 7.3). However, now 8 $cos\theta$ bins were constructed (see table 7.2), utilising the higher statistics (per bin) of the combined fields analysis.

Bin	$cos\theta_{min}$	$cos\theta_{max}$
1	-1.00	-0.75
2	-0.75	-0.50
3	-0.50	-0.25
4	-0.25	0.00
5	0.00	0.25
6	0.25	0.5
7	0.50	0.75
8	0.75	1.0

Table 7.2: Combined Fields cosine θ bins.

Figures 7.12, 7.13, 7.14, show the yields, differential cross-sections $\gamma d \rightarrow pK^+K^-(n)$, and the differential cross-section upper limits $\gamma d \rightarrow p\Theta^+K^-$, respectively for these 8 bins.
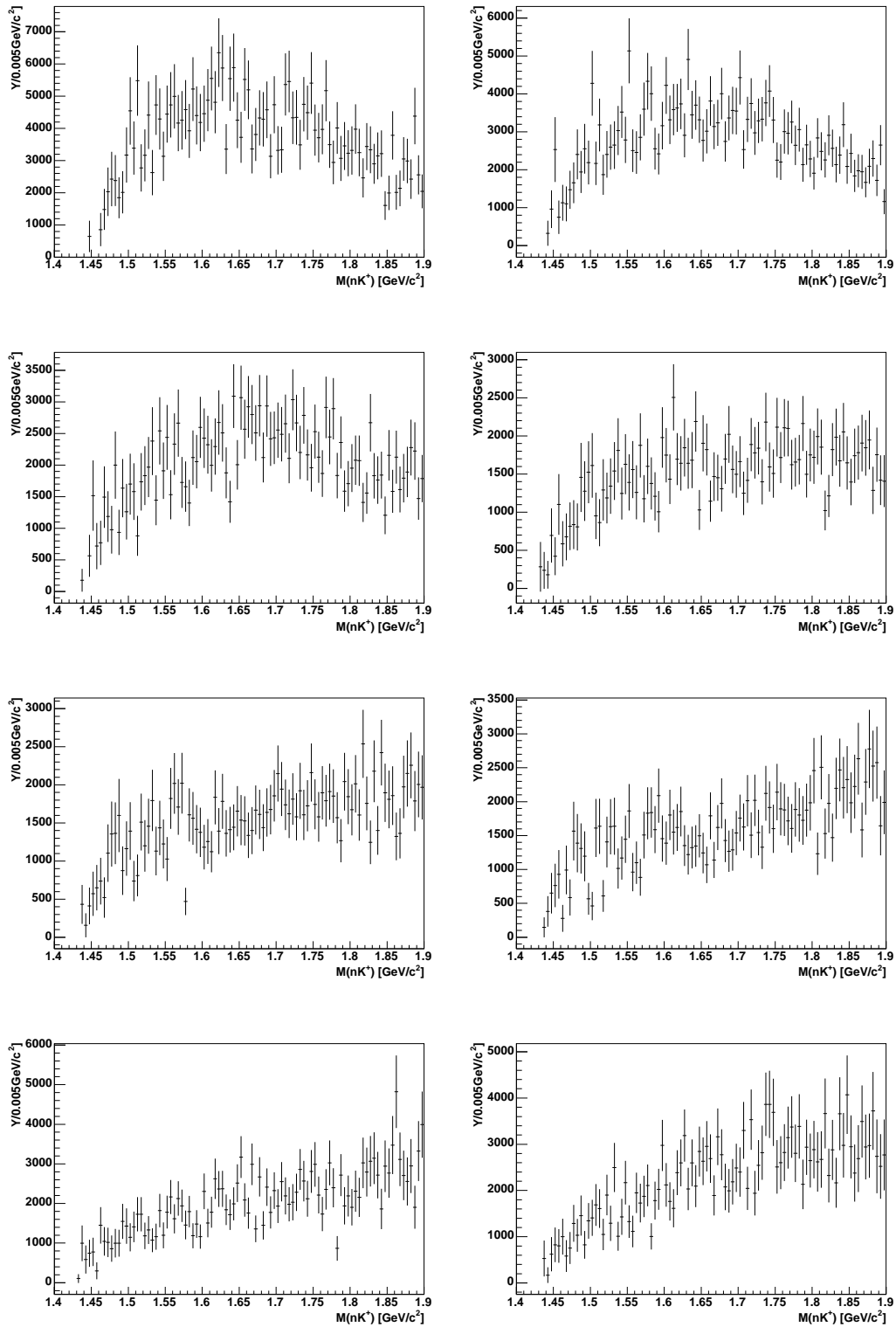
Figure 7.12: Combined Fields 8 *cosθ* bins: Yields. Top left: bin1, top right: bin 2...bottom right: bin 8.
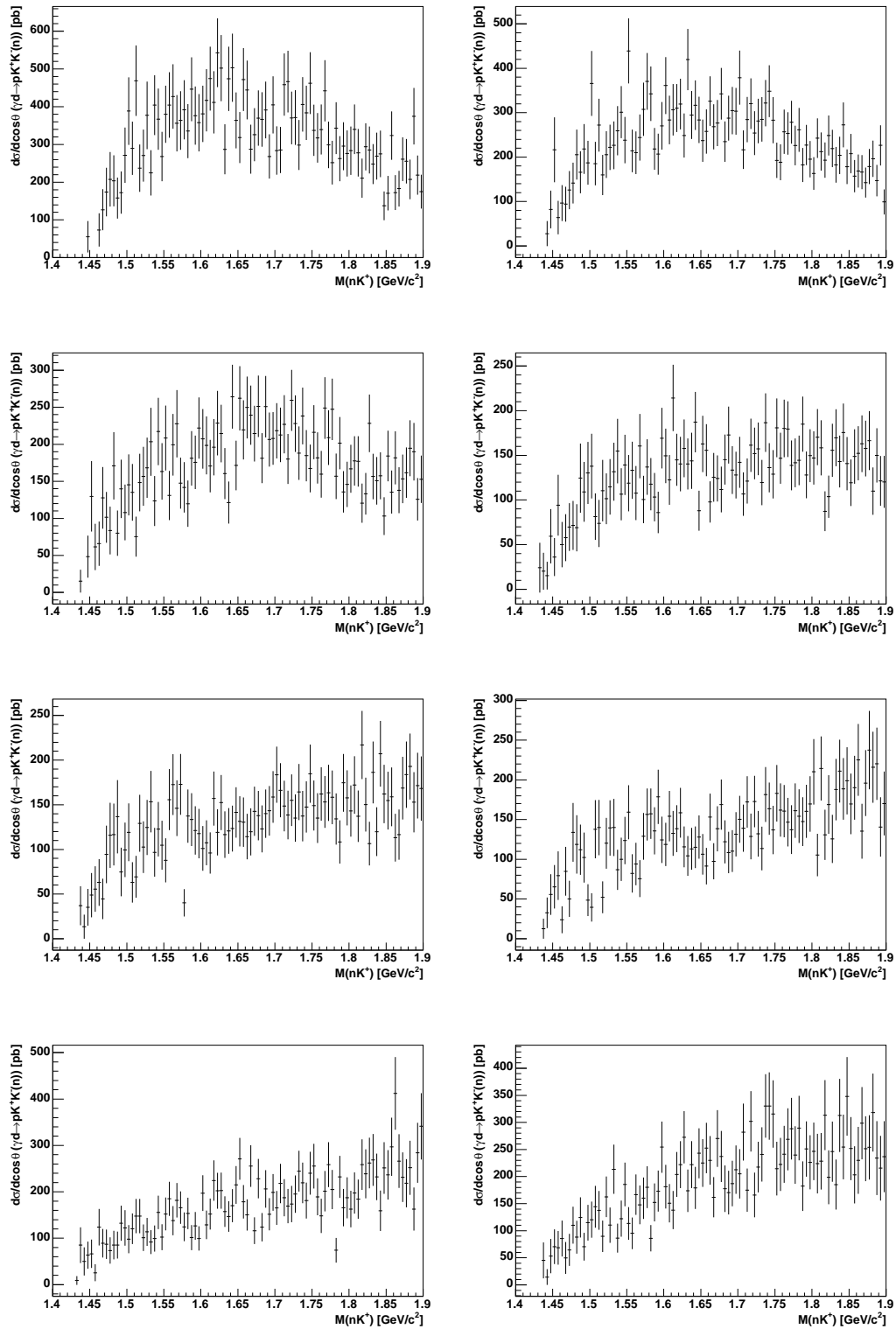
Figure 7.13: Combined Fields 8 $cos\theta$ bins: Differential Cross-Sections. Top left: bin1, top right: bin 2....bottom right: bin 8.
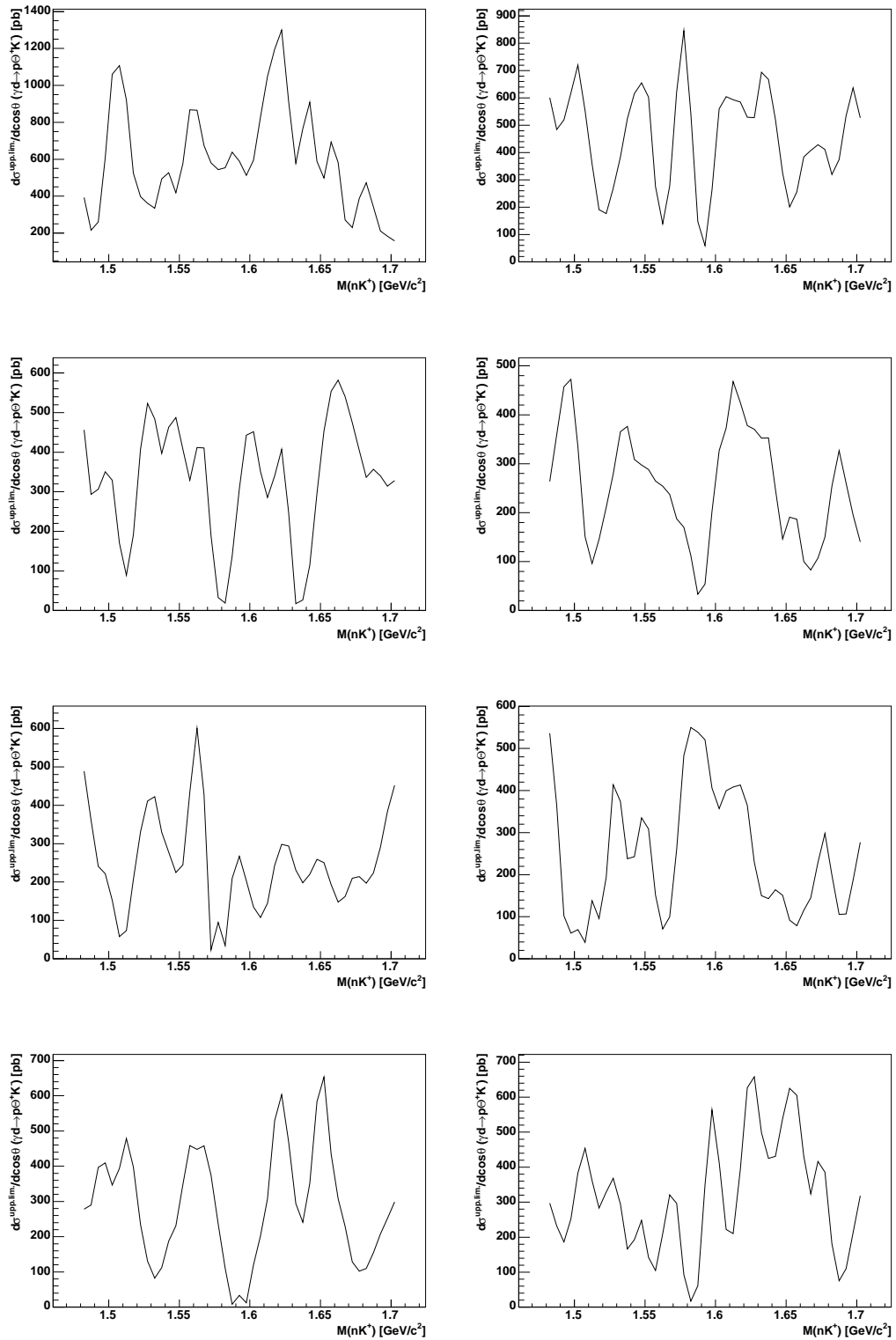
Figure 7.14: Combined Fields 8 *cosθ* bins: Differential Cross-Section Upper Limits. Top left: bin1, top right: bin2....bottom right: bin 8.

Finally, to observe the behaviour of this cross-section upper limit, the maximum in the mass range $1.52 - 1.56 \, GeV/c^2$ (black) and the value at $1.54 \, GeV/c^2$ (red), are plotted as a function of $cos\theta_{cm}^{nK^+}$. Figure 7.15 shows this.
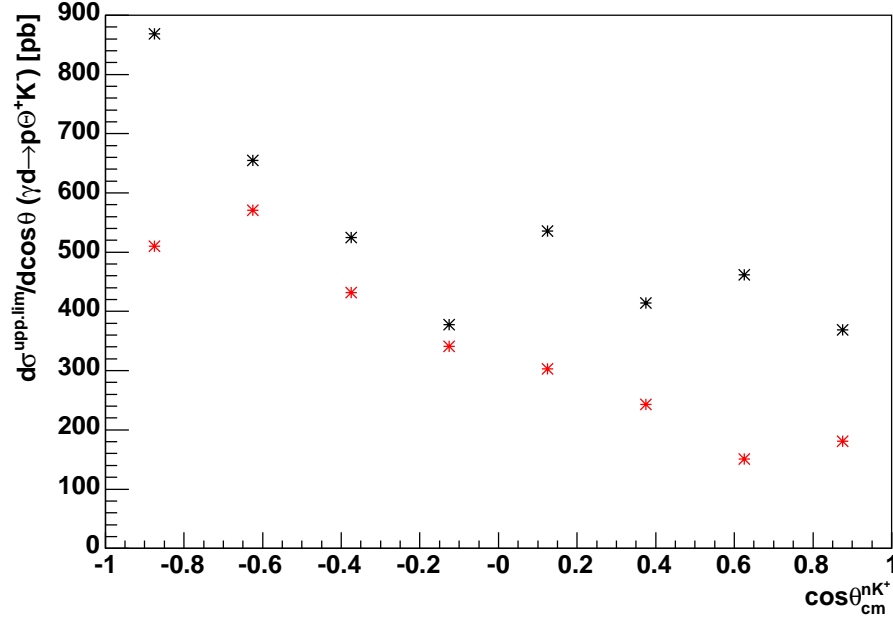
Figure 7.15: Black points: Maximum Upper Limit in the range $1.52 - 1.56 \, GeV/c^2$, Red points: Upper Limit at $1.54 \, GeV/c^2$. Each plotted as a function of $cos\theta_{cm}^{nK^+}$. Combined Fields.

7.6   Elementary Cross-Section $\gamma n \rightarrow \Theta^+ K^-$

In order to interpret the cross-section $\gamma d \rightarrow p\Theta^+ K^-$ in terms of the elementary cross-section on the nucleon $\gamma n \rightarrow \Theta^+ K^- \rightarrow K^+ K^- n$, a model must be employed. In the elementary process, $\gamma n \rightarrow \Theta^+ K^-$, there is no proton involved, however the proton in the deuteron (target), which is likely to be a spectator in Θ^+ production from deuterium, is required to have a minimum momentum of $\sim 0.3 - 0.35 \, GeV/c$ in order to be detected in CLAS. Therefore to be detected, the proton will either have a large pre-interaction momentum (on the large momentum tail of the Fermi distribution), or will need to undergo a final state interaction (FSI). Rescattering through the kaon-nucleon interaction is a possible mechanism for this FSI. Consequently, in order to comment on the elementary process, Θ^+ production on the neutron, this rescattering must be factored into the measured cross-sections (see preceding sections in this chapter).

The estimation of this rescattering correction is based on $\Lambda(1520)$ production

in the reaction $\gamma d \to p K^+ K^- n$. One can consider the symmetry in the $t-channel$ between the $\Lambda(1520)$ and Θ^+ production processes. The first order diagrams are shown in figure 7.16. For $\Lambda(1520)$ production, the reaction proceeds on the proton, with the spectator neutron only having sufficiently large momentum either pre-interaction (Fermi distribution tail), or by undergoing a FSI. This case is entirely similar to the proton in Θ^+ production. Subsequently, assuming that the production of $\Lambda(1520)$ and Θ^+ are $t - channel$ dominated, a measure of neutron rescattering in the $\Lambda(1520)$ production can be used to estimate the proton rescattering in Θ^+ production.
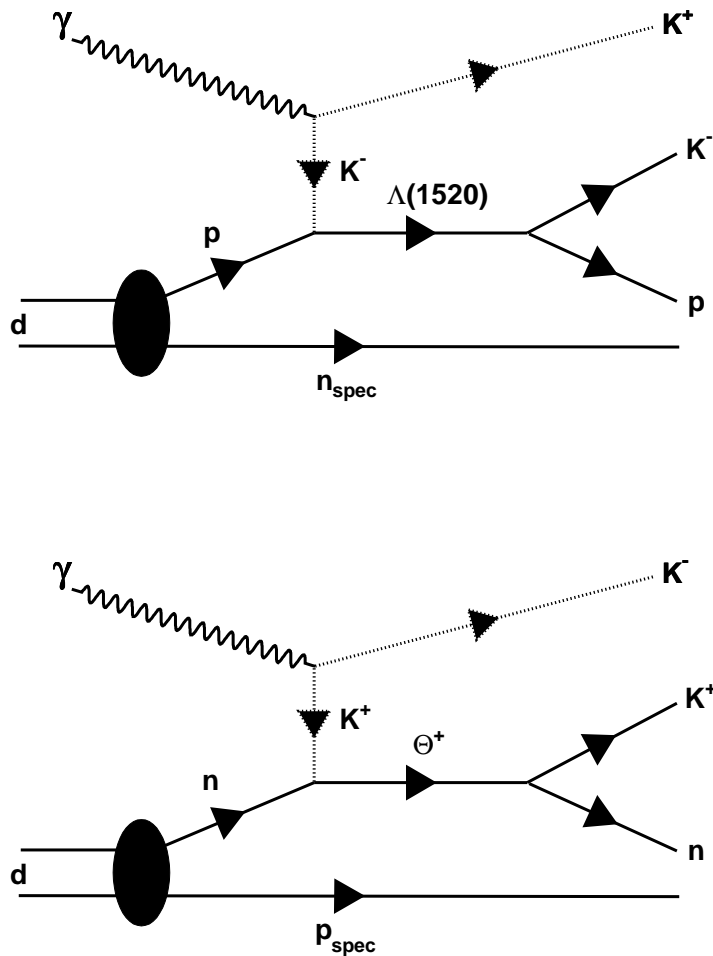
Figure 7.16: First order $t - channel$ diagrams for $\Lambda(1520)$ production (top), and Θ^+ production (bottom).

The neutron rescattering was estimated by studying the acceptance corrected yield of the $\Lambda(1520)$ as a function of neutron momentum. Figure 7.17 shows

the normalised cross-section fraction, R, for $\Lambda(1520)$ production, as a function of neutron momentum, P_n.
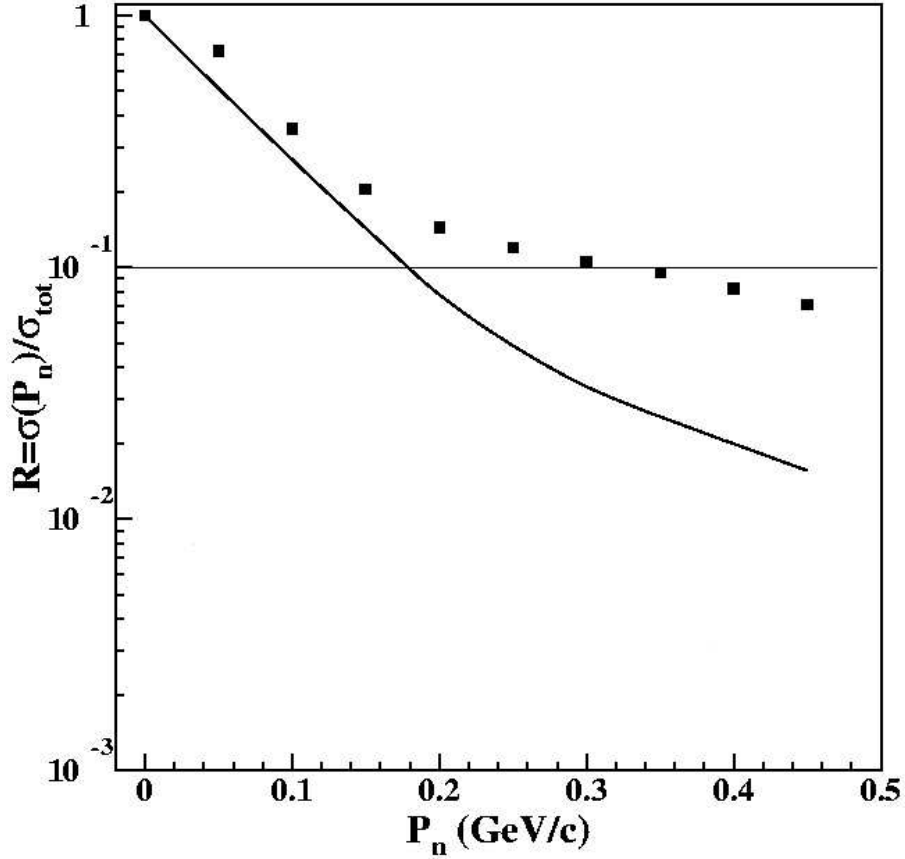
Figure 7.17: Cross-Section fraction for $\Lambda(1520)$ production, normalised to the cross-section with no neutron momentum cut, σ_{tot}, as a function of neutron momentum (squares). Also shown (solid line), is the fraction calculated using the Fermi momentum of the neutron.

Selecting events with a neutron momentum above $0.35\,GeV/c$ reduces the $\Lambda(1520)$ production cross-section by a factor of 10, compared to the cross-section without a neutron momentum cut, σ_{tot} (see figure 7.17). Assuming a similar production mechanism and FSI for the Θ^+, and acknowledging a minimum proton momentum $0.3 - 0.35\,GeV/c$ (to be detected in CLAS), gives rise to a similar reduction in Θ^+ cross-section. Consequently, the upper limit for $\gamma n \rightarrow \Theta^+ K^-$, is estimated to be a factor 10 higher than the limits presented previously in this chapter (this estimate is strongly model dependent).

One should note that since the $K^+ n$ scattering cross-section is smaller than

that of K^-p scattering [93], this rescattering correction factor is likely to be over estimated using the $\Lambda(1520)$ production as a model. However, for the purposes of an upper limit on the elementary process $\gamma n \to \Theta^+ K^-$ it represents a conservative estimate. If one were to assume that there are no FSI and the spectator protons in Θ^+ production come from the large momentum tail of the Fermi distribution, the most conservative correction factor would be ~ 50 (see figure 7.17). The solid line is the integral of the deuteron wave function, as a function of momentum, using the Paris potential [94].

Based on the predictions given in table 2.3 this estimate of the elementary cross-section would rule out theoretical models within which the Θ^+ has spin-parity $J^P = \frac{3}{2}^-, \frac{3}{2}^+$. Furthermore, the model of Guidal *et al* [45] discussed in section 2.5 predicts a **maximum** total cross-section of $1\,nb$ for the $J^P = \frac{1}{2}^+$ case, and $0.2\,nb$ for the $J^P = \frac{1}{2}^-$ case. Consequently, the estimate presented appears to rule out this model as well. However, the caveat that the estimated elementary cross-section is strongly model dependent remains.

Summary

As detailed in this chapter, the production cross-section upper limit $\gamma d \to p\Theta^+ K^-$ has been measured and provides a quantitative statement of result for this analysis. The upper limit in the mass range $1.52 - 1.56\,GeV/c^2$ is less than $0.3\,nb$ (95% confidence level), and less than $0.6\,nb$ in the mass range $1.48 - 1.7\,GeV/c^2$. Further to this measured upper limit, a (strongly) model dependent estimate of the cross-section upper limit for the elementary process $\gamma n \to \Theta^+ K^-$ is given. The final chapter is a summary presentation and contextualization of the results of this Θ^+ pentaquark search in the channel $\gamma d \to pK^+ K^- n : \Theta^+ \to nK^+$.

Chapter 8

Results and Discussion

The primary motivation behind this first ever dedicated search for the Θ^+ pentaquark was to test the reproducibility of the previous CLAS measurement with increased statistics. Furthermore, on the assumption that a Θ^+ signal was detected, the determination of its mass with a $\pm 2\, MeV/c^2$ accuracy and its spin were issues which this measurement proposed to resolve. However, as has been reported, the results of this analysis of $\gamma d \rightarrow pK^+K^-n$ with the $\Theta^+ \rightarrow nK^+$ are as follows:

- No obvious signal in the invariant mass $M(nK^+)$ spectrum in the range 1.52 to $1.56\, GeV/c^2$ was observed.

- As a consequence, further to reporting a non-observation, a cross-section upper limit on Θ^+ production was calculated.

- The upper limit in the mass range $1.52 - 1.56\, GeV/c^2$, for the reaction $\gamma d \rightarrow p\Theta^+K^-$, is less than $0.3\, nb$ (95% confidence level), and less than $0.6\, nb$ in the mass range $1.61 - 1.63\, GeV/c^2$.

- The cross-section upper limit for the elementary process $\gamma n \rightarrow \Theta^+K^-$, using a phenomenological model based on the *t-channel* symmetry between $\Lambda(1520)$ and Θ^+ production, is estimated to be a factor of 10 larger.

Figures 8.1 and 8.2 summarise the results presented in this thesis.

These results shows that the invariant mass $M(nK^+)$ peak of the previous measurement could not be reproduced, and puts significant limits on the production cross-section of a possible Θ^+ pentaquark.

Further to the analysis presented in this thesis, a comparison of the current results with the previous reported measurement was conducted by Stepan Stepanyan of the G10 analysis group. Full details of this study can be found in Ref. [82].
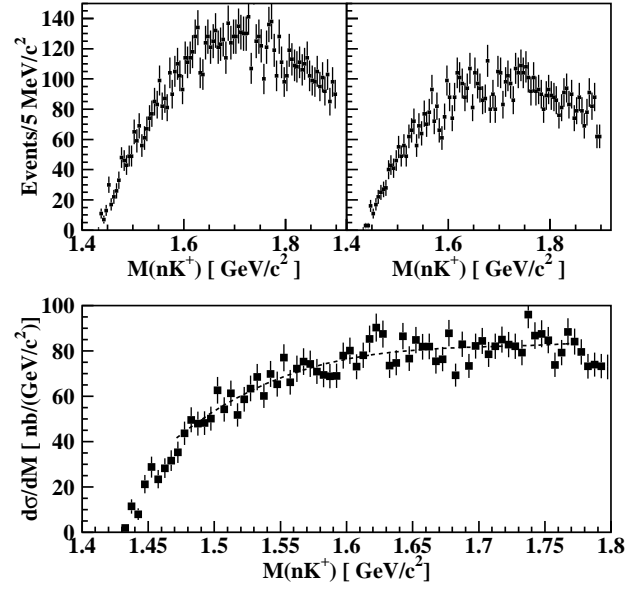
Figure 8.1: The invariant mass $M(nK^+)$ for the low (top left) and high (top right) field data. Cross-Section (differential w.r.t. mass) $\gamma d \rightarrow pK^+K^-n$ for combined fields data (bottom) with the polynomial fit shown.
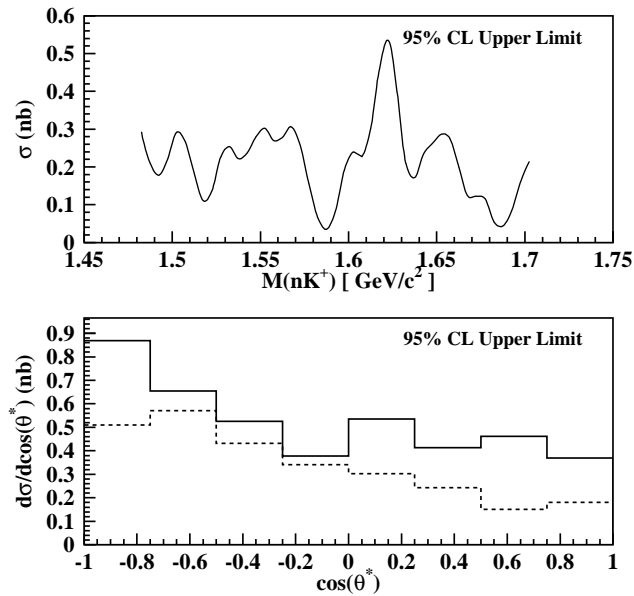
Figure 8.2: Cross-Section upper limit $\gamma d \rightarrow p\Theta^+ K^-$ (top). Differential cross-section upper limit as a function $cos\theta_{cm}^{nK^+}$ (bottom): Maximum upper limit in the mass range $1.52 - 1.56\,GeV/c^2$ (solid), or at fixed mass $1.54\,GeV/c^2$ (dashed).

The current data set was constrained to use the same event selection, and the same photon energy (range) distribution as the previous analysis. Figure 8.3 shows the previous result (points with errors), superimposed with the result of this comparison analysis (histogram). One should note that the comparison histogram has been scaled by a factor 5.9, so that both have the same total number of counts.
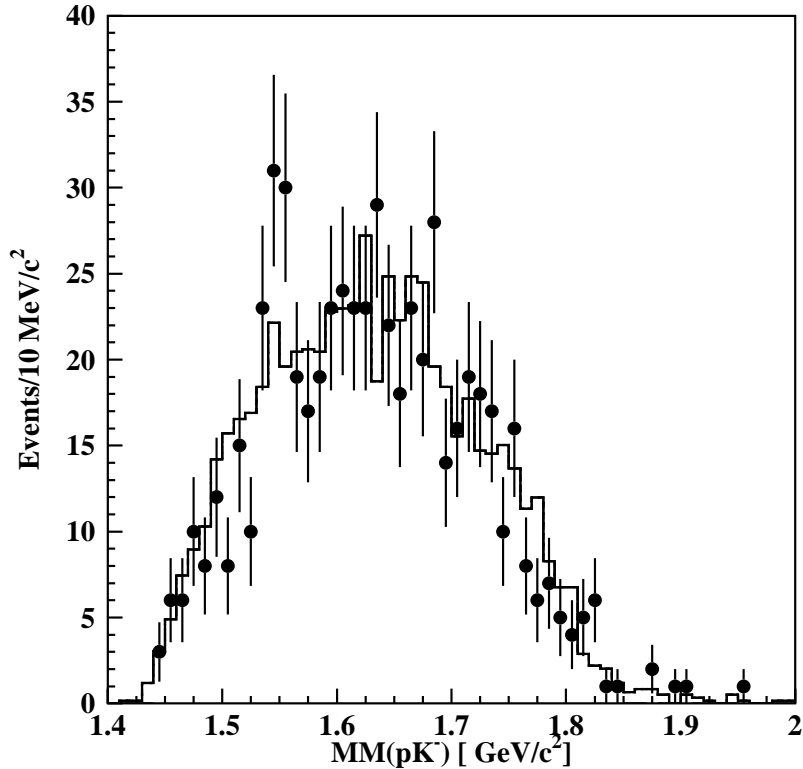
Figure 8.3: Comparison of previous published result (points with errors), with a comparison study of the current result (histogram). [82]

The previous reported peak at $1.542\, GeV/c^2$ is not reproduced, under these same analysis conditions. Using the result of the comparison analysis (histogram) as a representation of the true background, a $3rd-order$ polynomial was fitted to the histogram, along with a Gaussian peak (with width equivalent to the CLAS resolution) at $1.542\, GeV/c^2$. This results in the number of counts in the peak being 27.8 ± 9.6, and a statistical significance (of the fluctuation) of $2.9\,\sigma$. The conclusion drawn from this study is that the statistical significance of $5.2\,\sigma$ placed on the previous measurement was overstated, due to an under-estimation of the background.

Complementary to this current measurement and result for the reaction $\gamma d \rightarrow pK^+K^-n$ is the measurement from the "sister" dedicated pentaquark experiment (known as G11, performed directly after G10) conducted at CLAS. Here the exclusive reaction $\gamma p \rightarrow \bar{K}^0 K^+ n$: $\Theta^+ \rightarrow nK^+$, was studied with a photon energy range $1.6-3.8\,GeV$ and an integrated luminosity of $70\,pb^{-1}$. This reaction channel was previously analysed by the SAPHIR collaboration, which found evidence for a narrow Θ^+ state at a mass of $1.54\,GeV/c^2$, with a width $< 25\,MeV/c^2$ [16]. SAPHIR initially reported a production cross-section of $300\,nb$, however later reduced this to $50\,nb$ [95]. The invariant mass $M(nK^+)$ as calculated by the G11 analysis is shown in figure 8.4.
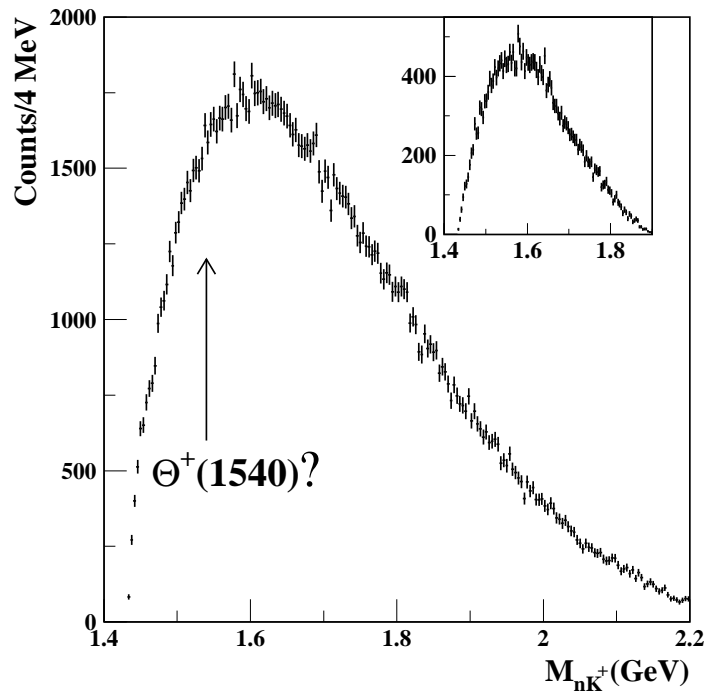
Figure 8.4: The G11 invariant mass $M(nK^+)$. The inset shows the invariant mass distribution obtained with specific cuts to reproduce the SAPHIR analysis. [96]

Similar to the result of the analysis presented here, the result [96] of this analysis (with significantly higher statistics than the SAPHIR measurement) found no evidence for the Θ^+, in the mass range $1.52 - 1.6\,GeV/c^2$, where previous evidence was seen. As a consequence of this null result, the G11 group also calculated a cross-section upper limit for Θ^+ production as a function of Θ^+ mass and centre-of-mass angle of the $\bar{K}^0$ (see figure 8.5).
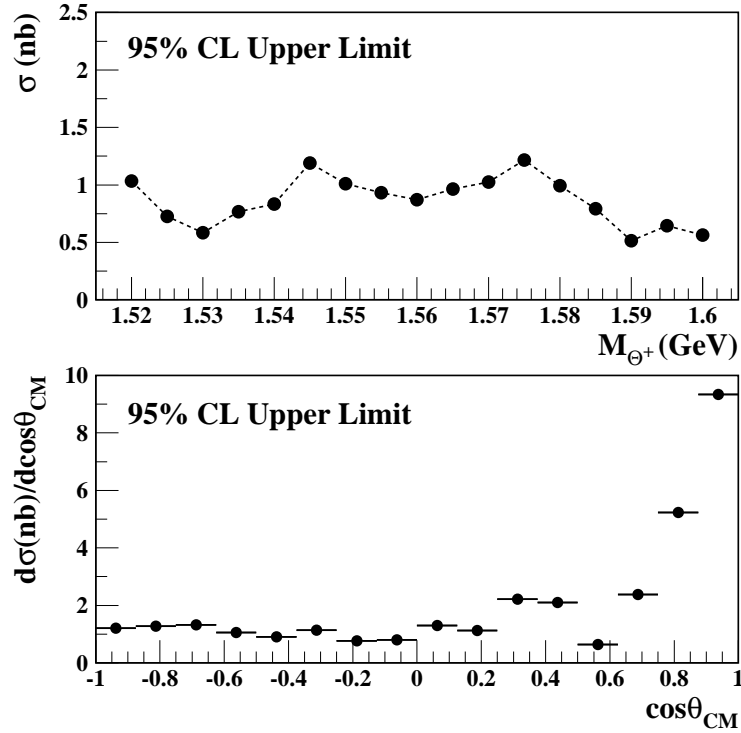
Figure 8.5: The G11 total cross-section upper limit as a function of Θ^+ mass (top). Differential cross-section upper limit, as a function of $cos\theta_{CM}^{\bar{K}^0}$ (with an assumed Θ^+ mass of $1.54\,GeV/c^2$. [96]

This measurement sets a cross-section upper limit of $0.8\,nb$ (95% confidence level), for an assumed Θ^+ mass of $1.54\,GeV/c^2$. One should note that both of these current CLAS results clearly identify the final nK^+ (baryonic) state to have $S = +1$, since the direct measurement of the K^+ defines and guarantees the strangeness. This process is referred to as *strangeness tagging*.

The G10 data set also provided the opportunity to analyse [97–99] the reaction $\gamma d \rightarrow \Lambda K^+ n$: $\Lambda \rightarrow p\pi^-$. Figure 8.6 shows the invariant mass $M(nK^+)$ (left), and cross-section/differential cross-section upper limit (right). No signal corresponding to the Θ^+ was found in this reaction channel. The calculated cross-section upper limit is of the order $< 10\,nb$. A further reaction channel $(\gamma d \rightarrow pK_s^0 K^- p)$ is currently being analysed [100].

It is interesting once again to review the previous measurements with evidence for the Θ^+ (see table 1.1). In each of these cases, the statistical significance was calculated using the relation $\sigma = N_s/\sqrt{N_B}$, where N_S is the number of counts in the signal and N_B is the number of counts in the background (also useful to define the number of counts of the peak $N_P = N_S + N_B$). A more meaningful statistical significance [101] may be to calculate the significance of the background
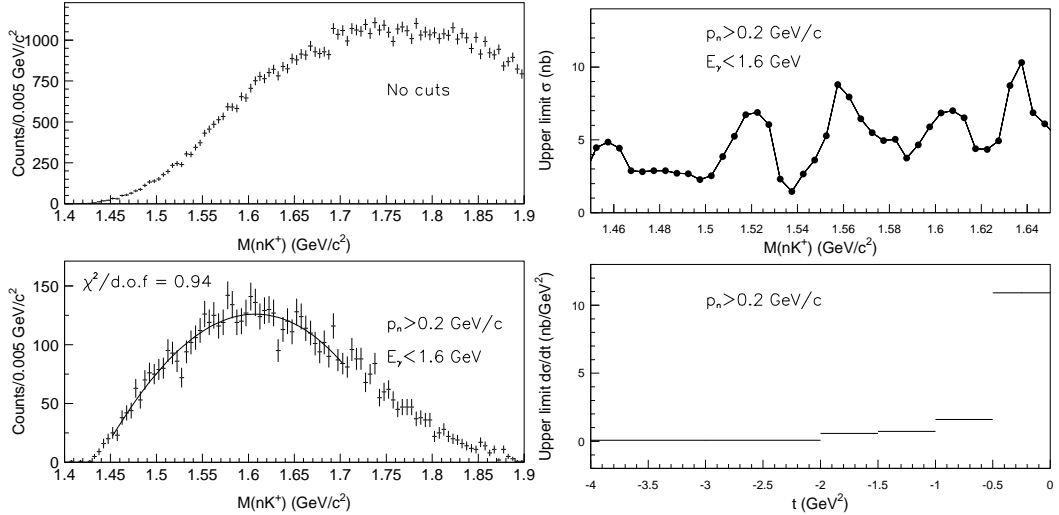
Figure 8.6: Invariant mass $M(nK^+)$, with different kinematic cuts (left). Cross-Section / differential cross-section upper limits (95% confidence level). [97–99]

fluctuating up into the range $N_P \pm \sqrt{N_P}$. This calculation results in a reduction of the statistical significance of each of the previous reported measurements (table 8.1 shows three examples).

Group	Ref.	Reaction	Reported σ's	Fluctuation to $N_P \pm \sqrt{N_P}$
LEPS	[14]	$\gamma n \to K^+ K^- n$	4.6	3.1
DIANA	[17]	$K^+ Xe \to K^0 p Xe'$	4.4	2.9
CLAS	[2]	$\gamma d \to p K^+ K^- n$	5.2 ± 0.6	4.4

Table 8.1: Examples of the recalculation of statistical significances.

Clearly one can conclude that the method employed to calculate the statistical significance of any signal determines the impact with which results are perceived. Furthermore, it is vital to have a correct calculation of the background in order to perform such calculations.

Existence of the Θ^+ Pentaquark

The question as to why so many initial experiments reported evidence for the Θ^+, and indeed why so many did not, is obviously one which must be addressed. However, the answer to such a question is far from trivial. Issues such as statistics, experimental sensitivity and analysis techniques (missing mass or invariant mass) have to be investigated. It is likely that in many cases, the statistics of these

previous measurements may have led to the mis-interpretation of fluctuations. Consequently, any future measurements must meet the following requirements:

- Essential to have a large statistics data set.

- Essential to have a definitive *strangeness tag* for the final baryonic state.

- Essential to have correctly calculated backgrounds (with theoretical justification).

- Essential to provide cross-sections and/or upper limits.

Ideally all other previous experiments which reported evidence, would be reproduced in a manner which fulfilled the above criteria (as has been the case with this current CLAS $\gamma d \to pK^+K^-n$ experiment and analysis). There is currently a proposal to repeat the previous CLAS proton experiment ($\gamma p \to \pi^+K^+K^-n$), with an estimated factor 50 increase in statistics.

In conclusion, this current null result along with the significant limits placed on the production cross-section provides compelling (yet not definitive) evidence for the non-existence of the Θ^+ pentaquark state. If this were the case, and exotic $S = +1$ pentaquark states do not exist, then one would be required to question the rules governing Quantum ChromoDynamics (QCD) (which do not prohibit their existence), and our understanding of the strong interaction. It is clear, presently, that the existence of the pentaquark is tenuous, yet further intensive study is required both experimentally and theoretically to resolve this question of scientific verisimilitude.

Bibliography

[1] B. McKinnon *et al.* Search for the Θ^+ Pentaquark in the Reaction $\gamma d \rightarrow pK^+K^-n$. hep-ex/0603028, Accepted for publication in Phys. Rev. Lett., 2006.

[2] S. Stepanyan *et al.* Phys. Rev. Lett., **91**:252001, 2003.

[3] H.J. Lipkin. Nucl. Phys., **A 625**:207, 1997.

[4] D. Strottman. Phys. Rev., **D 20**:748, 1979.

[5] F. Halzen and A. Martin. *Quarks & Leptons.* New York, USA: John Wiley & Sons (1985).

[6] D.H. Perkins. Contemp. Phys., **16**:173, 1975.

[7] K. Joo *et al.* Phys. Rev. Lett., **88**:122001, 2002.

[8] M. Gell-Mann and Y. Ne'eman. *The Eightfold Way.* New York, USA: W.A. Benjamin (1964).

[9] H.J. Lipkin. *Interactions Between Particle and Nuclear Physics.* AIP Conf. Proc., **150**:657, 1986.

[10] R.L. Jaffe. Phys. Rev., **D 15**:267, 1977.

[11] D. Diakonov, V. Petrov and M. Polyakov. Z. Phys., **A 395**:305, 1997.

[12] R.L. Jaffe and F. Wilczek. Phys. Rev. Lett., **91**:232003, 2003.

[13] N. Mathur. Phys. Rev., **D 70**:074508, 2004.

[14] T. Nakano *et al.* Phys. Rev. Lett., **91**:012002, 2003.

[15] V. Kubarovsky *et al.* Phys. Rev. Lett., **92**:032001, 2004.

[16] J. Barth *et al.* Phys. Lett., **B 572**:127, 2003.

[17] V. Barmin *et al.* Phys. Atom. Nucl., **66**:1715, 2003.

[18] A.E. Asratyan, A.G. Dolgolenko and M.A. Kubantsev. Phys. Atom. Nucl., **67**:682, 2004.

[19] A. Airapetian *et al.* Phys. Lett., **B 585**:213, 2004.

[20] A. Aleev *et al.* Phys. Atom. Nucl., **68**:974, 2005.

[21] M.Abdel-Bary *et al.* Phys. Lett., **B 595**:127, 2004.

[22] A. Berthon *et al.* Prog. Part. Nuclear Physics, **B 63**:54, 1973.

[23] K. Hicks. Prog. Part. Nucl. Phys., **55**:648, 2005.

[24] The ZEUS Collaboration. Phys. Lett., **B 591**:7, 2004.

[25] C. Alt *et al.* Phys. Rev. Lett., **92**:042003, 2004.

[26] H.G. Fischer and S. Wenig. Eur. Phys. J., **C 37**:133, 2004.

[27] CLAS Collaboration and JLab Management. CLAS Collaboration Statement.

[28] K. Hicks, S. Stepanyan *et al. Investigation of Exotic Baryon States in Photoproduction Reactions with CLAS.* JLab Proposal, **E03-113**.

[29] M. Gell-Mann. Phys. Rev., **8**:214, 1964.

[30] G. Zweig. CER-8182-TH-401., 1964.

[31] G. Zweig. CER-8419-TH-412., 1964.

[32] CDF Collaboration, D0 Collaboration and Tevatron Electroweak Working Group. hep-ex/0507006, 2005.

[33] D.J. Gross and F. Wilczek. Phys. Rev., **D 8**:3633, 1973.

[34] N. Isgur, R. Kokoski and J. Paton. Phys. Rev. Lett., **54**:869, 1984.

[35] T. Barnes. Acta. Phys. Polon, **B 31**:2545, 2000.

[36] C. Barnard *et al.* Phys. Rev., **D 56**:7039, 1997.

[37] M. Chanowitz and S.Sharpe. Nucl. Phys., **B 222**:211, 1983.

[38] F. Viron. Phys. Rev. Lett., **53**:2207, 1983.

[39] S. Zhu. Phys. Rev., **D 60**:097502, 1999.

[40] R. Jaffe. Phys. Rev. Lett., **38**:195, 1977.

[41] T.H. Skyrme. Nucl. Phys., **31**:556, 1962.

[42] E. Witten. Nucl. Phys., **B 223**:433, 1983.

[43] E. Witten. Nucl. Phys., **B 223**:422, 1983.

[44] F.E. Close and Q. Zhao. Phys. Lett., **B 590**:176, 2004.

[45] M. Guidal *et al.* Phys. Rev., **D 72**:054012, 2005.

[46] S. Nam *et al.* Phys. Lett., **B 633**:483, 2006.

[47] Y. Oh *et al.* Phys. Rept., **423**:49, 2006.

[48] C.M. Ko and W. Liu. nucl-th/0410068, 2004.

[49] W. Roberts. Phys. Rev., **C 70**:065201, 2004.

[50] D. Barber *et al.* Z. Phys., **C 7**:17, 1980.

[51] S. Barrow *et al.* Phys. Rev., **C 64**:044601, 2001.

[52] C.W. Leemann, D.R. Douglas and G.A. Krafft. *The Continuous Electron Beam Accelerator Facility: CEBAF at the Jefferson Laboratory.* Ann. Rev. Nucl. Part. Sci., **51**:413–450, 2001.

[53] D. Sober *et al.* Nucl. Instrum. Meth., **A 440**:263–284, 2000.

[54] S. Christo. *The Hall B Cryotarget Website.* http://www.jlab.org/ christo/target_intro.html.

[55] D. Dale *et al. The Primex Website.* http://www.jlab.org/primex.

[56] B.A. Mecking *et al.* Nucl. Instrum. Meth., **A 503**:513–553, 2003.

[57] S. Taylor *et al.* Nucl. Instrum. Meth., **A 462**:484, 2001.

[58] M.D. Mestayer *et al.* Nucl. Instrum. Meth., **A 449**:81–111, 2000.

[59] G. Adams *et al.* Nucl. Instrum. Meth., **A 465**:414, 2001.

[60] E.S. Smith *et al.* Nucl. Instrum. Meth., **A 432**:265–298, 1999.

[61] M. Amarian *et al.* Nucl. Instrum. Meth., **A 460**:239, 2001.

[62] D.C. Doughty *et al.* Nucl. Sci. IEEE Transactions, **39**:241–247, 1992.

[63] *Jefferson Lab Online Data Acquisition.* http://coda.jlab.org.

[64] D. Cords *et al.* *CLAS Event Format with BOS.* CLAS-NOTE 94-012, 1994.

[65] V. Blobel *et al.* *The BOS System for CLAS Detector.* Unpublished, 1995.

[66] J. Manak *et al.* *Data Processing Procedures.* CLAS-NOTE 99-016, 1999.

[67] D. Axmark *et al.* http://www.mysql.com.

[68] G. Gavalian. *C Interface to MySQL.* CLAS-NOTE 02-011, 2002.

[69] E. Anciant *et al.* *Tagger Calibration Overview.* CLAS-NOTE 99-004, 1999.

[70] J. Li *et al.* *PhotonTcal.* CLAS-NOTE 03-004, 2003.

[71] E.S. Smith *et al.* *Calibration of the CLAS TOF System.* CLAS-NOTE 99-011, 1999.

[72] D. Lawrence *et al.* *CLAS Drift Chamber Calibration: Software and Procedures.* CLAS-NOTE 99-018, 1999.

[73] M. Guillo *et al.* *EC Time Calibration Procedure for Photon Runs in CLAS.* CLAS-NOTE 01-014, 2001.

[74] S. Stepanyan. CLAS-ANALYSIS-NOTE 03-105, 2003.

[75] D. Sober, H. Crannell and F.J. Klein. CLAS-NOTE 04-019, 2004.

[76] N. Baltzell. Private Communication.

[77] B. McKinnon. G10: Θ^+ Pentaquark in the Exclusive Photoproduction Reaction $\gamma d \rightarrow pK^+K^-n$. CLAS-ANALYSIS-NOTE, 2006.

[78] E. Pasyuk. *ENERGY LOSS ROUTINE.* JLAB CUE.

[79] N. Baltzell. *Testing G10 Eloss Correction.* Unpublished CLAS-NOTE.

[80] T. Mibe, M. Mirazita and N. Baltzell. *G10 Momentum Corrections.* Private Communications.

[81] S. Stepanyan. Private Communication.

[82] S. Stepanyan. CLAS-ANALYSIS-NOTE, 2006.

[83] K. Hicks. CLAS-ANALYSIS-NOTE, 2006.

[84] T. Mibe. CLAS-ANALYSIS-NOTE, 2006.

[85] D. Carman. CLAS-ANALYSIS-NOTE, 2006.

[86] M.   Holtrop.   *CLAS   GEANT   Simulation   Website.*
     http://www.physics.unh.edu/ maurik/gsim_intro.shtml.

[87] Application Software Group/Computing and Networks Division. *GEANT-*
     Detector Description and Simulation Tool. CERN Geneva, Switzerland,
     1993.

[88] K. Joo. *GPP CLAS SOFTWARE ROUTINE.* JLAB CUE.

[89] S. Stepanyan. Private Communication.

[90] T. Sjostrand *et al. PYTHIA Physics and Manual.* hep-ph/0308153, 2003.

[91] J. Ball and E. Pasyuk. *Photon Flux Determination.* CLAS-NOTE 05-002,
     2005.

[92] G.D. Feldman and R.D. Cousins. Phys. Rev., **D 57**:3873, 1998.

[93] S. Eidelman *et al.* Phys. Lett., **B 592**:1, 2004.

[94] M. Lacombe *et al.* Phys. Rev., **C 21**:861, 1980.

[95] M. Ostrick. Prog. Part. Nucl. Phys., **55**:337, 2005.

[96] M. Battaglieri *et al.* Phys. Rev. Lett., **96**:042001, 2006.

[97] S. Niccolai. CLAS-ANALYSIS-NOTE, 2006.

[98] M. Mirazita. CLAS-ANALYSIS-NOTE, 2006.

[99] P. Rossi. CLAS-ANALYSIS-NOTE, 2006.

[100] N. Baltzell. CLAS-ANALYSIS-NOTE, 2006.

[101] A.M. Sandorfi. *Experimental Review of Pentaquarks.* Presentation at Pen-
     taquark 2005, JLab (2005).